INFORMATION TO USERS

.

Inversion of Controlled-Source Audio-Frequency

Magnetotelluric Data

Xinyou Lu

A dissertation submitted in partial fulfillment

of the requirements for the degree of

Doctor of Philosophy

University of Washington

1999

Program Authorized to Offer Degree: Geophysics Program

UMI Number: 9937618

Copyright 1999 by
Lu, Xinyou
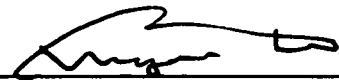
UMI
300 North Zeeb Road
Ann Arbor, MI 48103

In presenting this dissertation in partial fulfillment of the requirements for the Doctorial degree at the University of Washington, I agree that the Library shall make its copies freely available for inspection. I further agree that extensive copying of this thesis is allowable only for scholary purposes, consistant with "fair use" as prescribed in the U.S. Copyright Law. Requests for copying or reproduction of this dissertation may be referred to University Microfilms, 1490 Eisenhower Place, P.O. Box 975, Ann Arbor, MI 48106, to whom the author has granted "the right to reproduce and sell (a) copies of the manuscript in microform and/or (b) printed copies of the manuscript made from microform."

Signature

Date June 2, 1999

University of Washington

Graduate School

This is to certify that I have examined this copy of a doctoral dissertation by

Xinyou Lu

and have found that it is complete and satisfactory in all respects,
and that any and all revisions required by the final
examining committee have been made.

Co-Chairs of Supervisory Committee:

_____

Martyn Unsworth

_____

John Booker

Reading Committee:

_____

Jimmy Larsen

Date: _____ 6/2/99 _____

University of Washington

Abstract

Inversion of Controlled-Source Audio-Frequency Magnetotelluric Data

by Xinyou Lu

Co-Chairs of Supervisory Committee

Associate Professor Martyn Unsworth
Geophysics Program

Professor John Booker
Geophysics Program

This dissertation addresses an inversion algorithm to recover the Earth's electrical structure from controlled-source audio-frequency magnetotelluric data. The algorithm is based on the concepts of rapid relaxation inversion (RRI) of magnetotelluric data. The inversion uses the same technique to compute sensitivities as RRI and these approximate sensitivities are validated by comparison with exact sensitivities. The comparison shows that the approximate sensitivities have similar depth variations although different magnitudes as the exact sensitivities when transmitter-receiver offsets are greater than one skin depth in the Earth. A relationship between rapid relaxation inversion and the standard inversion is established through the sensitivity matrix. It is shown that RRI computes the sensitivities of data to the cells directly below the observation site by using approximate analytic formulas similar to the 1-D Fréchet derivative, and approximates the sensitivities of data to the rest of cells to be zero. The combination of sensitivity comparison and successful inversion imply that the accuracy of the sensitivity matrix need not be very high for an iterative inversion.

The 2.5-D finite-element forward modeling method of Unsworth *et al.* (1993) is

used in this inversion algorithm and extended to include a magnetic source. Thus the 2.5-D finite-element forward modeling method can model any source exciting a 2-D Earth. In principle, this inversion algorithm can invert CSAMT data from an electric or a magnetic source. The algorithm is tested on synthetic and field data from a electric dipole, a horizontal magnetic dipole and a finite-length horizontal electric dipole, and gives promising results.

TABLE OF CONTENTS

LIST OF FIGURES

LIST OF TABLES

ACKNOWLEDGMENTS

I would like to thank my co-advisor Professor John Booker for supporting and encouraging independent research. I would like to thank my co-advisor Professor Martyn Unsworth for his advice in the last three years of this endeavor. I would also like to thank Professor Jimmy Larsen for serving on my supervisory committee and my dissertation reading committee along with Professors John Booker and Martyn Unsworth and providing many valuable suggestions and comments that definitely improved this dissertation. I would like to also thank Professors Marshall Baker, Ken Bube and Robert Winglee for serving as my supervisory committee. Thanks also go to Don Watts for permitting use of his field data and to Steve Malone and Peter Lombard for their computer assistance. Special thanks go to my wife, Ying Xiong, for her great support, and my son, Bravyn, for relaxing me.

To My Parents: Lu Xiangsu and Mao Zhonpu

.

.

Chapter 1

INTRODUCTION

This dissertation describes some rapid inversion algorithms that can be used to recover the Earth's subsurface electrical conductivity structure from controlled source audio-frequency magnetotelluric (CSAMT) data. A range of transmitters are considered, including a horizontal electric dipole (HED), a finite-length horizontal electric dipole (FLHED), and a horizontal magnetic dipole (HMD).

The first section of this chapter gives a general introduction to the factors which influence the Earth's electrical conductivity. The second section reviews the history of CSAMT and its application. The third section of this chapter overviews this dissertation.

1.1 Factors influencing the Earth's electrical conductivity

The materials that lie at depth within the earth can be constrained by measurements of their physical properties such as density, velocity, magnetic permeability, dielectric permittivity, electrical conductivity, etc. The physical property sensed by CSAMT is electrical conductivity. The electrical resistivity is the reciprocal of the conductivity and is the other term often used. Only isotropic materials will be discussed in this dissertation.

The main factors influencing the conductivity of a rock at a shallow depth are minerals comprising the rock, the chemistry of electrolytic fluids in the pores, temperature, and the geometry of pore structures. Rock is a complex mixture of ma-

terials and different conduction mechanisms (electronic conduction, ionic conduction and electrolytic conduction) contribute to the overall conductivity. Under certain circumstance, one mechanism dominates others.

Minerals, the main constituents of rocks, can be separated into three groups by their conductivity property: 1) good conductors, 2) insulators, and 3) semiconductors between them. Minerals such as copper, iron and gold are the first group, which are of great economic interest and rarely occur in their native states, but their presence in a rock significantly increases the conductivity of the rock. Various compounds of those minerals may also be of high conductivity. Electronic conduction is the main conduction mechanism. The second group is mostly rockforming minerals such as quartz, feldspar and calcite, whose conductivities are less than 10^{-8} S/m. A large portion of minerals are semiconductors. The conductivity of semiconductors often is increased with temperature due to the energy provided by thermal excitation. Economic ore minerals are usually sulfides and oxides, which are also semiconductors and have high conductivities. The presence of highly conducting minerals may greatly increase the conductivity of the rock.

Electrolytic fluids such as water contained in the pores of a rock are another factor, possibly more influential than minerals, since, in most rocks, the fluid is the only constituent present with significant conductivity. Electrolytic conduction plays an important role in the conductivity of a fluid-bearing rock. The conductivity of a fluid-bearing rock can be empirically described by Archie's law (Archie, 1942; Keller, 1988),

$$\sigma = a\sigma_w S^n \phi^m \qquad (1.1)$$

where σ is the bulk conductivity of the rock, σ_w is the conductivity of the fluid, S is the fraction of the pore space filled with the fluid, ϕ is the porosity expressed as a volume fraction of the rock, which could be occupied by a gas, n is an empirical parameter termed the saturation exponent (normally close to 2.0), a is a parameter which varies somewhat according to interconnectivity and m is a parameters which

indicates fracture density. From Archie's law, the conductivity of rocks will decrease if the pore space is filled with air, gas or oil. Conversely, it will increase sharply if the pore space is filled with water or other electrolytic fluids. Generally, sedimentary rocks are much more porous than igneous or metamorphic rocks, and thus, more conductive.

Temperature may also be an important factor. Ionic conduction becomes more and more important as temperature increases. The mobility and number of ions in fluids in the pores increase with temperature, and thus the conductivity of the rock increases also. Usually, pronounced conductivity anomalies are associated with geothermal areas. At very high temperature, rocks may melt and molten rocks have a high conductivity. Because water and other fluids begin to be freeze below 0°C, the conductivity of the rock gradually decreases with temperature. Normally, permafrost has very low conductivity.

Pore structure is another important factor influencing rock conductivity. For a given porosity and electrolyte content, fracture and joint porosity will result in higher rock conductivity, while vuggy and isolated porosity will generate lower rock conductivity.

Other factors such as pressure may also influence the rock conductivity. The rock conductivity is not just controlled by one factor, but is usually influenced by many factors. Keller (1988) has a more detailed discussion about factors influencing the conductivity and Palacky (1988) gives a review of the resistivity characteristics of geologic targets.

1.2 CSAMT

Controlled source audio-frequency magnetotellurics uses electromagnetic (EM) fields from an artificial source to investigate the conductivity structure of the Earth's interior through analysis of electric and magnetic fields observed on its surface. CSAMT

is similar to natural-source magnetotellurics (MT), the difference between them is the source of the EM fields. Therefore, it is useful to briefly review MT. A brief mathematical derivation of MT is given in Chapter 2. Vozoff (1988) gave a thorough review on MT and also collected some important published MT papers into a single volume (Vozoff, 1986).

Tikhonov (1950) and Cagniard (1953) independently proposed the MT method. The dependence of MT on natural sources quickly attracted geophysicists' attention. It required no power supplies and the corresponding control system. Also, natural signals are very strong at long periods and can be assumed to be plane waves (one-dimensional), and then the interpretation of MT data is greatly simplified. From then up to 1980, MT progressed steadily but slowly with the debate on the validity of the plane-wave assumption in later 1950s and early 1960s (Wait, 1954; Price, 1962; Madden and Nelson, 1964; etc.), the introduction of the concept of impedance tensor (Cantwell and Madden, 1960), the development of remote reference (Gamble et al, 1979 a & b), and application of 1-D inversion (Oldenburg, 1979), but was largely hindered by the lack of innovation in instrument (data acquisition), data processing and interpretation techniques. Since 1980, MT has advanced rapidly with the revolution of digital electronics, new data processing and interpretation techniques. In data acquisition, advanced digital electronics results in highly sensitive magnetic sensor and multi-channel collecting units, and therefore enhances data quality and efficiency. In data processing, robust estimates yield superior transfer functions over conventional methods (Egbert and Booker, 1986; Chave, 1987) and the Groom-Bailey decomposition (Groom and Bailey, 1989, 1991) can effectively remove near surface 3-D distortions. In data interpretation, practical 2-D inverse algorithms have been developed (deGroot-Hedin and Constable, 1990; Smith and Booker, 1991). Today, MT is widely used as a powerful geophysical tool.

The dependence of MT on natural fields is its major attraction, and also its greatest weakness. Because natural sources are unpredictable and there exists a persistent

spectral energy low near 1 Hz, it often takes a very long time to obtain good data. Sometimes, for instance, in an oil field, it may be impossible to get high-quality MT data because of very strong cultural noise. In order to provide a stable, dependable signal, Goldstein and Strangway (1975) proposed using a grounded electric dipole source instead of relying on natural sources. This technique was called Controlled Source Audio-Frequency Magnetotellurics.

The utilization of artificial sources resulted in higher-quality data and more efficient measurements than are usually obtainable with natural-source MT, but greatly complicates data interpretation in most situations because of the 3-D nature of the electromagnetic fields from an artificial source. In the far field, beyond a distance of approximately three skin depths from the transmitter, the electromagnetic fields can be assumed to be planar. If the mutually orthogonal electric and magnetic fields, E and H, are measured, then the apparent resistivity ρ_a and phase ϕ are defined as

$$\rho_a = \frac{1}{\omega\mu}\left|\frac{E}{H}\right|^2 \tag{1.2}$$

and

$$\phi = Arg\left(\frac{E}{H}\right) \tag{1.3}$$

They can be analyzed with conventional, plane wave magnetotelluric techniques. Due to the transmitter power limitations, it is not always possible to produce measurable signals in the far field. Thus measurements are often made near the transmitter, where the electromagnetic fields have a 3-D geometry. Within a skin depth of the transmitter, the electric and magnetic fields vary as $1/r^3$ and $1/r^2$ respectively (for an HED transmitter), where r is the transmitter-receiver separation. Thus in this near field regime the apparent resistivity is proportional to r^2. On a logarithmic plot the variation of apparent resistivity with period is linear, while the phase approaches zero. Between the far field and the near field is the transition zone which exhibits intermediate behavior. The application of plane wave analysis techniques will yield incorrect estimates of the earth's conductivity structure in the transition zone and the

near field because of the 3-D nature of the electromagnetic fields. This geometrical complexity has hindered the development of inversion and modeling algorithms for CSAMT data as compared to the MT method, and the full potential of the technique has not been realized.

Since its introduction in the mid-1970s, CSAMT has become a powerful non-seismic exploration method and has been used in mineral and petroleum exploration, geothermal investigation, groundwater and seawater intrusion studies, and environmental geophysics. An excellent review of CSAMT and its applications is given by Zonge and Hughes (1991). However, CSAMT inversion and modeling algorithms are much less well developed than for MT data and the lack of the effective interpretation techniques greatly impedes the widespread use of CSAMT and makes the quality of CSAMT work questionable. A brief review of CSAMT interpretation techniques is given in Chapter 3. Therefore seeking an effective CSAMT interpretation technique has become a main research topic in EM geophysics, and is also the main topic of this dissertation.

1.3 Overview

This dissertation involves CSAMT forward modeling, inversion, the Fréchet derivative or sensitivity, and synthetic data and real data experiments. It is organized as follows.

Chapter 2 discusses the CSAMT forward modeling and presents some analytic and numerical results. It begins with the equations that govern the physics of CSAMT and a brief review of the previous work on EM forward modeling, then describes the finite element method for 2.5-D CSAMT forward problem developed by Unsworth et al (1993), which is extended to include the magnetic source. After this, analytic results are presented for horizontal electric and magnetic dipoles on the surface of a homogeneous half-space. At the end of the chapter, some numerical results computed with the technique of Unsworth (1993) are given for a two-dimensional model.

The inverse problem is the topic of Chapter 3. First, general inversion problems are discussed and a formulation of the 2-D inversion is described. Then, the rapid relaxation inversion (RRI) of MT is outlined extended to CSAMT. The key step to this extension is the Fréchet derivatives and sensitivities.

Chapter 4 focuses on the Fréchet derivatives and sensitivities. At the beginning of this chapter, methods of computing the Fréchet derivatives and sensitivities are introduced and RRI sensitivities are derived. Then the RRI technique is applied to derive sensitivities for CSAMT with electric and magnetic dipoles. Finally, comparison of CSAMT-RRI sensitivities with true sensitivities is made to justify the validity of CSAMT-RRI sensitivities on three models.

The inversion is tested on synthetic data and applied to a variety of field data in Chapter 5. The dissertation ends with conclusions and suggestions for future work in Chapter 6.

Chapter 2

CSAMT FORWARD MODELING

The goal of forward modeling is to predict the response of a given model provided that the relationship between these two is given. For any electromagnetic forward modeling, this relationship is provided by Maxwell's equations. Therefore, this chapter starts with derivation of the general CSAMT governing equations from the Maxwell's equations under some approximations; following is a review of previous work on EM forward modeling. The third section describes a forward modeling method which is used in our proposed CSAMT inversion. The fourth section gives analytic solutions of HED, HMD and FLHED for a homogeneous half-space. The fifth section presents some numerical results for a 2-D model.

2.1 Induction Equations

The fundamental differential equations governing the behavior of electromagnetic fields are given by Maxwell:

$$\nabla \times \mathbf{H} = \frac{\partial \mathbf{D}}{\partial t} + \mathbf{J} \tag{2.1}$$

$$\nabla \times \mathbf{E} = -\frac{\partial \mathbf{B}}{\partial t} \tag{2.2}$$

$$\nabla \cdot \mathbf{D} = \rho \tag{2.3}$$

$$\nabla \cdot \mathbf{B} = 0 \tag{2.4}$$

where $\mathbf{H}$ is the magnetic field in $Ampere/m$, $\mathbf{E}$ the electric field in $Volt/m$, $\mathbf{D}$ the electric displacement in $Coulomb/m^2$, $\mathbf{B}$ magnetic flux density in $Weber/m^2$, $\mathbf{J}$ the current density in $Ampere/m^2$, ρ the volume charge density in $Coulomb/m^3$, and bold

face letters represent vectors. Assuming that the medium is isotropic, the relations between these vectors are then given by

$$\mathbf{J} = \sigma\mathbf{E} \tag{2.5}$$

$$\mathbf{D} = \epsilon\mathbf{E} \tag{2.6}$$

$$\mathbf{B} = \mu\mathbf{H} \tag{2.7}$$

where σ is conductivity in $Siemens/m$, ϵ the dielectric constant in $Farad/m$, and μ the permeability in $Henry/m$. Resistivity is expressed in units of $ohm - m$.

At present, no magnetic charge has been found to exist in nature and Maxwell's equations contain only electric charges and currents. In practice, however, it is often convenient to use the concept of fictitious magnetic currents and charges. For example, a small current loop is shown to be equivalent to a magnetic current, which is used as a source to generate electromagnetic waves in CSAMT. If the fictitious magnetic current density $\mathbf{J}_m$ and charge density ρ_m are included, Maxwell's equations take the following symmetric form:

$$\nabla \times \mathbf{H} = \epsilon\frac{\partial\mathbf{E}}{\partial t} + \mathbf{J}_e \tag{2.8}$$

$$\nabla \times \mathbf{E} = -\mu\frac{\partial\mathbf{H}}{\partial t} - \mathbf{J}_m \tag{2.9}$$

$$\nabla \cdot \mathbf{D} = \rho_e \tag{2.10}$$

$$\nabla \cdot \mathbf{B} = \rho_m \tag{2.11}$$

Because of this symmetry, duality relationships exist (Ishimaru, 1991). For example, one can use the following transformation without affecting Maxwell's equations:

$$\mathbf{E} \rightarrow \mathbf{H}' \qquad \mathbf{J} \rightarrow \mathbf{J}'_m \qquad \rho \rightarrow \rho'_m \qquad \mu \rightarrow \epsilon'$$

$$\mathbf{H} \rightarrow -\mathbf{E}' \qquad \mathbf{J}_m \rightarrow -\mathbf{J}' \qquad \rho_m \rightarrow -\rho' \qquad \epsilon \rightarrow \mu'$$

Using this duality principle, when a solution is known for the unprimed fields, the solution for the primed fields can easily be obtained. The above duality relations between the primed fields and the unprimed fields are not the only ones that exist.

In Maxwell's equations, the current density and the charge density refer to all currents and charges, *source* and *induced*. It is often convenient to separate them into the source (or extrinsic) and the induced. For example, in CSAMT the current on the transmitting antenna is the *source current*, but the currents induced in the earth are considered the *induced current*. It is more convenient to express Maxwell's equations in the following manner:

$$\nabla \times \mathbf{H} = \epsilon\frac{\partial \mathbf{E}}{\partial t} + \mathbf{J} + \mathbf{J}_e^s \tag{2.12}$$

$$\nabla \times \mathbf{E} = -\mu\frac{\partial \mathbf{H}}{\partial t} - \mathbf{J}_m^s \tag{2.13}$$

$$\nabla \cdot \mathbf{D} = \rho + \rho_e^s \tag{2.14}$$

$$\nabla \cdot \mathbf{B} = \rho_m^s \tag{2.15}$$

where $\mathbf{J}$ and ρ are the induced current and the induced charge density, respectively. $\mathbf{J}$ and ρ can be incorporated into the medium characteristics.

In CSAMT, Maxwell's equations can be simplified by the following assumptions: (1) quasi-static electromagnetic fields: the displacement current term is negligible in the CSAMT working frequency range; (2) non-ferromagnetism: permeability of medium within the earth is approximately equal to the permeability of free space μ_0. The resultant Maxwell's equations become

$$\nabla \times \mathbf{H} = \sigma\mathbf{E} + \mathbf{J}_e^s \tag{2.16}$$

$$\nabla \times \mathbf{E} = i\omega\mu_0\mathbf{H} - \mathbf{J}_m^s \tag{2.17}$$

$$\nabla \cdot \mathbf{D} = \rho \tag{2.18}$$

$$\nabla \cdot \mathbf{B} = 0 \tag{2.19}$$

where time factor $e^{-i\omega t}$ is used, ω is angular frequency in *radians/second*, and $i = \sqrt{-1}$. Taking the curl of (2.17) and using (2.16), (2.18) and (2.19), one can get a second order partial differential equation for $\mathbf{E}$ alone

$$\nabla \times \nabla \times \mathbf{E} - i\omega\mu_0\sigma\mathbf{E} = i\omega\mu_0\mathbf{J}_e^s - \nabla \times \mathbf{J}_m^s \tag{2.20}$$

Then **H** can be computed from **E** by

$$\mathbf{H} = \frac{1}{i\omega\mu_0}\nabla \times \mathbf{E} \tag{2.21}$$

Similarly, **H** satisfies the following equation:

$$\nabla \times \nabla \times \mathbf{H} - i\omega\mu_0\sigma\mathbf{H} = -\sigma\mathbf{J}_m^s - \nabla \times \mathbf{J}_e^s \tag{2.22}$$

and **E** can be computed from

$$\mathbf{E} = \frac{1}{\sigma}\nabla \times \mathbf{H} \tag{2.23}$$

Solving Maxwell's equations (2.16) to (2.19) for **E** and **H** is equivalent to solving equations (2.20) and (2.21) or equations (2.22) and (2.23). Equations (2.20) and (2.22) are the two basic equations one needs to solve for **E** and **H**. It is important to recognize that they are diffusion equations, which lead to the attendant lack of resolution of electromagnetic prospecting methods. A number of techniques have been developed to solve (2.20) and (2.22). In the next section I will review previous work in the area of EM forward modeling.

2.2 *Review of Previous Work*

Forward solutions for 1-D models have been available for many years. The half-space case is reviewed in the book by Sommerfield (1949) and in the monograph by Banos (1966). Stratified media are treated by Wait (1953), Ward (1967), Kong (1972), Stoyer (1977), Tang (1979) and others. Forward modeling of a 2-D or 3-D conductivity model is more difficult. Analytic solutions do not generally exist for a 2-D or 3-D model except for certain simple geometries such as spheres and cylinders, where conductivity boundaries correspond to constant-coordinate surfaces. Therefore numerical solutions are sought for multi-dimensional models.

For multi-dimensional forward modeling, the simplest problem is that of a 2-D model excited by a 1-D or 2-D source such as a plane-wave natural EM field in the

MT method and a line source of current. A number of techniques for the 2-D forward problem in the frequency-domain have been developed. Jones and Price (1971) presented a finite-difference solution and Swift (1971) discussed a network analogy formulation of a finite-difference solution. Coggon (1971) discussed a finite-element formulation using a variational approach. Hohmann (1971) and Parry and Ward (1971) developed volume and surface integral equation solutions, respectively. Silvester and Haslam (1972) presented a finite-element solution based on the method of weighted residuals. In the time-domain, Kuo and Cho (1980) obtained an explicit solution based on finite-element discretization in space and a finite-difference approximation in time. Goldman and Stoyer (1983) formulated an implicit finite-difference transient solution. Oristaglio and Hohmann (1984) presented an explicit finite-difference solution. Because of the 3-D nature of the CSAMT transmitter, 2-D modeling is not completely adequate in CSAMT inversion. Lu *et al.* (1997) used infinite-length line source in HED CSAMT data inversion and observed some artifacts in inversion model.

Modeling a 2-D earth and a 3-D source is the next step of complexity. Coggon (1971) first published a finite-element derivation for this so-called 2.5-D electromagnetic problem and some results for the DC resistivity and induced polarization problems. Stoyer and Greenfield (1976) used a finite-difference method to compute the response of a 2-D earth to a vertical magnetic dipole source. Lee (1978) and Lee and Morrison (1985) presented a finite-element solution for the fields induced by a magnetic dipole over a 2-D earth. Unsworth *et al.* (1993) developed a finite-element method to model electromagnetic induction by an electric dipole source over a 2-D earth. In the time domain, Everett (1990) described a solution for a transient seafloor exploration system, Moghaddam *et al.* (1991) presented a solution for ground-penetrating radar, and Sugeng and Raiche (1992) modeled the 2.5-D responses for a wide range of time-domain EM systems. 2.5-D modeling is a practical approach to compromise computation and model complexity. Fully 3-D modeling techniques

would approach the real situation more closely, because real earth conductivity varies in 3-D.

3-D forward modeling dates back to the early 1970's. Solutions to 3-D modeling were first formulated by using the volume integral equation method (Raiche, 1974; Hohmann, 1975; Weidelt, 1975). Since then a lot of effort has gone into the integral equation method (Ting and Hohmann, 1981; Wannamaker *et al.*, 1984, 1991; Newman *et al.*, 1986; Xiong, 1992). Finite-difference formulations are discussed by Lines and Jones (1973), Zhdanov *et al.* (1982), and Adhidjaja and Hohmann (1989). Reddy *et al.* (1977) published 3-D MT results based on a finite-element method. Pridmore *et al.* (1981) presented a 3-D finite-element solution for controlled source EM applications. Some hybrid approachs have been developed by combining differential-equation solutions and integral-equation solutions as a means of limiting mesh size (Lee *et al.*, 1981; Best *et al.*, 1985). Recently, Wang and Hohmann (1993), Mackie *et al.* (1993) and Smith (1996) have introduced staggered grids into 3-D modeling problems of EM induction to enforce conservation laws. More recent developments of 3-D EM modeling are covered in the monograph edited by Oristaglio and Spies (1995).

3-D EM modeling is still a challenge for any numerical method. The limitations arise in part because of restrictions on computer memory and speed and also because of the inadequacies of numerical approximations used to represent continuous fields. The integral equation method has been studied extensively primarily because it requires discretization in the anomalous region only, but it lacks flexibility in terms of the structures that can be modeled. The finite-difference method and the finite-element method are better suited to modeling arbitrarily complex geometries, but they require large grids, which often result in unreasonable amounts of computer time and storage.

The forward problem I will address is to model the electromagnetic response of 2-D conductivity structures to 3-D electromagnetic waves and is discussed in the next section.

2.3 2.5-D EM forward modeling

I use the finite-element method developed by Unsworth *et al.* (1993) for forward modeling to exploit its efficiency, accuracy and flexibility for various sources. The following derivation largely follows Unsworth *et al.* (1993), but extends it to include more complex magnetic sources such as magnetic dipoles.

2.3.1 Formulation

Maxwell's equations (2.16) and (2.17) can be rewritten as

$$\nabla \times \mathbf{B} = \mu_0 \sigma \mathbf{E} + \mu_0 \mathbf{J}_e^s \tag{2.24}$$

$$\nabla \times \mathbf{E} = i\omega \mathbf{B} - \mathbf{J}_m^s \tag{2.25}$$

where $\sigma = \sigma(y, z)$ is assumed to vary in two dimensions, with x aligned with strike, y perpendicular to strike and z positive downward (hereafter, I will use this coordinate system unless otherwise specified).

If the fields due to a specific resistivity model $\sigma_0(y, z)$ are defined as primary fields and the fields due to model $\sigma(y, z)$ are defined as total fields, then their differences are the secondary fields. Equations (2.24) and (2.25) govern both the primary fields when $\sigma = \sigma_0(y, z)$ and total fields when $\sigma = \sigma(y, z)$. Thus equations for the secondary fields are:

$$\nabla \times \mathbf{B}^s = \mu_0 \sigma(y, z) \mathbf{E}^s + \mu_0 \Delta\sigma(y, z) \mathbf{E}^p \tag{2.26}$$

and

$$\nabla \times \mathbf{E}^s = -\frac{\partial \mathbf{B}^s}{\partial t} \tag{2.27}$$

where $\mathbf{E}^s$ and $\mathbf{B}^s$ are the secondary electric field and magnetic induction, $\mathbf{E}^p$ is the primary electric field, and $\Delta\sigma(y, z) = \sigma(y, z) - \sigma_0(y, z)$. Note that the nature of the source is introduced here by the primary field just in places where the total model departs from the primary model. Also, note that by separating the total electric and

magnetic fields into their primary and secondary components, the method removes the singularity in **E** and **B** at the location of the current sources $\mathbf{J}_e^s$ and $\mathbf{J}_m^s$, and has the advantage of directly calculating secondary quantities. The primary fields can be calculated for a simple conductivity structure. Appendix A gives primary fields for a half-space with various sources.

By Fourier transforming each field component in the x-direction, the dimensionality of computation can be reduced from 3 to 2. The Fourier transforms are defined as

$$\hat{F}(k_x, y, z) = \int_{-\infty}^{\infty} dx\, e^{ik_x x} F(x, y, z) \tag{2.28}$$

and

$$F(x, y, z) = \frac{1}{2\pi} \int_{-\infty}^{\infty} dk_x e^{-ik_x x} \hat{F}(k_x, y, z) \tag{2.29}$$

where k_x is the along-strike wavenumber; a hat ($\wedge$) is used to denote quantities in the Fourier transform domain. In Cartesian form, equations (2.26) and (2.27) can be expanded as

$$-ik_x \hat{E}_y^s - \partial_y \hat{E}_x^s - i\omega \hat{B}_z^s = 0 \tag{2.30}$$

$$\partial_y \hat{B}_z^s - \partial_z \hat{B}_y^s - \mu_0 \sigma \hat{E}_x^s = \mu_0 \delta\sigma \hat{E}_x^p \tag{2.31}$$

$$\partial_z \hat{E}_x^s + ik_x \hat{E}_z^s - i\omega \hat{B}_y^s = 0 \tag{2.32}$$

$$-ik_x \hat{B}_y^s - \partial_y \hat{B}_x^s - \mu_0 \sigma \hat{E}_z^s = \mu_0 \delta\sigma \hat{E}_z^p \tag{2.33}$$

$$\partial_y \hat{E}_z^s - \partial_z \hat{E}_y^s - i\omega \hat{B}_x^s = 0 \tag{2.34}$$

$$\partial_z \hat{B}_x^s + ik_x \hat{B}_z^s - \mu_0 \sigma \hat{E}_y^s = \mu_0 \delta\sigma \hat{E}_y^p \tag{2.35}$$

If the source is invariant in the x-direction (2-dimensional with $k_x = 0$) as in MT or for an infinite-length line source, equations (2.30) to (2.35) can be grouped into two "modes". Equations (2.30) to (2.32) define the transverse electric (TE) mode, which only has an electric component in the invariant x-direction. Equations (2.33) to (2.35) define the transverse magnetic (TM) mode, which only has a magnetic component in the invariant x-direction. For a finite source, a number of nonzero k_x

values have to be considered in the Fourier domain. TE and TM modes are no longer independent but coupled by the variation of the source in the x-direction. One can view the zero-wavenumber problems (2-D source) as a first-order approximation to the non-zero-wavenumber problems (3-D source). Therefore, the solution of the problem with a 2-D source gives useful physical insight into electromagnetic induction, but the results must be applied cautiously to the interpretation of data from 3-D sources, since the reduction in dimension fails to represent the complete induction process.

Equations (2.30) to (2.35) may be rearranged to yield coupled equations for $\hat{E}_x^s$ and $\hat{B}_x^s$, the secondary along-strike fields in the Fourier domain.

$$\nabla \cdot \left(\frac{\mu_0 \sigma \nabla \hat{E}_x^s}{\gamma^2} \right) - \mu_0 \sigma \hat{E}_x^s = \mu_0 \delta \sigma \hat{E}_x^p - i k_x \nabla \cdot \left(\frac{\delta \sigma \hat{\mathbf{E}}^p}{\gamma^2} \right) +$$
$$+ i k_x \left[\nabla \hat{B}_x^s \times \nabla \left(\frac{1}{\gamma^2} \right) \right] \cdot \mathbf{x} \qquad (2.36)$$

$$\nabla \cdot \left(\frac{i\omega \nabla \hat{B}_x^s}{\gamma^2} \right) - i\omega \hat{B}_x^s = i\omega \mu_0 \nabla \times \left(\frac{\delta \sigma \hat{\mathbf{E}}^p}{\gamma^2} \right) \cdot \mathbf{x} +$$
$$+ i k_x \left[\nabla \hat{E}_x^s \times \nabla \left(\frac{1}{\gamma^2} \right) \right] \cdot \mathbf{x} \qquad (2.37)$$

where $\gamma^2 = k_x^2 - i\omega \mu_0 \sigma$, $\mathbf{x}$ is a unit vector in the x-direction and $\nabla = (0, \partial_y, \partial_z)$. Note that these two equations are coupled through a non-zero k_x. With a non-zero wavenumber, a minimum of two field components must be computed at a point to represent the electromagnetic fields of a 3-D source, whereas only one suffices for the zero-wavenumber case or a 2-D source. The other field components can then be calculated by numerical differentiation of $\hat{E}_x^s$ or/and $\hat{B}_x^s$. To avoid the errors from differentiation, Coggon (1971) and Lee and Morrison (1985) solved directly for all three electric field components, but this approach increases the size of the matrix equations by 50 percent. Equations (2.36) and (2.37) could be solved simultaneously for $\hat{E}_x^s$ or/and $\hat{B}_x^s$, but an iterative approach is more efficient to solve the coupled equations. The iteration process is: (1) the coupling terms are kept on the right-hand

sides of the equations as a source term; (2) then $\hat{B}_x^s$ is set to be zero and equation (2.36) is solved for an initial $\hat{E}_x^s$; (3) $\hat{E}_x^s$ is then used to update $\hat{E}_x^s$ in the source term in equation (2.37) to compute $\hat{B}_x^s$; (4) finally $\hat{B}_x^s$ is used to improve the approximation to $\hat{E}_x^s$. This process is repeated until convergence is achieved, which is defined as occurring when both the mean and maximum change in the secondary fields at the earth's surface are less than some specified amount.

Once the secondary fields $\hat{E}_x^s$ and $\hat{B}_x^s$ are obtained, the primary and secondary fields are added to yield the total electromagnetic field components in the x-direction. Then the other two horizontal components can be computed by

$$\hat{B}_y(k_x, y, z) = \frac{1}{(i\omega\mu\sigma - k_x^2)} \left(\mu\sigma \frac{\partial \hat{E}_x(k_x, y, z)}{\partial z} + ik_x \frac{\partial \hat{B}_x(k_x, y, z)}{\partial y} \right) \qquad (2.38)$$

$$\hat{E}_y(k_x, y, z) = \frac{1}{(i\omega\mu\sigma - k_x^2)} \left(ik_x \frac{\partial \hat{E}_x(k_x, y, z)}{\partial y} + i\omega \frac{\partial \hat{B}_x(k_x, y, z)}{\partial z} \right) \qquad (2.39)$$

Finally, the EM fields in the (x, y, z) domain are computed by using the inverse Fourier transform (2.29).

2.3.2 The finite element method

The 2.5-D EM induction problem has been formulated in terms of two differential equations (2.36) and (2.37) that are solved subject to a given set of boundary conditions. The following outlines how the finite-element method is used to solve the two partial differential equations for $\hat{E}_x^s$ or $\hat{B}_x^s$. This formulation may be written in general mathematical notations as

$$\mathcal{D}V = f \qquad in \qquad \Omega \qquad (2.40)$$

and boundary conditions

$$V = f_0 \qquad on \qquad \partial\Omega \qquad (2.41)$$

where $\mathcal{D}$ is a differential operator, V is a field, Ω is a specified region, f is the source term, f_0 is a known function on $\partial\Omega$, $\partial\Omega$ is the boundary of the region Ω.

The calculus of variations shows that solving the differential equation is equivalent to finding a function V that minimize the Lagrangian $\mathcal{L}$ (Clegg, 1968)

$$\mathcal{L} = \int_\Omega L(V, \partial_y V, \partial_z V) dy dz \tag{2.42}$$

where L, the Lagrange density, satisfies the Euler-Lagrange equation,

$$\partial_y \left[\frac{\partial L}{\partial(\partial_y V)} \right] + \partial_z \left[\frac{\partial L}{\partial(\partial_z V)} \right] = \frac{\partial L}{\partial V} \tag{2.43}$$

Equations (2.36) and (2.37) are of the form

$$-\nabla \cdot (a(y,z)\nabla V) + b(y,z)V = f(y,z) \tag{2.44}$$

which has Lagrange densities of the form

$$L = \frac{a}{2}(\partial_y V)^2 + \frac{a}{2}(\partial_z V)^2 + \frac{bV^2}{2} + fV \tag{2.45}$$

Thus solving a differential equation problem is transformed to minimizing the functional $\mathcal{L}$ of equation (2.42). This alternative formulation provides a convenient way of implementing a finite-element scheme.

The detailed description of the finite-element method can be found in Zienkowicz (1967) and Oden and Carey (1983) and a brief description is outlined here. The region Ω is divided into N_e elements, and the kth element is defined by $n(k)$ nodes with coordinates $(y_i, z_i), i = 1, ..., n(k)$. The mesh contains N_n nodes in total. The solution V is expressed within element k as

$$V_k(y, z) = \sum_{i=1}^{n(k)} v_i \psi_i(y, z) \tag{2.46}$$

where v_i is the value at node i of the element k, ψ_i is a set of basis functions, $i = 1, ..., n(k)$, which are also called the element shape functions. Then equation (2.42) can be rewritten as a sum of integrals over each element,

$$\mathcal{L} = \sum_{k=1}^{N_e} \int_{\Omega_{Bk}} L(V, \partial_y V, \partial_z V) dy dz \tag{2.47}$$

where Ω_{Ek} is the kth element. Substituting for L and V from equations (2.45) and (2.46), gives

$$\mathcal{L} = \sum_{k=1}^{N_e} \left\{ \int_{\Omega_{Bk}} \left[\frac{a}{2} \left(\sum_{j}^{n(k)} v_j \partial_y \psi_j \right)^2 + \frac{a}{2} \left(\sum_{j}^{n(k)} v_j \partial_z \psi_j \right)^2 + \right. \right.$$
$$\left. \left. + \frac{b}{2} \left(\sum_{j}^{n(k)} v_j \psi_j \right)^2 + f \sum_{j}^{n(k)} v_j \psi_j \right] dydz \right\} \tag{2.48}$$

The basis functions, if they are independent of the nodal values, are required to have the property that

$$\psi_i = \delta_{ij} \quad at \quad (y_j, z_j) \tag{2.49}$$

where (y_j, z_j) are the nodal points, $i, j = 1, ..., n(k)$, and δ is the Kronecker delta. Then the contribution to $\mathcal{L}$ from each element can be written in quadratic form as

$$\mathcal{L}_e = \mathbf{v}_e^T \mathbf{K}_e \mathbf{v}_e - \mathbf{v}_e^T \mathbf{f}_e \tag{2.50}$$

where $\mathbf{v}_e$ is the vector containing the node values, T denotes the conjugate transpose, $\mathbf{K}_e$ is the element stiffness matrix given by

$$K_{ij} = \int_{\Omega_B} \left[\frac{a}{2} (\partial_y \psi_i)(\partial_y \psi_j) + \frac{a}{2} (\partial_z \psi_i)(\partial_z \psi_j) + \frac{b}{2} \psi_i \psi_j \right] dydz \quad i, j = 1, ..., n(k), \tag{2.51}$$

and $\mathbf{f}_e$ is the element load vector with components

$$f_i = \int_{\Omega_B} f \psi_i dydz \quad i = 1, ..., n(k). \tag{2.52}$$

The Lagrangian $\mathcal{L}$ can be obtained by summing over all elements and it can be written

$$\mathcal{L} = \mathbf{v}^T \mathbf{K} \mathbf{v} - \mathbf{v}^T \mathbf{f} \tag{2.53}$$

where $\mathbf{v} = [v_1, ..., v_{Nn}]$ is the global solution vector of nodal values, $\mathbf{K} = \sum_{i=1}^{N_e} \mathbf{K}_e$ is the global stiffness matrix and $\mathbf{f} = \sum_{i=1}^{N_e} \mathbf{f}_e$ is the global load vector. $\mathbf{K}$ contains all of the information regarding the element sizes and media properties (a and b).

To minimize $\mathcal{L}$ with respect to v, equation (2.53) is differentiated with respect to **v** and equated to zero, yielding the matrix equation,

$$\mathbf{Kv} = \mathbf{f} \qquad (2.54)$$

which can be solved for **v**.

2.4 The analytical solution for a homogeneous half space

Computing the electromagnetic fields of an EM source in a conducting medium is of direct practical importance in geophysics. It helps us not only to understand the nature of EM fields, but also to provide information for optimal survey layout to resolve a specific target. The horizontal electric dipole (HED), the horizontal magnetic dipole (HMD), and the finite-length HED (FLHED) are among the most commonly-used artificial sources in practice. In this section, first, I will briefly review MT methodology since CSAMT is closely related to MT and they share many technical terms. Second, I will study the EM fields on the surface of a homogeneous half space from HED, HMD and FLHED.

2.4.1 MT methodology

MT uses natural sources, which may be assumed to be 1-dimensional plane waves outside the earth. For a homogeneous half space, EM fields are uniform laterally. If the electric field is in the x direction, then the magnetic field has only a y component. From equations (2.20) and (2.22), the governing equations are

$$\frac{\partial^2 E_x}{\partial z^2} - k^2 E_x = 0 \qquad (2.55)$$

$$\frac{\partial^2 H_y}{\partial z^2} - k^2 H_y = 0 \qquad (2.56)$$

The solution of equations (2.55) and (2.56) are given by

$$E_x(z) = E_{x0} e^{-ikz} \qquad (2.57)$$

$$H_y(z) = \frac{k}{\omega\mu_0}E_{x0}e^{-ikz} \qquad (2.58)$$

where $k = (1 - i)\sqrt{\omega\mu_0\sigma/2}$ is the complex wave number in the medium and E_{x0} is the horizontal electrical field at the surface. Note that the strength of the fields decreases exponentially as their depth increases due to the transformation of electromagnetic energy into heat. The field strength is attenuated by $1/e$ or 63% percent of the original field strength at a depth equal to the skin depth δ, which is given by

$$\delta = \sqrt{\frac{2}{\omega\mu_0\sigma}} \qquad (2.59)$$

Equation (2.59) can be written in terms of resistivity as

$$\delta = 503\sqrt{\frac{\rho}{f}} \qquad (meters) \qquad (2.60)$$

Skin depth is a very useful concept. It is dependent on two parameters: the resistivity of the earth and the frequency of the signal. Skin depth is smaller with decreasing resistivities and increasing frequencies. Conversely, it is larger with increasing resistivities and decreasing frequencies. Figure (2.1) shows the skin depth as a function of the earth resistivity and the signal frequency. If the Earth's resistivity varies from 1 to 10^4 Ωm and the frequency of EM data varies from about 1 to 10^4 Hz, then EM penetration varies from tens of meters to tens of kilometers.

In order to draw useful information about the Earth's resistivity structure from the measurement at the surface, $z = 0$, the ratio of orthogonal E to H is used and defined as impedance

$$Z = \frac{E}{H} \qquad (2.61)$$

Then, by equations (2.57) and (2.58), the impedance Z_{xy} is given by

$$Z_{xy} = \sqrt{-i\omega\mu\rho} \qquad (2.62)$$

Impedance is a function of the resistivity of the earth and the frequency. Simple algebra gives the true resistivity of the half space in terms of the impedance

$$\rho = -\frac{1}{i\omega\mu_0}Z_{xy}^2 \qquad (2.63)$$

Therefore measuring orthogonal electrical and magnetic fields at the Earth surface can be used to infer electric resistivity inside of the Earth. If the electric field is in the y direction and then magnetic field is in the x direction, one can readily see from the above derivation that

$$Z_{yx} = \frac{E_y}{H_x} = -\sqrt{-i\omega\mu\rho}$$ (2.64)

For a uniform half space and a 1-D earth

$$Z_{xy} = -Z_{yx}$$ (2.65)

For more complex structure, the quantity on the right hand side of equation (2.63) still reflects a volume average of the resistivities within about one skin depth below the measurement point. The magnitude of the impedance can be used to define apparent resistivity and its argument is defined as the phase,

$$\rho_a = \frac{1}{\omega\mu_0}|Z|^2$$ (2.66)

$$\phi = Arg\{Z\}$$ (2.67)

ρ_a (also called the Cagniard resistivity) and ϕ are the two main parameters used to extract resistivity structure information from measured data.

2.4.2 EM fields of a horizontal electric dipole

One commonly-used controlled source is the horizontal electric dipole, which is an insulated wire grounded at each end. Electric and magnetic field components in a half space conducting medium due to an HED aligned in the x-direction on the surface of the medium are given in Appendix A. On the surface, the horizontal components can be simplified to

$$E_x = \frac{Idl}{2\pi r^3 \sigma}\left[3\cos^2\phi - 2 + (1 + ikr)e^{-ikr}\right]$$ (2.68)

$$E_y = \frac{Idl}{2\pi r^3 \sigma}3\cos\phi\sin\phi$$ (2.69)

$$H_x = \frac{Idl}{4\pi r^2} \sin\phi \cos\phi \left[ikr(I_0 K_1 - I_1 K_0) - 8I_1 K_1\right] \qquad (2.70)$$

$$H_y = \frac{Idl}{2\pi r^2} \left[(1 - 4\sin^2\phi)I_1 K_1 + \frac{ikr}{2}\sin^2\phi(I_0 K_1 - I_1 K_0)\right] \qquad (2.71)$$

where the I_m and K_m represent modified Bessel functions of the mth order with argument $ikr/2$ and ϕ is the angle from the x-direction (Figure 2.2). The electric and magnetic components are dependent on r, the separation between the source and the receiver, and on medium resistivity and frequency. Investigating EM field variation as a function of the separation between the source and the receiver gives one an understanding of the fields.

Near-Field

This region is very close to the HED at much less than one skin depth ($r \ll \delta$ or $|kr| \ll 1$). Equations (2.68) to (2.71) can be simplied by taking the limit $|kr| \to 0$

$$E_x = \frac{Idl}{2\pi r^3 \sigma}(3\cos^2\phi - 1) \qquad (2.72)$$

$$E_y = \frac{Idl}{2\pi r^3 \sigma}3\cos\phi\sin\phi \qquad (2.73)$$

$$H_x = \frac{Idl}{4\pi r^2}\sin\phi\cos\phi \qquad (2.74)$$

$$H_y = \frac{Idl}{4\pi r^2}(2\cos^2\phi - 1) \qquad (2.75)$$

We see that for a homogeneous half space, both electric field (E_x and E_y) and magnetic field (H_x and H_y) are independent of frequency, and so is the impedance. Electric field is inversely proportional to ground conductivity, but magnetic field is independent of conductivity. H_x and H_y are independent of ground conductivity and frequency. Such H_x and H_y are said to be "saturated". Since the electric and magnetic fields vary as $1/r^3$ and $1/r^2$, respectively, the apparent resistivity in the near-field is proportional to r^2. This demonstrates that near-field measurements are controlled by survey geometry, not frequency. The apparent resistivity increases with a slope of 45 degrees on a log-log plot, while the phase approaches zero (Figure 2.3).

This phenomenon is often called the "source effect". Sometimes, any deviation from the MT responses, caused by the introduction of the artificial source is attributed to the source effect.

Far Field

Far away from the HED source ($r \gg \delta$ or $|kr| \gg 1$), equations (2.68) to (2.71) have the following form

$$E_x = \frac{Idl}{2\pi r^3 \sigma}(3\cos^2 \phi - 2) \tag{2.76}$$

$$E_y = \frac{Idl}{2\pi r^3 \sigma}3\cos \phi \sin \phi \tag{2.77}$$

$$H_x = -\frac{Idl}{2\pi r^3 ik}3\sin \phi \cos \phi \tag{2.78}$$

$$H_y = \frac{Idl}{2\pi r^3 ik}(3\cos^2 \phi - 2) \tag{2.79}$$

Equations (2.76) to (2.79) show that, in the far field, E_x and E_y are independent of frequency and are inversely proportional to ground conductivity as in the near-field, but H_x and H_y depend on k and therefore on ground conductivity as well as frequency. The horizontal field components all decay as $1/r^3$. Impedance in the far field can be obtained from (2.76) to (2.79)

$$Z_{xy} = \frac{E_x}{H_y} = \sqrt{-i\omega\mu\rho} \tag{2.80}$$

and

$$Z_{yx} = \frac{E_y}{H_x} = -\sqrt{-i\omega\mu\rho} \tag{2.81}$$

These impedances are same as those defined for MT. Since (2.76) to (2.79) are obtained with the limitation $r \to \infty$, EM fields in this region can be taken as uniform plane wave. Since CSAMT and MT have the same impedances (Figure 2.3) in the far field, definitions (2.66) and (2.67) for apparent resistivity and phase are also valid for CSAMT in the far field. Apparent resistivity and phase are again the two most

commonly-used parameters in CSAMT data interpretation, which maintains the similarity between CSAMT and MT. In MT, the use of impedance cancels the unknown natural source field.

Apparent resistivity and phase presented in pseudo-section format have a visual relationship to the electric structure, but apparent resistivity and phase pseudosections for CSAMT will have a source-effect at low frequencies and near the transmitter. For CSAMT, electric and magnetic fields can also be used to recover a conductivity model, but they have no easily visualized relationship with conductivity structure below the measurement site and their magnitudes are dependent on the source as well as conductivity structure.

Transition Zone

This is the region between the near-field and far-field zones ($r \approx \delta$ or $|kr| \approx 1$). The exact electric and magnetic fields and impedance Z can be computed by using equations (2.68) to (2.71). E decays as $1/r^3$ and H decays at a rate between $1/r^2$ and $1/r^3$. Data in this zone are transitional from near-field to far-field behavior (Figure 2.3).

EM fields, apparent resistivities and phases

Figure (2.4) shows the horizontal EM field components, apparent resistivities and phases for an HED on a 100 Ωm half space at frequency 64 Hz. The HED, an infinitesimal dipole with unit moment, is located at the origin and directed in the x-direction. The plots are presented for one quadrant only. The other quadrants follow from the symmetry.

Figures 2.4a and 2.4e show the behavior of the horizontal electric components E_x and E_y. The E-field parallel to the HED, E_x, shows a double-lobed appearance. The lobes are separated by a "null" zone in which E_x goes to zero. The flip in the orientation of E_x causes this null zone, which is about at 35° from the HED direction.

The orientation flip means that the direction of E_x changes from the positive x-direction to negative, or vice versa. E_x values along the x-axis are about half the E_x values along the y-direction. This difference in signal strength is one of the features that makes E_x measurements in the broadside configuration more preferable than the collinear one. The E_y plot, which is the electric component perpendicular to the HED, has a single uniform lobe appearance except along the x and y axes, where the field strength drops off sharply. The single uniform lobe appearance indicates that E_y always has the same orientation in each quadrant. E_y has the strongest signal at an azimuth of 45°.

Figures 2.4b and 2.4f show magnetic fields H_y and H_x, which are very similar to E_x and E_y, respectively. This similarity can be verified by comparing the formulas for near-field and far-field responses.

Figures 2.4c and 2.4d show the apparent resistivity ρ_{xy} and phase ϕ_{xy}. Because of the double-lobed appearance of E_x and H_y, the appearances of ρ_{xy} and ϕ_{xy} are more complicated than those of ρ_{yx} and ϕ_{yx}. The apparent resistivity ρ_{xy} is very close to the true resistivity value at $r > 4\delta$ for broadside measurements and at $r > 5\delta$ for collinear measurements. However the phase ϕ_{xy} converges to 45° at $r > 5\delta$ for broadside configuration and at $r > 6\delta$ for collinear configuration. The computation along the 35° null zone is not accurate because the fields flip their orientations in this zone. So the values of ρ_{xy} and ϕ_{xy} along the null zone are less accurate than others. Also note that the effective null zone for ρ_{xy} and ϕ_{xy} are larger near to the source than far away from the source. This is because the zones where E_x and H_y flip are not exactly the same near to the source, but are the same far away from the source.

The apparent resistivity and phase computed from E_y and H_x are shown in Figures 2.4g and 2.4h. Since E_y and H_x both have a single uniform lobe appearance, it is predictable that the apparent resistivity ρ_{yx} and phase ϕ_{yx} are much the same, with the data along the x and y axes being undefined due to the null zones for E_y and H_x. The apparent resistivity is very close to the true resistivity of the half space for

$r > 3\delta$, whereas the phase is about $45°$ for $r > 4\delta$.

2.4.3 EM fields of a horizontal magnetic dipole

The HMD technique is studied less. From the derivation in Appendix A, horizontal components on the surface are given by

$$E_x = -\frac{i\omega\mu_0 m}{2\pi r^2}\sin\phi\cos\phi\left[-4I_1K_1 + \frac{ikr}{2}(I_0K_1 - I_1K_0)\right] \qquad (2.82)$$

$$E_y = \frac{i\omega\mu_0 m}{2\pi r^2}\left[(1 - 4\cos^2\phi)I_1K_1 + \frac{ikr}{2}(I_0K_1 - I_1K_0)\cos^2\phi\right] \qquad (2.83)$$

$$H_x = -\frac{m}{2\pi r^5 k^2}\left\{3 + k^2r^2 - (3 + 3ikr - k^2r^2)e^{-ikr} + \cos^2\phi\left[-15 - 3k^2r^2 + \right.\right.$$
$$\left.\left. + (-ik^3r^3 - 6k^2r^2 + 15ikr + 15)e^{-ikr}\right]\right\} \qquad (2.84)$$

$$H_y = \frac{m}{2\pi r^5 k^2}\sin\phi\cos\phi\left[15 + 3k^2r^2 - (-ik^3r^3 - 6k^2r^2 + 15ikr + 15)e^{-ikr}\right] \qquad (2.85)$$

where m is magnetic dipole moment, r and ϕ are same as in Figure 2.2.

Note that, by comparing them with equations (2.68) to (2.71) for the HED, E and H of an HMD are similar to their counterparts of H and E for HED, respectively. This can be understood from the duality of Maxwell's equations for the HED and HMD. The similarity will be more obvious when one investigates EM fields in the near-field and far-field zones.

Near-Field

In the near field, $r \ll \delta$ or $|kr| \ll 1$. The limit of equations (2.82) to (2.85) for small kr is

$$E_x = -\frac{i\omega\mu_0 m}{2\pi r^2}\sin\phi\cos\phi \qquad (2.86)$$

$$E_y = \frac{i\omega\mu_0 m}{4\pi r^2}(1 - 2\cos^2\phi) \qquad (2.87)$$

$$H_x = -\frac{m}{4\pi r^3}(1 - 3\cos^2\phi) \qquad (2.88)$$

$$H_y = \frac{m}{4\pi r^3}3\sin\phi\cos\phi \qquad (2.89)$$

When comparing these equations with the equations for HED, some differences are observed. For an HMD, both electric and magnetic fields are independent of earth resistivity, so the measurement in this region is non-responsive to the ground resistivity. Furthermore, the near-field E_x and E_y vary with frequency and are not a function of resistivity, whereas for an HED, E_x and E_y are independent of frequency but are a function of resistivity. For the HMD, E and H vary as $1/r^2$ and $1/r^3$, respectively, while E and H vary as $1/r^3$ and $1/r^2$ for the HED. Therefore, for HMD, the apparent resistivity decreases with a 45 degree slope in log-log plot and phase approaches 90 degrees (Figure 2.5). The appearance of the source effect for the HED and HMD is opposite. H_x and H_y remain independent of both frequency and resistivity for both cases.

Far Field

Equations (2.82) to (2.85) can be simplied for the far-field ($r \gg \delta$ or $|kr| \gg 1$) to

$$E_x = \frac{\omega\mu_0 m}{2\pi r^3 k} 3 \sin\phi \cos\phi \qquad (2.90)$$

$$E_y = \frac{\omega\mu_0 m}{2\pi r^3 k}(1 - 3\cos^2\phi) \qquad (2.91)$$

$$H_x = -\frac{m}{2\pi r^3}(1 - 3\cos^2\phi) \qquad (2.92)$$

$$H_y = \frac{m}{2\pi r^3} 3 \sin\phi \cos\phi \qquad (2.93)$$

In far field, for the HMD, the electric fields (E_x and E_y) are a function of both frequency and resistivity, but E_x and E_y are independent of frequency for HED. For an HMD, the magnetic fields (H_x and H_y) are independent of both frequency and resistivity, whereas the magnetic field of an HED is dependent of both frequency and resistivity. Both electric and magnetic fields from the HMD decay as $1/r^3$ as in HED. Similarly, apparent resistivity is equal to the true resistivity and phase is 45 degree for a half space (Figure 2.5).

EM fields, apparent resistivities and phases

Figure 2.6 shows the horizontal EM field components, apparent resistivities and phases from an HMD for a $100\Omega m$ half space at frequency $64Hz$. The HMD is located at the origin and directed in the x-direction.

Figures 2.6a and 2.6e show the horizontal electric components E_x and E_y, which are very similar to E_y and E_x for the HED. However, the null zone for E_y for the HMD is at about 55°, rather than 35° of E_x for HED.

Magnetic fields H_x and H_y are shown in figures 2.6f and 2.6b. They are also similar to H_y and H_x of HED. Similarly, H_x's null zone is about 55°. Note that the EM fields from a unit HMD are much smaller than those from an HED, because HED has grounded electrodes to inject electric current into the earth and is coupled with the earth tightly, whereas an HMD is insulated from the earth and electromagnetic waves transmitted by an HMD will be partially reflected back to air. HMD is weakly coupled with the earth. For this reason, a horizontal magnetic dipole normally has less transmitting power than HED, but is safer without grounded electrodes. HMD is not used as commonly as HED.

Figures 2.6c and 2.6d show the apparent resistivity ρ_{xy} and phase ϕ_{xy}. Apparent resistivity is very close to the true resistivity of the half space for $r > 4 \sim 5\delta$, whereas the phase is about 45° for $r > 5\delta$. Figures 2.6g and 2.6h show the apparent resistivity ρ_{yx} and phase ϕ_{yx}. The apparent resistivity ρ_{yx} is very close to the true resistivity value at $r > 4\delta$ for broadside measurements and at $r > 5\delta$ for collinear measurements. The phase ϕ_{yx} is about 45° at $r > 5\delta$ for broadside configuration and at $r > 6\delta$ for collinear configuration.

2.4.4 EM fields of a finite-length horizontal electric dipole

The HED is an approximation to a real CSAMT electric source. In practice, a real CSAMT electric source is composed of a finite length of grounded wire. If the source-

receiver separation is large enough, a grounded wire may be approximated as an electric dipole. But often, to overcome noise and improve signal-noise ratio, either a long grounded wire source is used or receivers are close to the grounded wire. Then the approximation of a point dipole may not be valid. Then the length of a long grounded wire source has to be considered. In this section I will investigate EM fields on the surface of a homogeneous half-space from an x-directed finite-length horizontal electric dipole source and the effect of length on measurements. Unfortunately, no closed formula is available for the EM field on the surface of the earth from a finite-length horizontal electric dipole source. Therefore, analysis is based on numerical results using formulas in Appendix A.

Figures 2.7, 2.8, 2.9, 2.10, 2.11, and 2.12 show the EM fields, apparent resistivities and phases for line sources with the lengthes of 1, 2, 3, 4, 6, and 10 skin depths, respectively.

Comparing these figures with Figure 2.4, some features can be observed. The deviations from an HED are larger as the length is increased. When the length is less than 2-3 skin depths, EM fields, apparent resistivities and phases are quite close to those from an HED, whereas when the length is 10 skin depths, they appear to be very close to those from an infinite-length line source in the area between the two electrodes. The null zones of E_x and H_y, which gives their radiation a double-lobed appearance, start from the electrode location at $x = L/2$, and the strongest signals for E_x and H_y are at the azimuth of 45° and also start from $x = L/2$. The null zones of E_x and H_y along the y-axis get wider as the length of an FLHED source is increased.

In summary, horizontal electric dipole, magnetic dipole and finite-length horizontal electric dipole sources generate EM fields that can be related to each other by impedance as with MT. This similarity allows one to use the MT method to interpret CSAMT data. But fields from these finite sources also depend on the positions of

the source and receiver. In the transition and near-field zones, apparent resistivity and phase are not same as those from MT. The source effect can invalidate an MT interpretation of data collected in the transition and near-field zones. The null zone is different for each mode and each dipole type. One has to keep this complication in mind to avoid weak signal and low-quality data when one uses CSAMT to resolve a geological target. When the length of a line source exceeds three skin depths in the earth, it may be necessary to consider its finite length.

2.5 Numerical results for a two-dimensional model

The 2.5-D forward modeling method is convenient for computing responses of a model to various sources. In this section numerical results for a 2-dimensional conductivity model are presented.

2.5.1 Model and mesh

The 2-dimensional model (Fig.2.13, also see Fig.4.8 for more detail of the model) is based on two conductive dipping prism bodies (10 Ωm) in a homogeneous bedrock (100 Ωm) with a conductive overburden at the surface. The two conductive bodies are 1000 m apart. Each conductive body is 1000 m wide and high, and its top is 300 m below the surface. The conductive overburden consists of three layers with resistivities 30 Ωm, 60 Ωm, and 80 Ωm from shallow to deep, each with 100 m thick.

The goal of discretization design is to balance computational cost and the accuracy of the numerical solution. Grid information is listed below

Horizontal Node y (km) -100.0 -39.0 -19.0 -10.0 -5.0 -3.0 -2.0 -1.5 -1.3 -1.1 -0.9
-0.7 -0.5 -0.3 -0.2 -0.1 0.0 0.05 0.1 0.2 0.3 0.5 0.7 0.9 1.1 1.3 1.5 1.7 1.9 2.1 2.3
2.5 2.7 2.9 3.1 3.3 3.5 3.7 3.9 4.1 4.3 4.5 4.7 4.9 5.1 5.3 5.5 5.7 5.9 6.1 6.3 6.5 6.7
6.9 7.1 7.4 7.7 8.0 8.5 9.0 10.0 13.0 18.0 28.0 48.0 100.0

Vertical Node z (km) -100.0 -40.0 -15.0 -8.0 -3.0 -1.0 -0.3 -0.1 -0.05 -0.02 -0.01 -0.005 0.0 0.005 0.01 0.02 0.04 0.06 0.08 0.1 0.12 0.14 0.16 0.18 0.2 0.22 0.24 0.26 0.28 0.3 0.35 0.4 0.45 0.5 0.6 0.7 0.8 0.9 1.0 1.1 1.2 1.3 1.4 1.6 1.8 2.0 2.5 3.0 3.5 4.0 4.5 5.0 5.5 6.0 7.0 8.0 10.0 15.0 20.0 30.0 40.0 50.0

Measurement site y (km) 2.1 2.3 2.5 2.7 2.9 3.1 3.3 3.5 3.7 3.9 4.1 4.3 4.5 4.7 4.9 5.1 5.3 5.5 5.7 5.9 6.1 6.3 6.5 6.7 6.9 7.1

Frequency (Hz) 2048.0 1024.0 512.0 256.0 128.0 64.0 32.0 16.0 8.0 4.0 2.0 1.0

The transmitter is located at the origin. The horizontal nodes are spaced logarithmically to the left side of the transmitter since there are no receivers, but on the right side, the horizontal nodes are made uniform where there are receivers and increase logarithmically outside of the region with data. Vertical node spacing at the surface is made less than one tenth of the skin depth deduced from the lowest resistivity at the surface in order to have an accurate numerical differentiation. The mesh in the earth is $200km \times 50km$ with the grid of 50×50. 26 measurement sites are located from 2.1 km to 7.1 km with a spacing of 200 m. The 12 frequencies from 1 Hz to 2048 Hz are spaced logarithmically. Figure 2.14 shows the center part of the finite element mesh.

2.5.2 Configuration

Horizontal electric dipole, horizontal magnetic dipole and finite-length line sources will be considered. According to the relationship between the orientation of the source and the direction of the strike, four configurations can be set up (Figure 2.15): along-strike HED (denoted as HEDx), across-strike HED (HEDy), along-strike HMD (HMDx), and across-strike HMD (HMDy). The configuration of an FLHED source can be treated similarly as an HED. Separate TE and TM modes do not exist for a dipole source (as in MT or for a 2-D infinite source). However, TE and TM can

formally be defined in analogy to MT with the TE mode: $(E_x,\ H_y)$ and the TM mode: $(E_y,\ H_x)$.

Since the EM fields of 2-D model due to a dipole source are 3-dimensional, various measurement profiles can be deployed. Figure 2.16 shows two basic geometries: co-linear profile (or called, main profile) and broadside profile (or non-main profile). The non-main profile in Figure 2.16 has an offset d in the strike direction.

2.5.3 Numerical results

HEDx data

Figure 2.17 shows apparent resistivities and phases for HEDx; TE data on the main profile (Fig.2.17a) and a non-main profile with offset 3.0 km (Fig.2.17b), and TM data on the non-main profile (Fig.2.17c). Because of the null zone on the main profile for E_y and H_x, measurements for TM data on the main profile are not recommended. All responses show that the high apparent resistivity and low phase associated with the HED source effect occur at the sites close to the dipole and at low frequencies. From Fig.2.17 a and b, note that the source effect does not decrease very much for a 3.0 km offset and that the data from the non-main profile are complicated by the 35° null zone of E_x and H_y, especially for phase. TM data show two separated resistivity anomalies, while TE data hardly indicate if one or two conductors are present. The conductive body at the right, which is farther away from the source, has a stronger anomaly.

HEDy data

Figure 2.18 a, b, and c displays HEDy TE data on the non-main profile and HEDy TM data on the main profile and the non-main profile. TE data on the main profile are not shown because of the null zone. The source effect, the separation of the anomalies, and the strength of the anomalies seen for HEDx can also be observed for

HEDy. The TM data from the non-main profile are much more complicated by the null zone than their counterpart for HEDx (Fig.2.18.b). This is because TE data for HEDx are observed in the lower triangular regions of Fig.2.4c and d, while TM data of HEDy is collected in the upper triangular regions. Fig.2.4c and d show that the 35° null zone has more effect on the upper triangular regions than on the lower ones, and the lower triangular regions are larger than the upper ones. TE data (Fig.2.17b and Fig.2.18a) or TM data (Fig.2.17c and Fig.2.18c) from the non-main profile for HEDx and and HEDy are very different. Therefore, TE data (or TM data) for HEDx and HEDy should be considered separately. Zonge and Hughes (1988) proposed that " *In tensor measurements, these quantities* $(E_x, E_y, H_x, H_y, H_z)$ *may be treated by standard MT processing techniques*". This claim is true only if measurements are made in the far-field. In practice, measurements of E_x, E_y, H_x, H_y, and H_z should be made separately for HEDx and HEDy of tensor CSAMT.

HMDx data

TE data for the non-main profile and TM data for the main and non-main profiles are shown in Fig.2.19 a, b, c. Physically, HMDx is somewhat similar to HEDy. The data of HEDy and HMDx show this similarity. Compare Fig.2.18a with Fig.2.19a and Fig.2.18b with Fig.2.19b. Thus the general features for the HEDy are also true for the HMDx. But the source effect for an HMD appears as low apparent resistivity and high phase at the sites near to the source and at low frequencies. HMDx data appears to have weaker resistivity anomalies, but shows less source effect than HEDy data.

HMDy data

HMDy data are shown in Fig.2.20 and are similar to HEDx data. The features of HMD data that are different from HED data discussed above are also true for HMDy data. Thus, HMDy's main features can be summarized as: resistivity anomalies in

the TM data are separate, but not in the TE data; the conductive body at the right has stronger anomalies; HMDy data has weaker conductive anomalies, but with less source effect than HEDx data; etc. Note that TE phase appears low at low frequencies and at the sites very close to the source.

FLHEDx and FLHEDy data

Figure 2.21 shows apparent resistivities and phases for an x-directed FLHED source with a length of 2.5 km, which is about 4 skin depths of bedrock or 7 skin depths of the shallow layer. The HEDx results (Fig.2.17) are very similar to the FL-HEDx. The significant difference is the source effect. For the main profile, the source effect is less as the length of the FLHED source is increased.

The results for a y-directed FLHED source are shown in Figure 2.22. It has very similar results to those from HEDy. Because the electrodes are separated from each other as the length of the FLHEDy increases in the y-direction, the measurement sites become closer to one electrode. The source effect on main profile is therefore larger. But for a site which has the same distance from the electrode, the source effect should be smaller for an FLHED source.
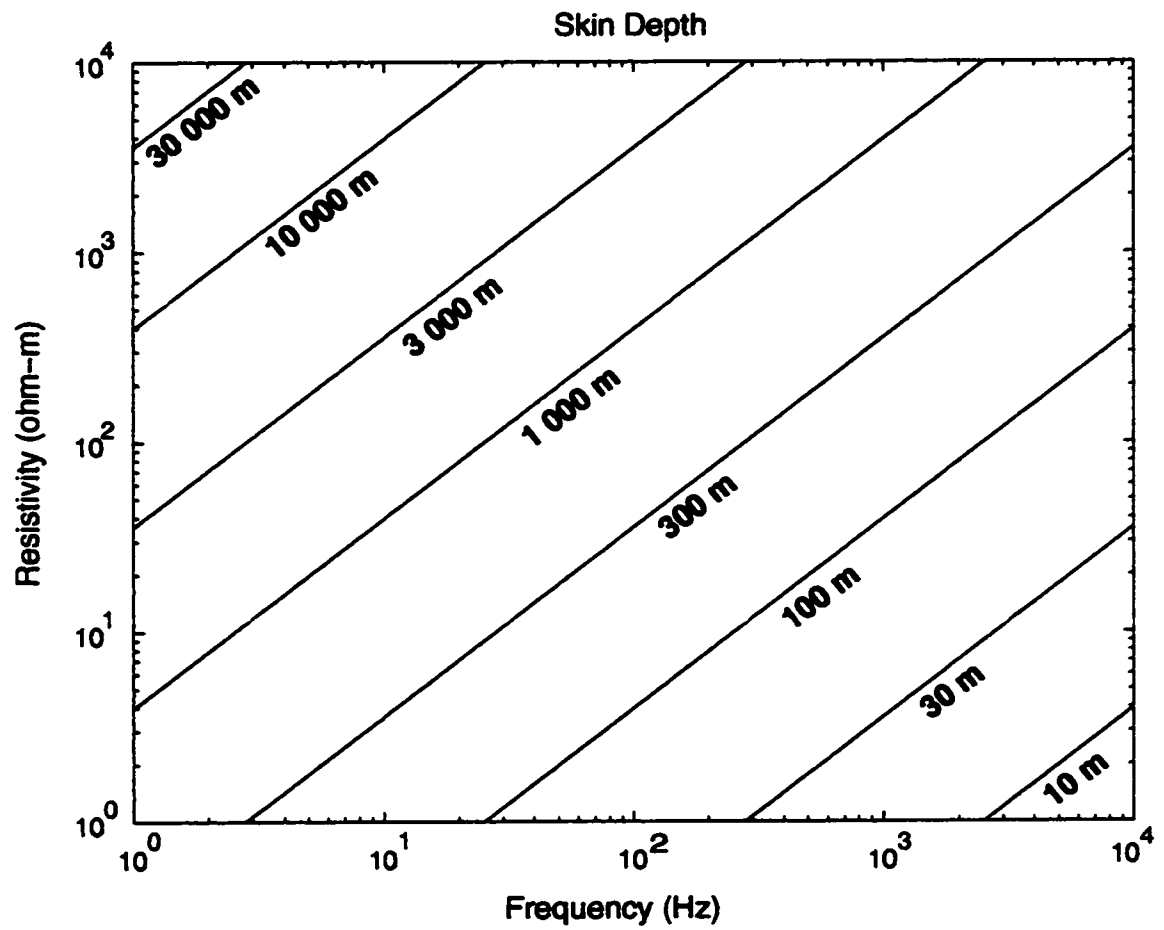
Figure 2.1: Skin depth as a function of resistivity and frequency for a half space.
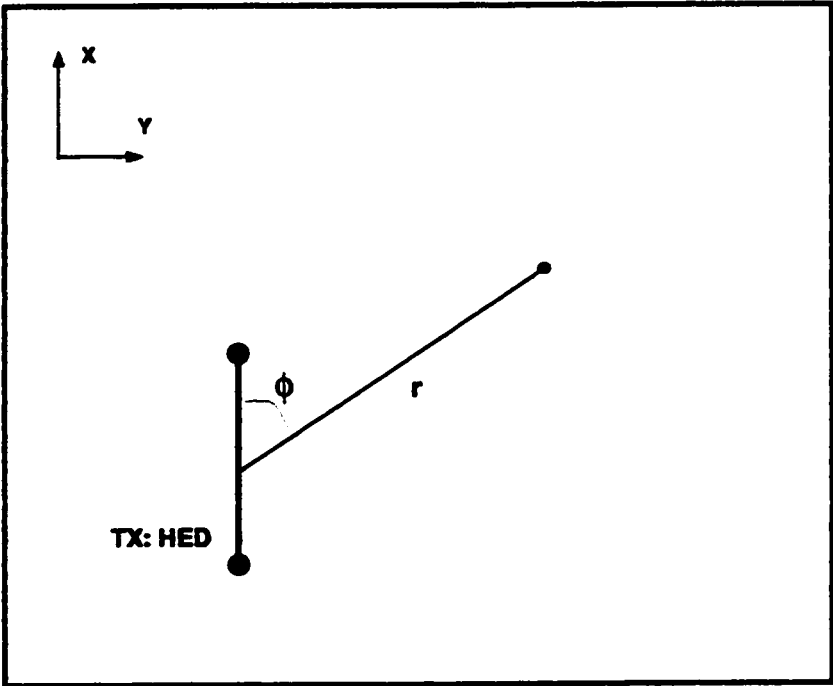
Figure 2.2: Transmitter and receiver geometry.
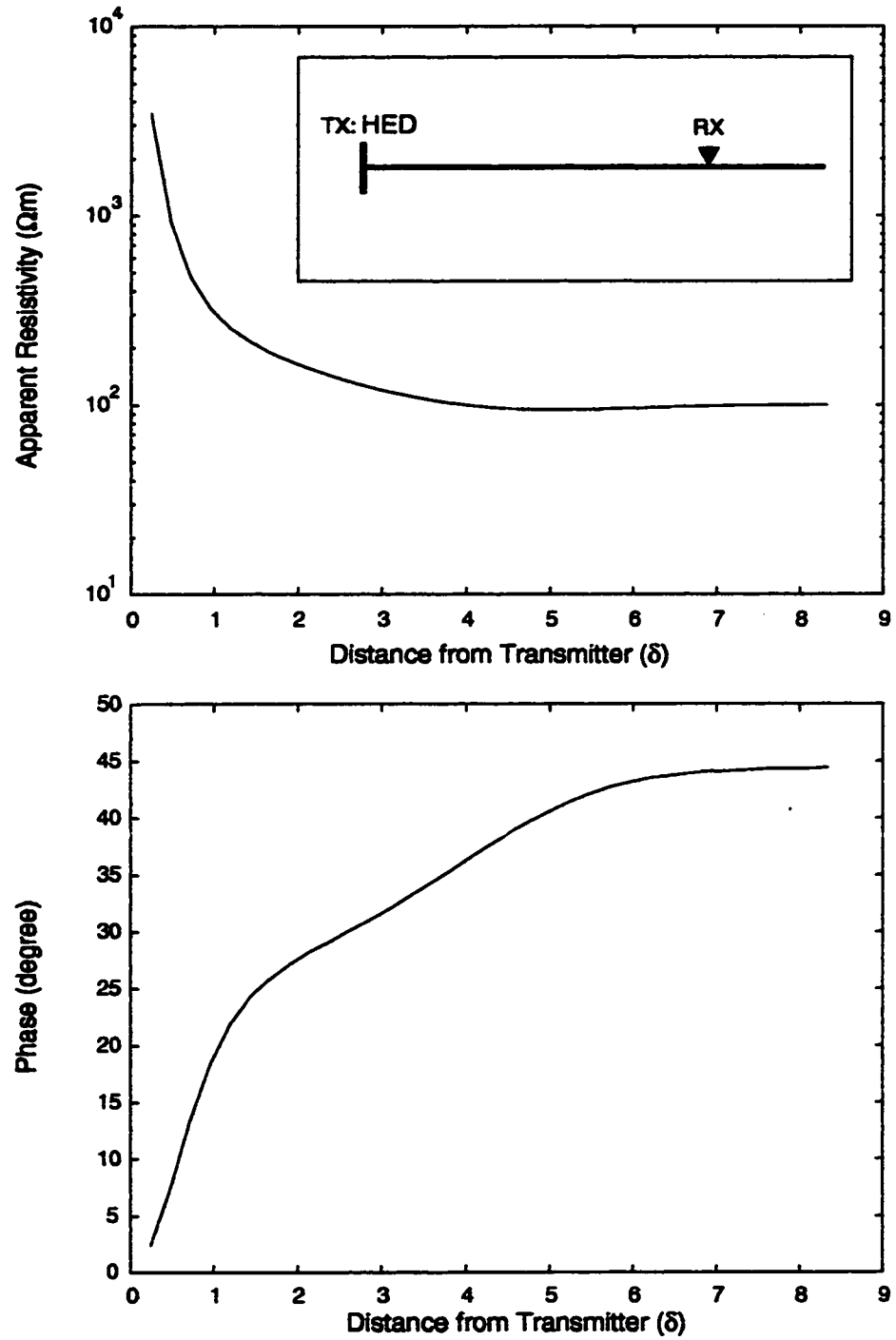
Figure 2.3: Apparent resistivity and phase for an HED on a 100 Ωm half-space. f = 64 Hz.
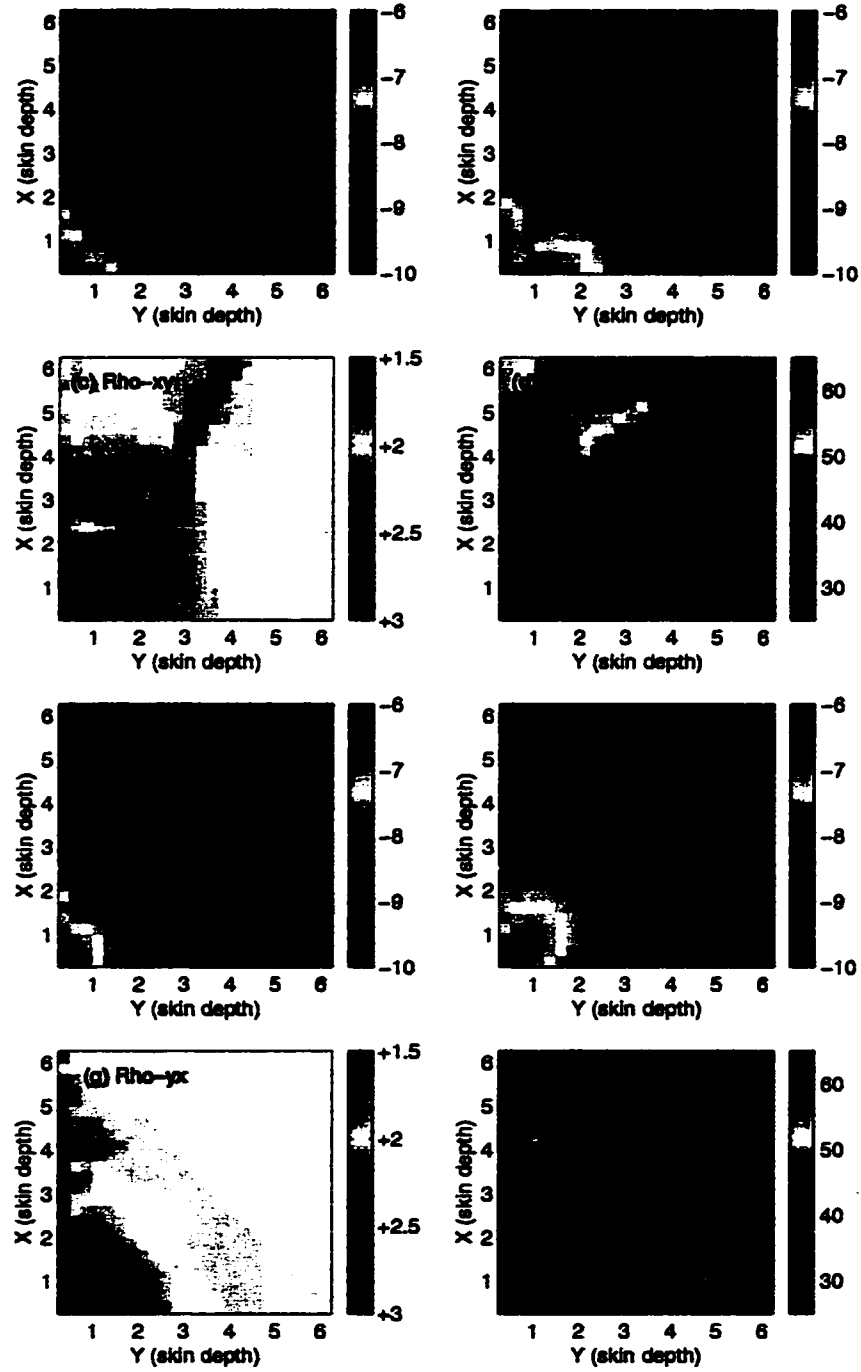
Figure 2.4: EM fields, apparent resistivities and phases of an x-directed HED at the origin over a 100 Ωm half space. E $(Volt/m)$, H $(Ampere/m)$, apparent resistivity (Ωm) all have a $\log_{10}$ scale, phase (degrees) has a linear scale.
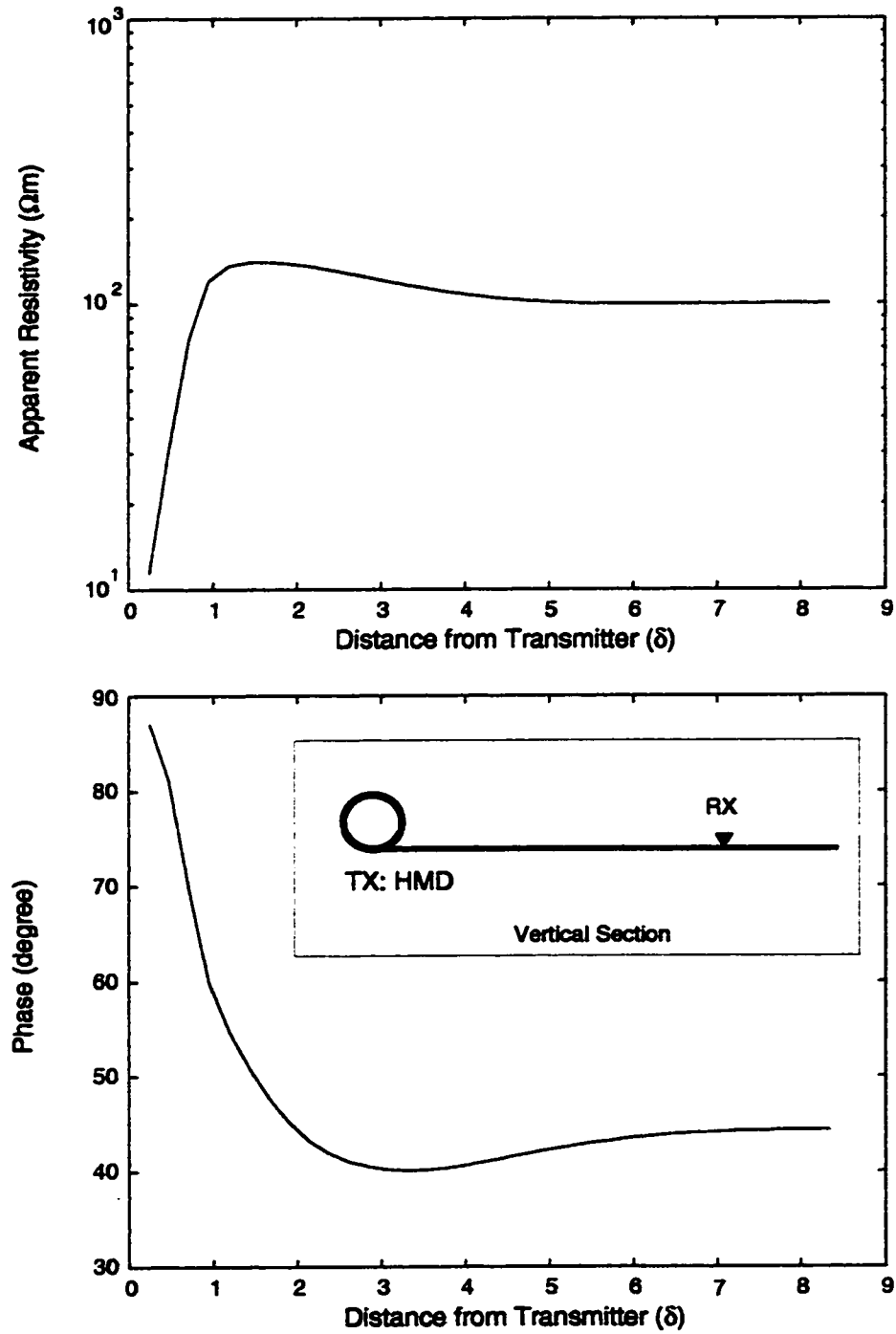
Figure 2.5: Apparent resistivity and phase for an HMD on a 100 Ωm half-space. f = 64 Hz.
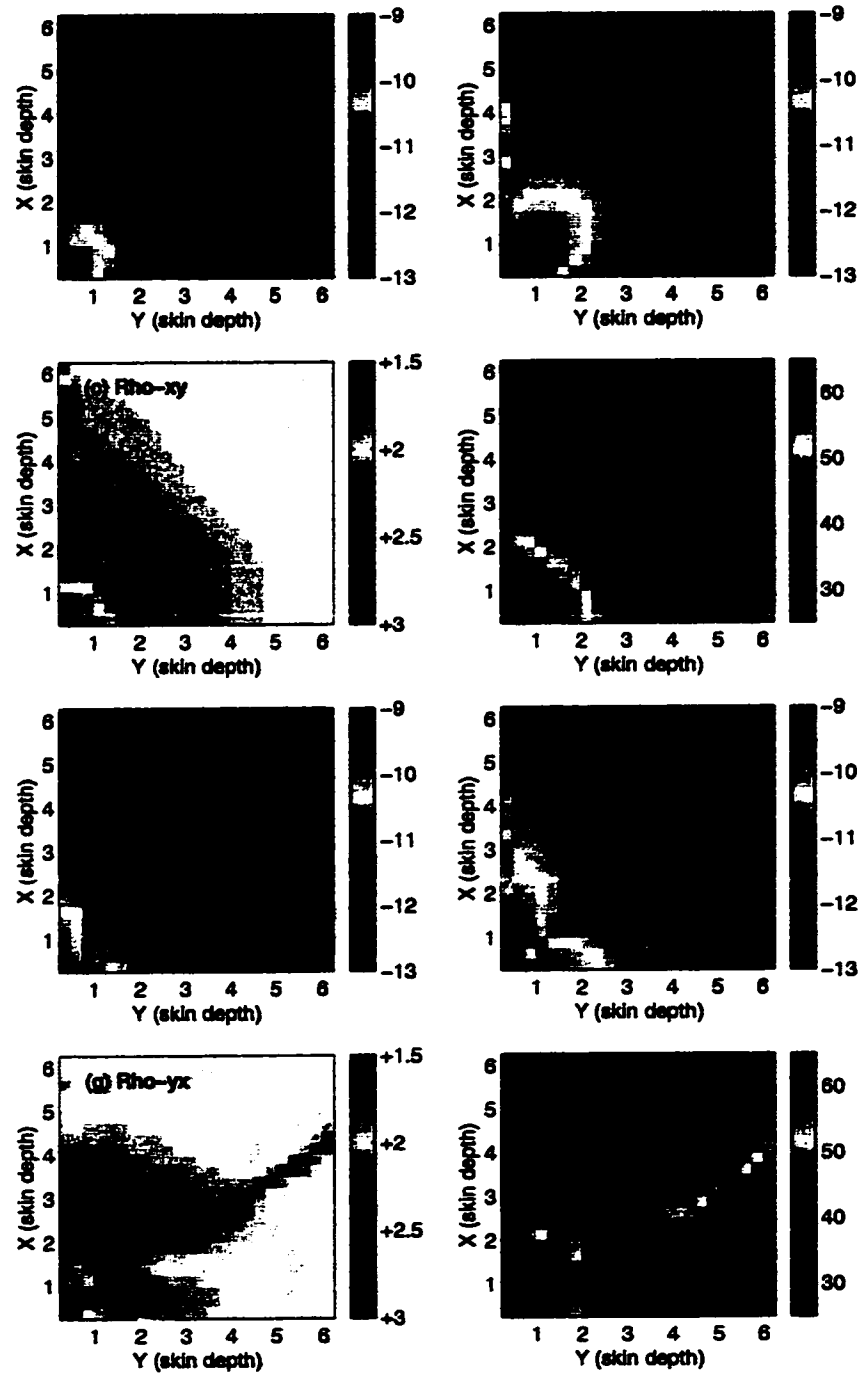
Figure 2.6: EM fields, apparent resistivities and phases of an x-directed HMD at the origin over a 100 Ωm half-space. E $(volt/m)$, H $(ampere/m)$, apparent resistivity (Ωm) all have a $\log_{10}$ scale, phase (degree) has a linear scale.
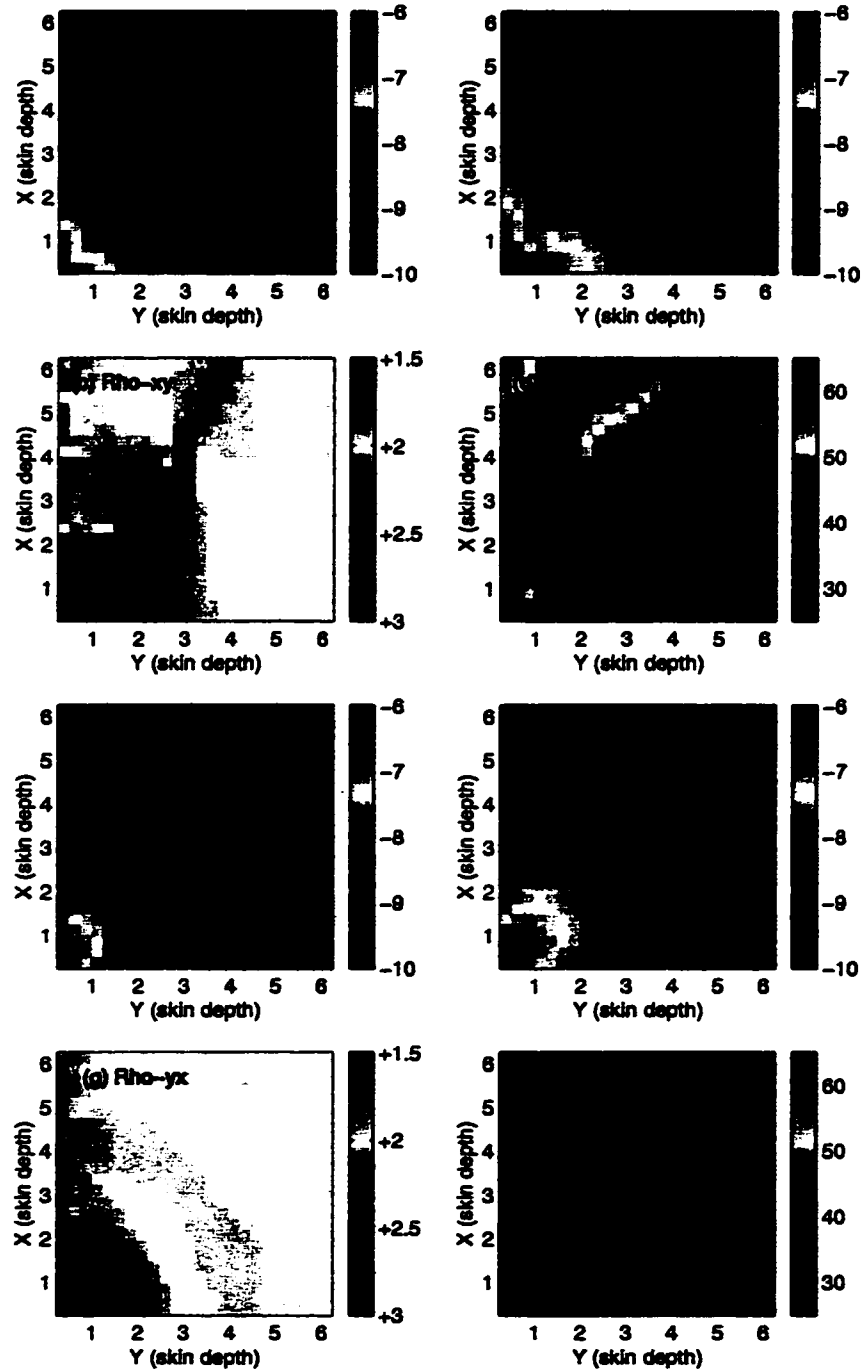
Figure 2.7: EM fields, apparent resistivities and phases of an x-directed FLHED with a length of 1 skin depth, centered at the origin on a 100 Ωm half-space. E ($volt/m$), H ($ampere/m$), apparent resistivity (Ωm) all have a $\log_{10}$ scale, phase (degree) has a linear scale.
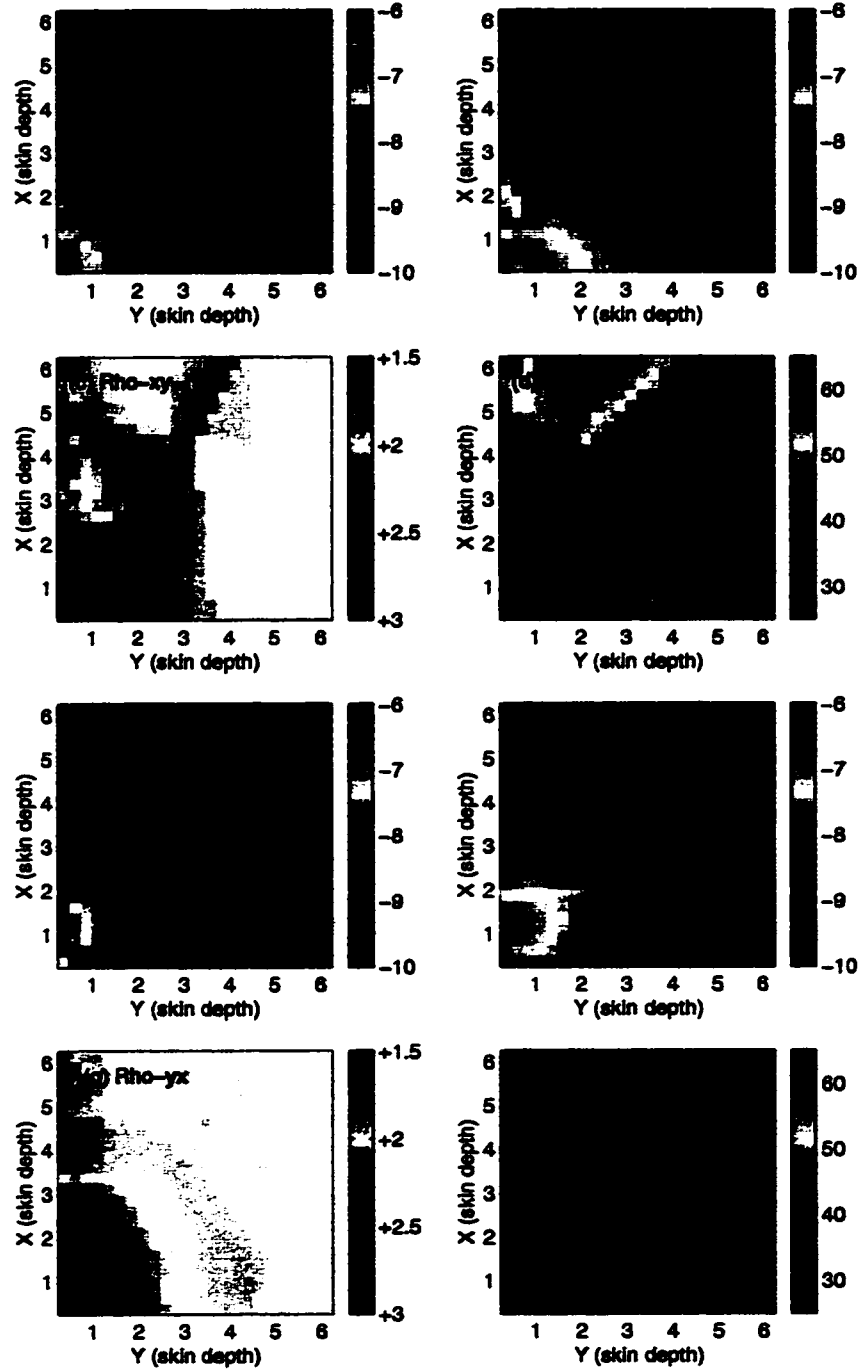
Figure 2.8: EM fields, apparent resistivities and phases of an x-directed FLHED with a length of 2 skin depths, centered at the origin on a 100 Ωm half-space. E ($volt/m$), H ($ampere/m$), apparent resistivity (Ωm) all have a $\log_{10}$ scale, phase (degree) has a linear scale.
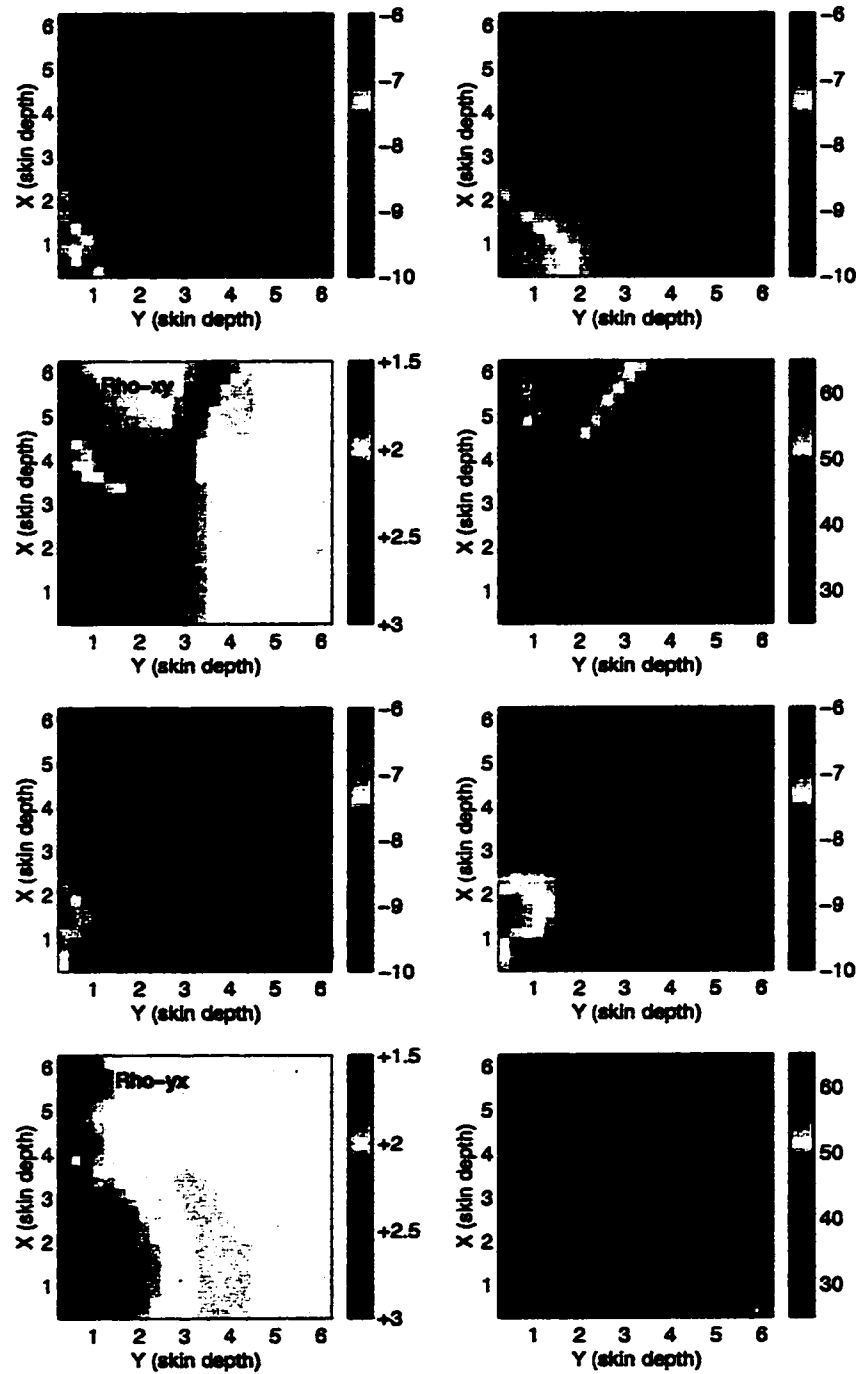
Figure 2.9: EM fields, apparent resistivities and phases of an x-directed FLHED with a length of 3 skin depths, centered at the origin. E ($volt/m$), H ($ampere/m$), apparent resistivity (Ωm) all have a $\log_{10}$ scale, phase (degree) has a linear scale.
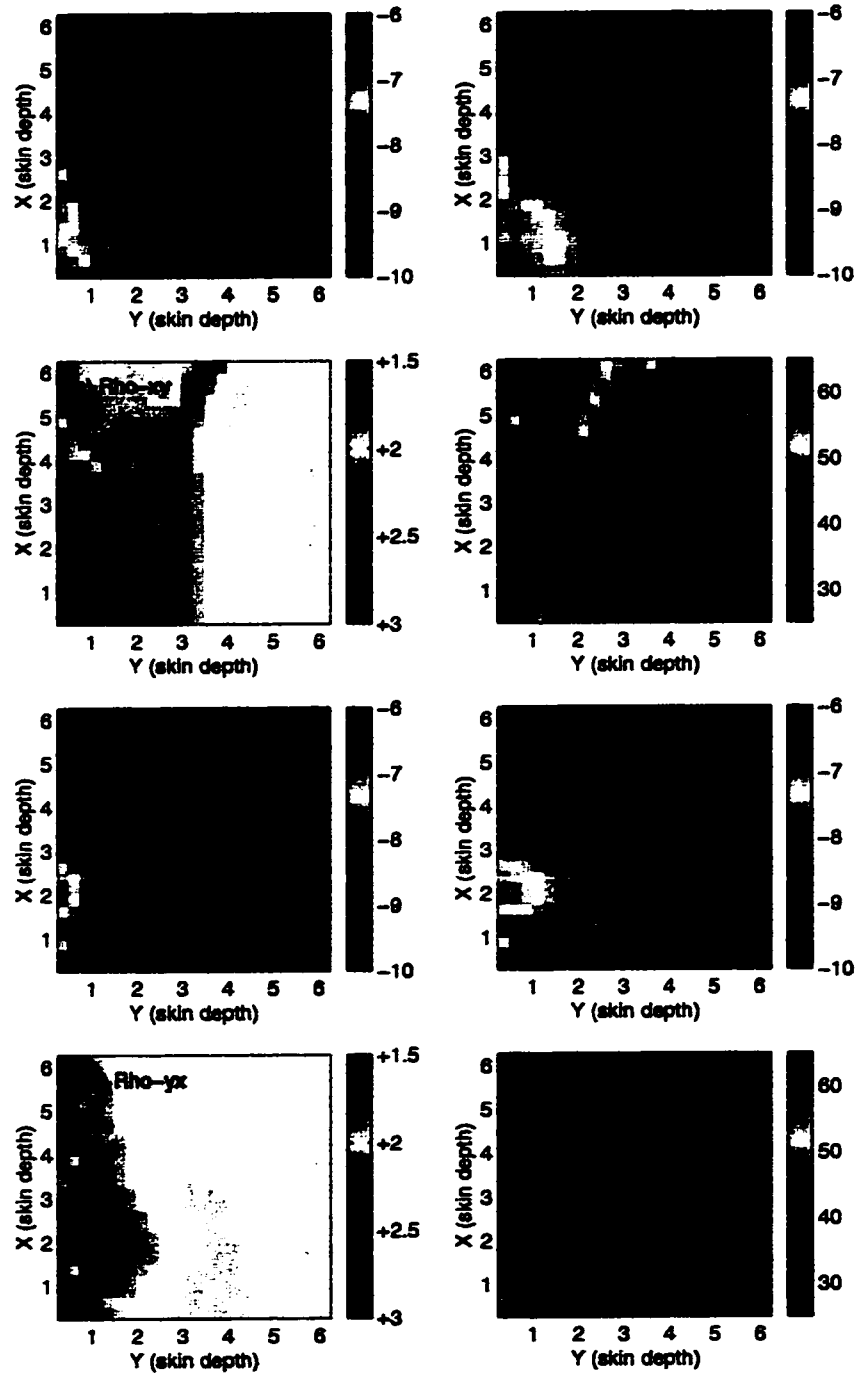
Figure 2.10: EM fields, apparent resistivities and phases of an x-directed FLHED with a length of 4 skin depths, centered at the origin. E ($volt/m$), H ($ampere/m$), apparent resistivity (Ωm) all have a $\log_{10}$ scale, phase (degree) has a linear scale.
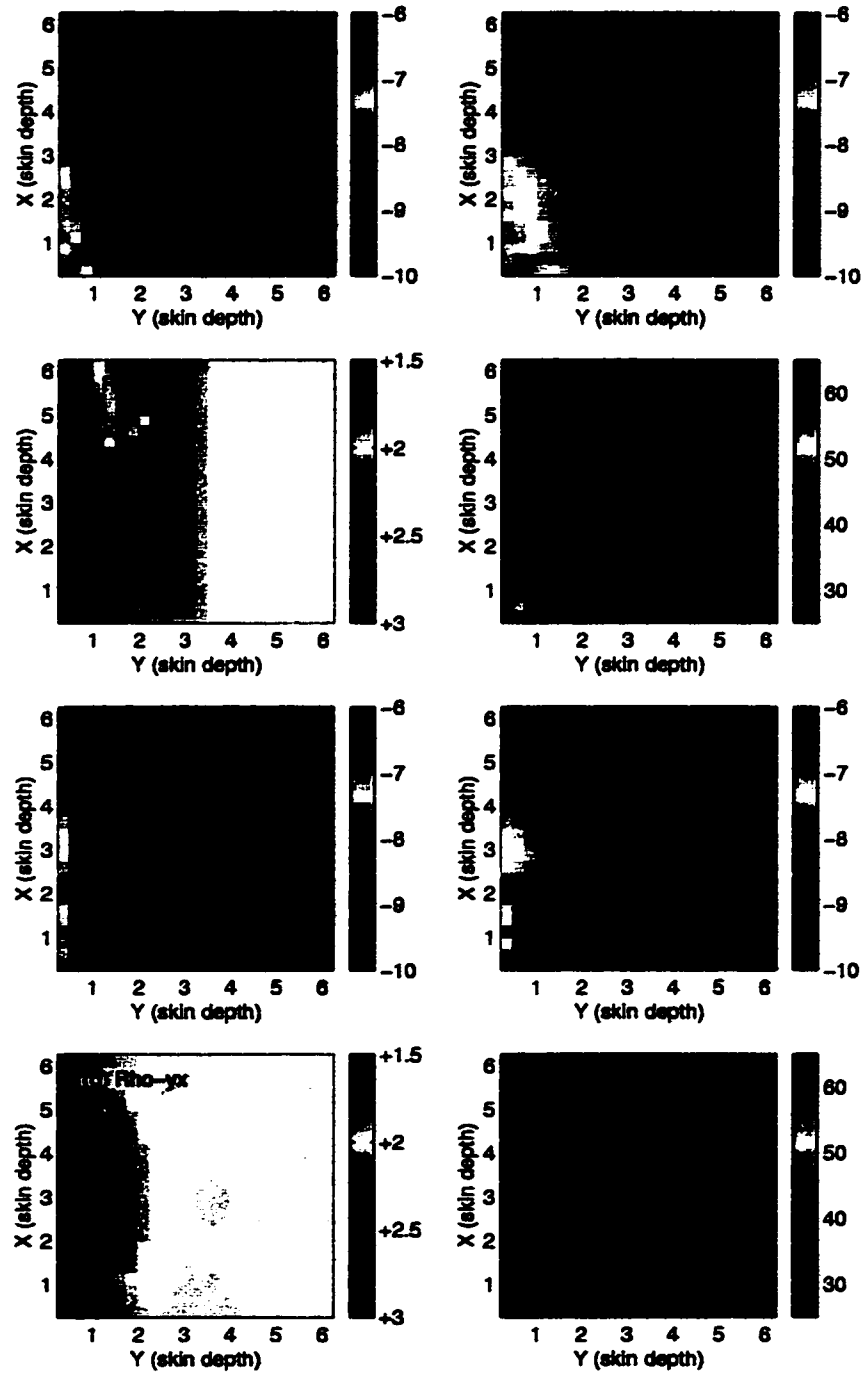
Figure 2.11: EM fields, apparent resistivities and phases of an x-directed FLHED with a length of 6 skin depths, centered at the origin. E $(volt/m)$, H $(ampere/m)$, apparent resistivity (Ωm) all have a $\log_{10}$ scale, phase (degree) has a linear scale.
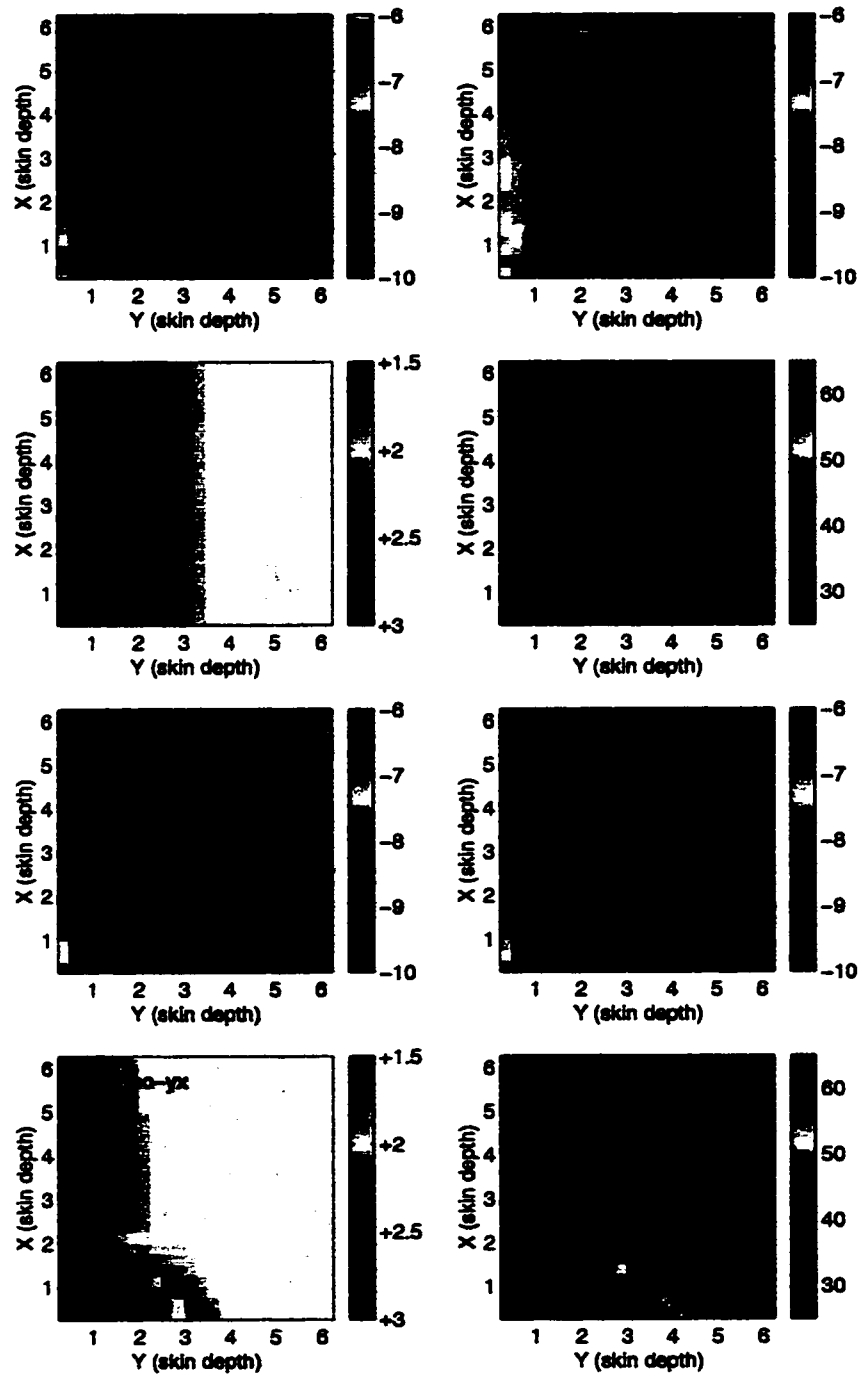
Figure 2.12: EM fields, apparent resistivities and phases of an x-directed FLHED with a length of 10 skin depths, centered at the origin. E ($volt/m$), H ($ampere/m$), apparent resistivity (Ωm) all have a $\log_{10}$ scale, phase (degree) has a linear scale.
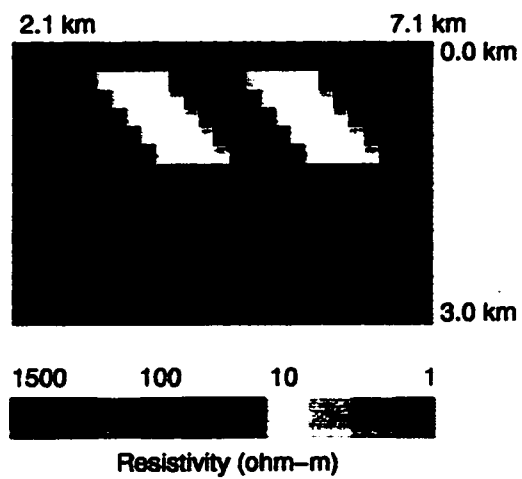
Figure 2.13: 2-Dimensional model. Two conductive dipping prisms (10 Ωm) embedded in a homogeneous bedrock (100 Ωm), with a conductive overburden. Horizontal ticks are measurement sites. The transmitter is located at the origin of 0 *km*.
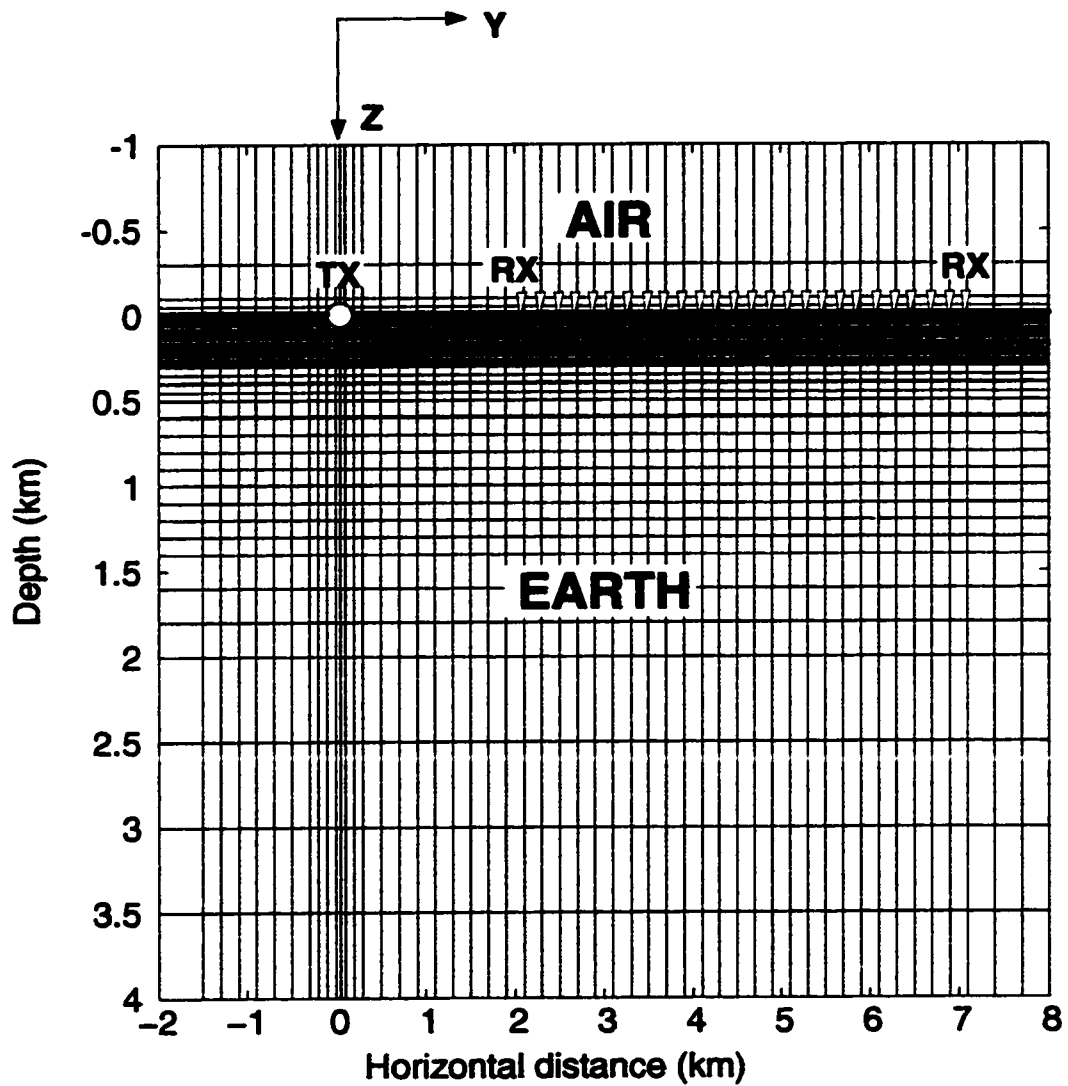
Figure 2.14: The center of the finite element mesh used for modeling. The transmitter is located at the origin. Vertical exaggeration is 2. The overall mesh is 200 $km \times$ 150 km with a grid 66 $\times$ 62 of nodes. The mesh in the earth is 200 $km \times$ 50 km with a grid 66 $\times$ 50.
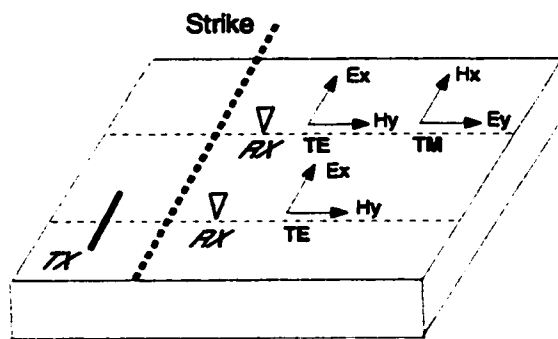
a) HEDx: Along-Strike HED
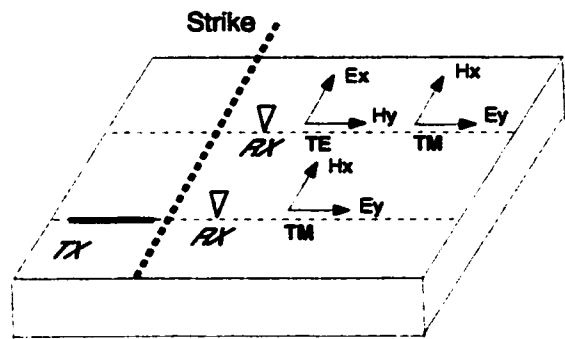
b) HEDy: Across-Strike HED
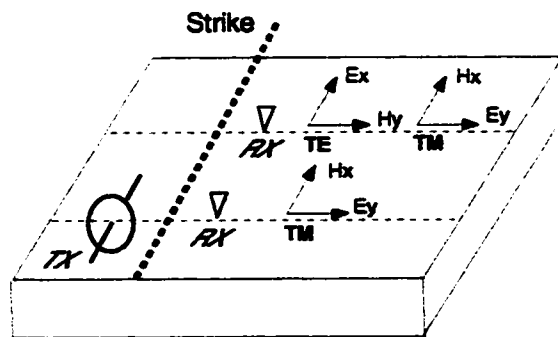
c) HMDx: Along-Strike HMD
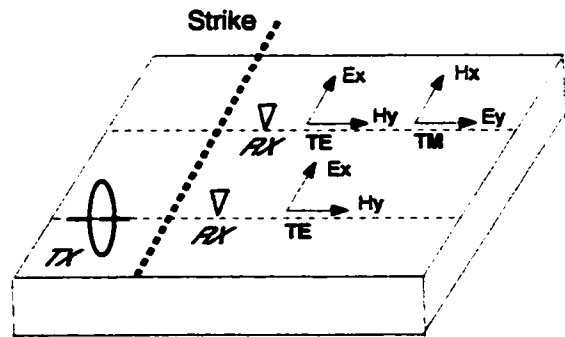
d) HMDy: Across-Strike HMD

Figure 2.15: CSAMT Configurations.
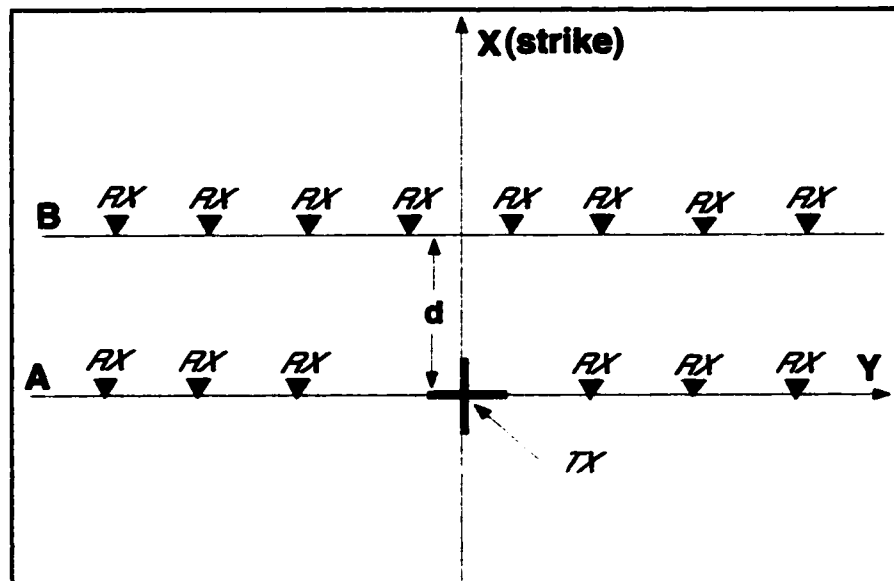
Figure 2.16: Geometry of a CSAMT survey. Profile A is called the main profile (or, the co-linear profile), profile B the non-main profile (broadside profile) with offset d.
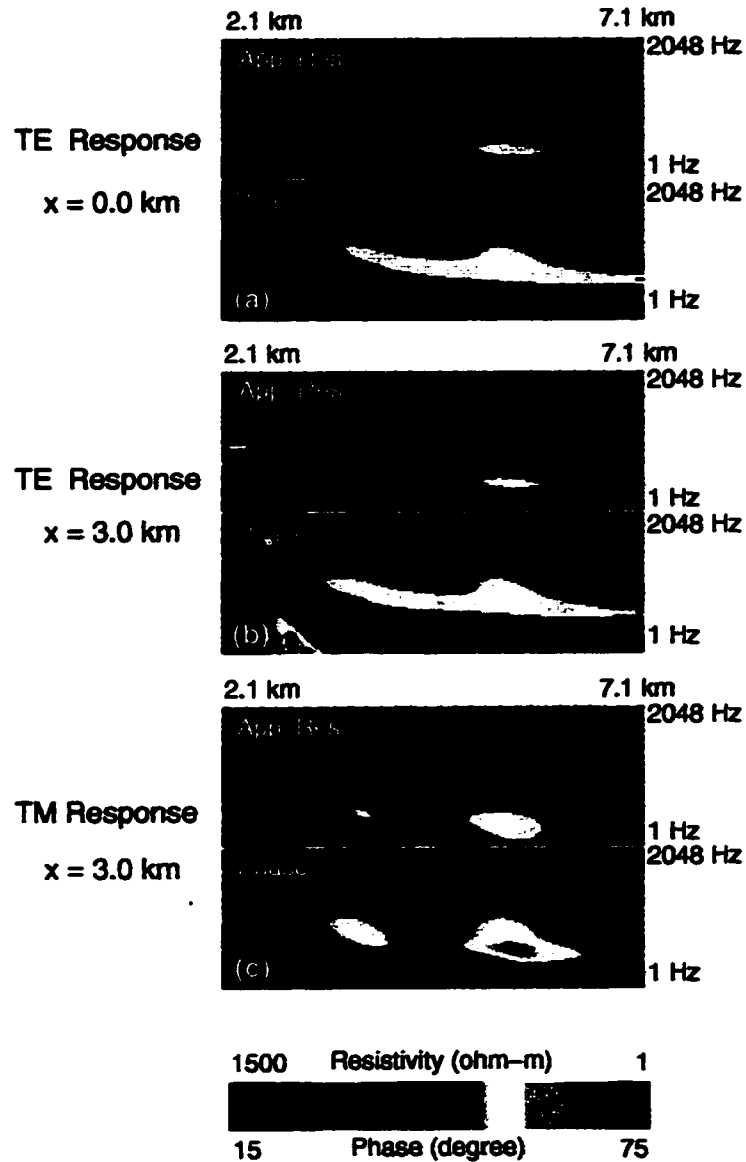
Figure 2.17: HEDx apparent resistivities and phases on the main profile (offset $x = 0.0$ km) and a non-main profile with offset $x = 3.0$ km for the two conductive dipping prism model. Data are represented in pseudo-section format: horizontal ticks are the measurement sites with the distances from the HEDx located at the origin; vertical ticks represent frequencies. (hereafter, I will omit the explanation of the pseudo-section format if data are represented in this format.) (a) TE ρ_a and ϕ on the main profile. (b) TE ρ_a and ϕ on the non-main profile. (c) TM ρ_a and ϕ on the non-main profile.
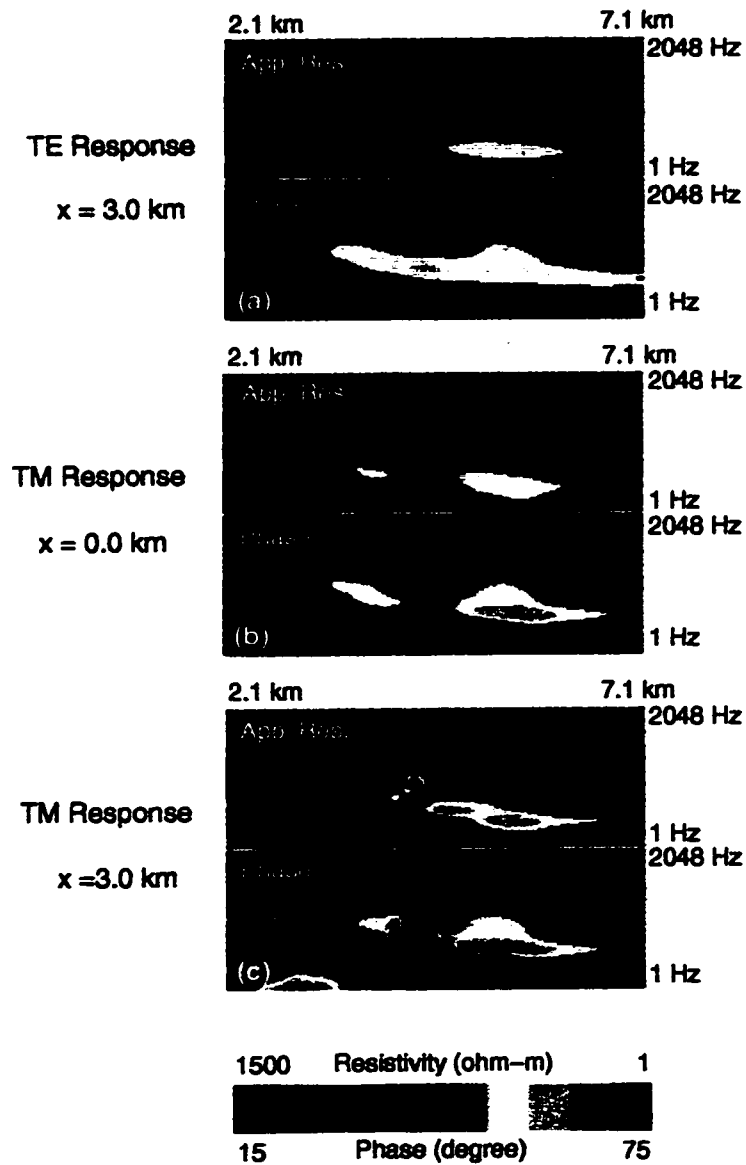
Figure 2.18: HEDy apparent resistivities and phases on the main profile (offset $x =$ 0.0 km) and a non-main profile with offset $x = 3.0$ km for the two conductive dipping prism model. (a) TE ρ_a and ϕ on the non-main profile. (b) TM ρ_a and ϕ on the main profile. (c) TM ρ_a and ϕ on the non-main profile.
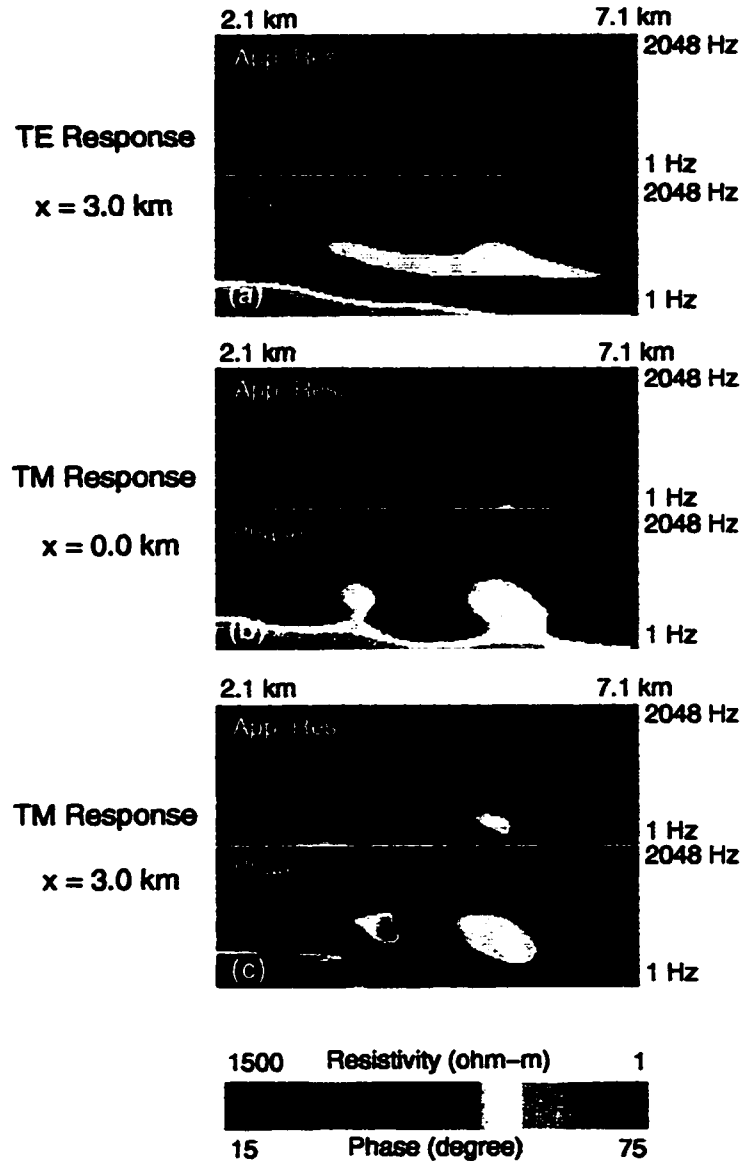
Figure 2.19: HMDx apparent resistivities and phases on the main profile (offset $x = 0.0$ km) and a non-main profile with offset $x = 3.0$ km for the two conductive dipping prism model. (a) TE ρ_a and ϕ on the non-main profile. (b) TM ρ_a and ϕ on the main profile. (c) TM ρ_a and ϕ on the non-main profile.
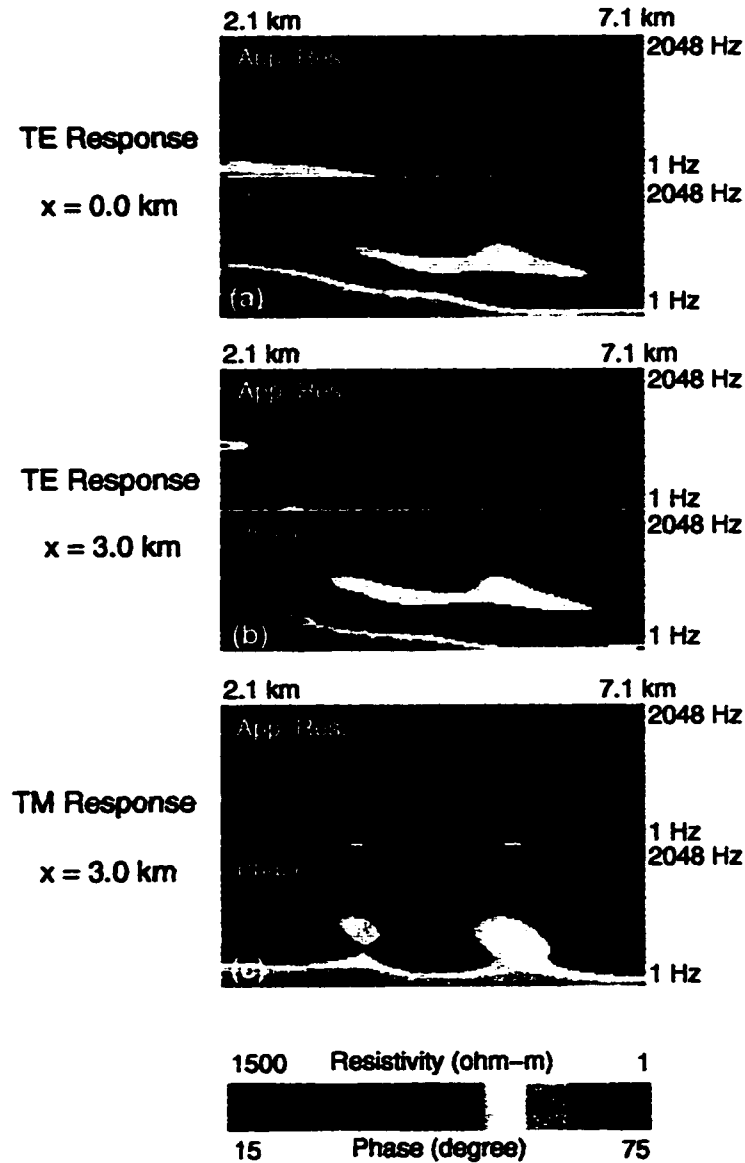
Figure 2.20: HMDy apparent resistivities and phases on the main profile (offset $x =$ 0.0 km) and a non-main profile with offset $x = 3.0$ km for the two conductive dipping prism model. (a) TE ρ_a and ϕ on the main profile. (b) TE ρ_a and ϕ on the non-main profile. (c) TM ρ_a and ϕ on the non-main profile.
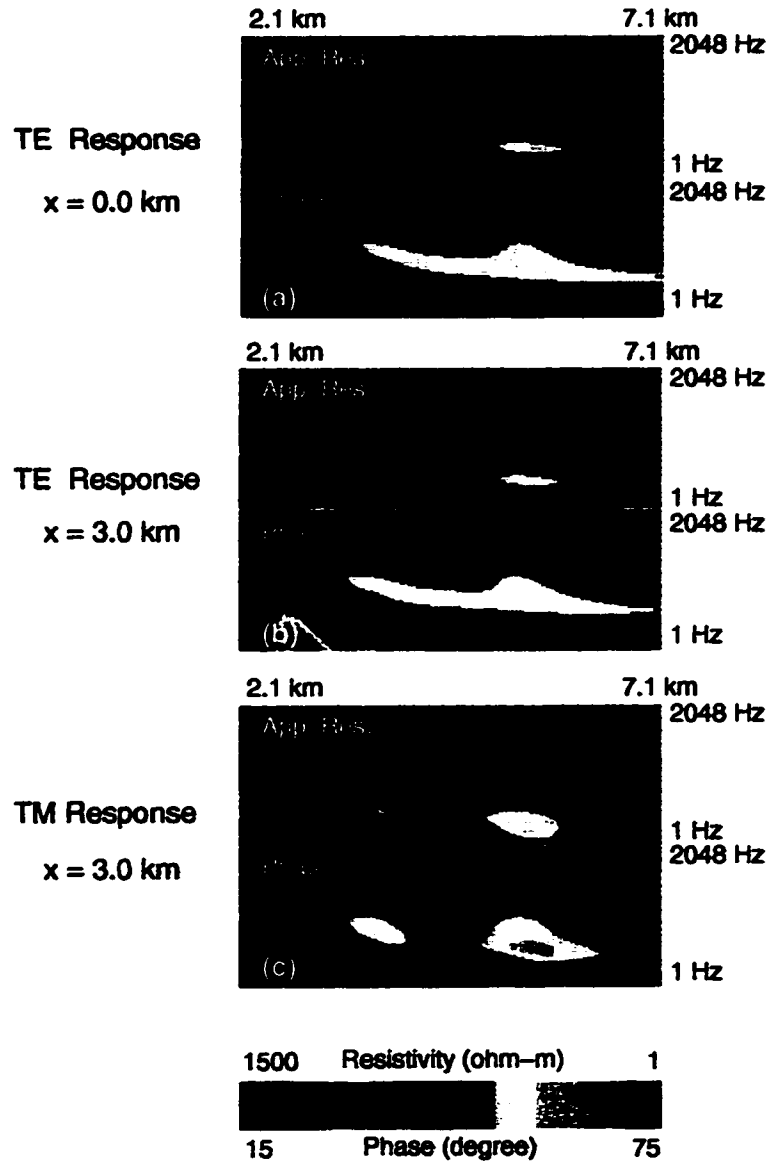
Figure 2.21: FLHEDx apparent resistivities and phases on the main profile (offset $x = 0.0$ km) and a non-main profile with offset $x = 3.0$ km for the two conductive dipping prism model. (a) TE ρ_a and ϕ on the main profile. (b) TE ρ_a and ϕ on the non-main profile. (c) TM ρ_a and ϕ on the non-main profile.
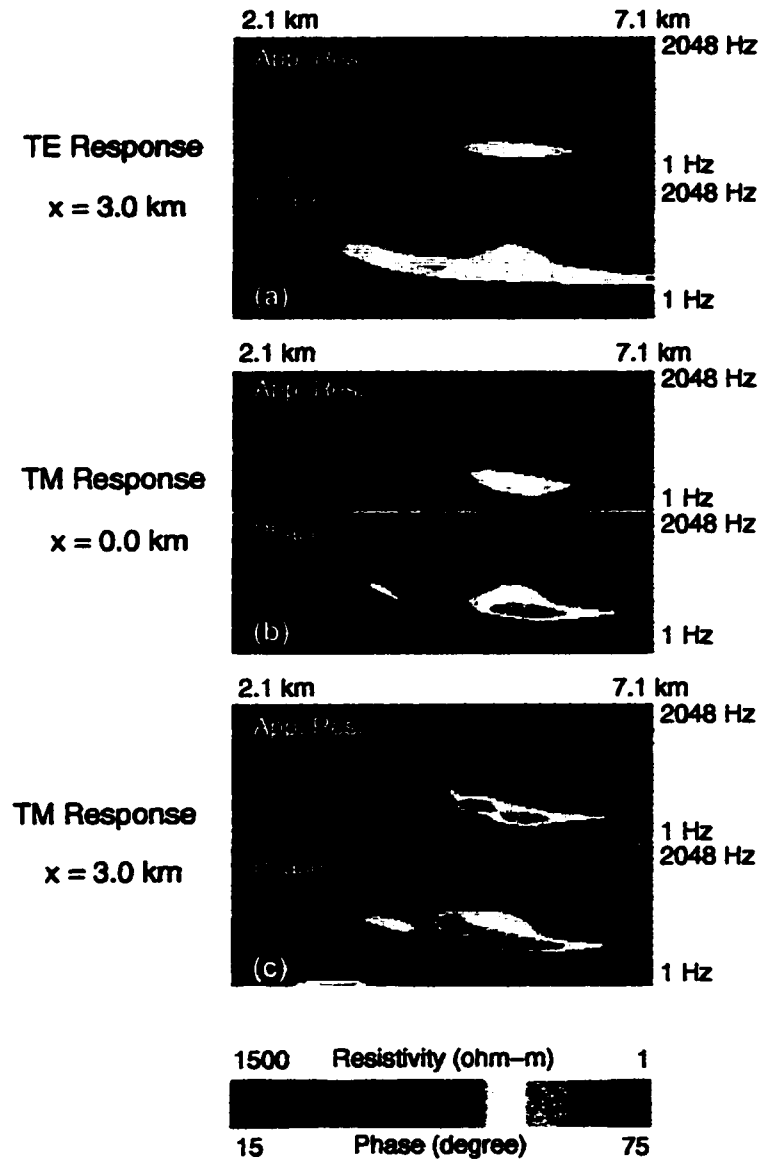
Figure 2.22: FLHEDy apparent resistivities and phases on the main profile (offset $x = 0.0$ km) and a non-main profile with offset $x = 3.0$ km for the two conductive dipping prism model. (a) TE ρ_a and ϕ on the non-main profile. (b) TM ρ_a and ϕ on the main profile. (c) TM ρ_a and ϕ on the non-main profile.

Chapter 3

INVERSION

In this chapter I will discuss inversion. In the first two sections, a formulation of an inversion is given and some general inversion difficulties such as nonlinearity and nonuniqueness are discussed. In the third section, I will focus on the 2-D inversion. This includes a formulation of the 2-D inverse algorithm and its numerical representation. After this, a short review of the Rapid Relaxation Inversion (RRI) method of Smith and Booker (1991) is given. Then I describe previous methods to invert CSAMT data. Finally, I present a new CSAMT data inversion algorithm: the CSAMT-RRI inversion algorithm. The CSAMT-RRI algorithm is developed by extending the RRI method to CSAMT inversion.

3.1 Inverse problems

The inverse problem is a process to recover the earth's resistivity structure from the measurements. The forward problem discussed in last chapter can be written symbolically as

$$d = F(m) \tag{3.1}$$

where **m** is a model of the earth's resistivity, **d** is the result of the forward problem, and **F** is the physics of the problem, which is known and provides a means to compute **d** for any model **m**. Then the inverse problem corresponding to this forward problem would be to find the set of all **m** that yield the given data **d**. It may be written, also symbolically, as

$$m = F^{-1}(d) \tag{3.2}$$

This inverse mapping F^{-1} can be very complicated and non-unique.

3.2 General inversion problems

When the inversion problem is formulated as in (3.2), no specific property is assigned to the functional F, the model m or the measurements d. The property of each element plays an important role in inversion. In this section, I will review the general inversion problem.

The functional F can be simple or complicated. The simplest functionals are the linear ones. When the functional F is linear, the corresponding inverse problem is said to be linear. Linear inverse problems are the simplest and best-understood inverse problems. They have been extensively studied by Backus and Gilbert (1968) and Backus (1970a, b, c). They showed that although an infinite number of models exist, localized averages of those models can be uniquely determined, and the position that the averages are localized about may be varied continuously, yielding models whose resolution properties are well understood. Franklin (1970), and Jordan and Franklin (1971) studied a more specific linear case by assigning values to m with error bars at all positions to realize a stochastic process.

Most functionals which are derived in geophysics are nonlinear, so the corresponding inverse problems are nonlinear. Well-established linear inverse theories cannot be directly applied. Non-linear inverse problems have been approached in two ways: the direct non-linear inversion and the linearized inversion. The direct non-linear inversion has only been considered for simple, low-dimensional situations. For example, Weidelt (1972), Parker (1980), Parker and Whaler (1981), Whittal and Oldenburg (1986) etc. have discussed direct non-linear inversion methods for 1-D MT data. A direct non-linear inversion method for multi-dimensional models is unknown.

Another approach to the non-linear inverse problem is the linearized inversion. The nonlinear relationship between data and model is approximated by the following

linear relationship

$$d_i = \mathbf{F(m_0)} + \sum_{j=1}^{M} G_{ij}\delta m_j \tag{3.3}$$

or in continuous form,

$$d_i = \mathbf{F(m_0)} + \int g_i(\mathbf{r})\delta m(\mathbf{r})d\mathbf{r} \tag{3.4}$$

where δm is a small change to a known (or guessed) model $\mathbf{m_0}$. G_{ij} and $g_i(\mathbf{r})$ are known as the Fréchet derivatives, sensitivities or data kernels. Linearized inversion methods iterate using a linear inversion of the residuals $r_i = d_i - \mathbf{F(m_0)}$ for a current model. This is essentially the Gaussian-Newton iterative procedure. A typical linearized inversion proceeds as follow: Starting with an initial model, one calculates Fréchet derivatives (sensitivities of the data with respect to the model parameters) and data residuals; then a linear inversion is applied to compute the perturbated model from the data residuals. The model can be updated by adding the perturbation to the initial model. This updated model is used to compute the predicted responses and the new residuals for next iteration. This procedure is repeated until convergence is achieved. In relative terms, linearized inversions are easy to implement, flexible to extend to higher dimensional model, and are able to incorporate model structural constraints.

In reality, the unknown model $\mathbf{m}$ is a function of position, which is of infinite dimension, and the measurements $\mathbf{d}$ comprise only a finite collection of numbers, either exactly or with error, so that the inverse problem is not unique. Non-uniqueness is another serious problem in inversion. Four approaches have been suggested to deal with the non-uniqueness problem. One approach (Backus and Gilbert, 1968; Parker, 1970; Oldenburg, 1979) has been to find localized averages that are shared by all models that are close enough to some reference model for a linearization approximation to hold. A second approach (Tikhonov, 1970; Parker, 1975; Oldenburg, 1983; Constable et al, 1987; Smith and Booker, 1988) has been to find models minimizing some functional, particularly functionals which penalize roughness of the model. A third

approach has been to assume prior knowledge of the distribution of likely models and find which of these models is most likely given a set of data (Franklin, 1970; Jordan and Franklin, 1970; Backus, 1970c, 1988). A fourth approach has been to ignore the problems of the non-uniqueness and to merely seek a model fitting the data fairly well. The first three approaches differ in interpretation of the resultant models, but not in obtaining models. An inversion algorithm which makes the model unique by minimizing a norm of the derivative of the model is given in next section.

3.3 . A formulation of the 2-D inversion

The goal of CSAMT/MT inversion could be to find an electrical resistivity model that fits the data. Mathematically, this can be stated as

$$\text{minimize} \quad obj = \mathbf{e}^T \mathbf{e} \tag{3.5}$$

where $\mathbf{e}$ is the misfit vector.

Numerically, a common objective approach is to discretize the model into more blocks than there are degrees of freedom in the data (overparameterizing), give a resistivity for each block, then invert data for resistivities. The solution will be non-unique. The fundamental difficulty in solving the EM inverse problem is the nonuniqueness of the solution. Three approaches discussed in the last section can be applied to obtain a unique solution. The philosophy to avoid non-uniqueness is to find a model which has the minimum structure possible for a given level of data misfit. Therefore, the problem (3.5) can be modified by including a functional for measuring structure. One proposed by Smith and Booker (1991) is

$$\text{minimize} \quad obj = \iint w(x,y) \left[\frac{d^2 m}{dz^2} + g(y,z)\frac{d^2 m}{dy^2} \right]^2 dy\, dz + \beta \mathbf{e}^T \mathbf{e} \tag{3.6}$$

where $w(x,y)$ is a weight function. This can be written compactly as

$$\text{minimize} \quad W = Q + \beta\chi^2 \tag{3.7}$$

where χ^2 is the squared misfit scaled by the variances of the measurement errors, which is often called the chi-squared misfit statistic. Because of the exponential decay of EM fields as the depth increases, it is reasonable to put a larger structural penalty at depth to make parts of model, which are less constrainted by the data, smoother. Smith and Booker (1988) show that choosing $(z + z_0)^3$ is likely to result in a model fitting the data uniformly across the full frequency bandwidth. The function $g(y, z)$ allows trading-off between penalizing horizontal and vertical structures. β is a trade-off parameter between model complexity and data misfit. If β is too big, the resulting model fits noise in the data (i.e. overfits the data). In fact in 1-D the model actually approaches a series of Dirac delta functions. It is termed D^+ by Parker (1981). If β is too small, the resultant model will over-penalize structure complexity and be too smooth to fit the data. Smith and Booker (1988) presented an efficient and stable method for choosing β. In their algorithm, β is chosen in each iteration so that minimizing the object function W results in the smallest Q for a specified value of χ^2 when the linearization inherent in equations (3.3) and (3.4) are valid.

When approximated with finite differences, the problem (3.6) can be rewritten in the form

$$\text{minimize} \qquad W = (\mathbf{R}\mathbf{m} - \mathbf{c})^T(\mathbf{R}\mathbf{m} - \mathbf{c}) + \beta \mathbf{e}^T \mathbf{e} \qquad (3.8)$$

$$\text{subject to} \qquad \mathbf{d} - \mathbf{d}_0 = \mathbf{F}\mathbf{m} - \mathbf{F}\mathbf{m}_0 \qquad (3.9)$$

where $\mathbf{R}$ is a roughening matrix of dimension $(n_y \cdot n_z)$; $\mathbf{F}$ is the matrix of sensitivities of the data to changes in the model, with a dimension of $n_d \cdot (n_y \cdot n_z)$; $\mathbf{c}$ is a vector with a length of $(n_y \cdot n_z)$ which arises from penalizing the horizontal second derivative, (it expresses our bias that structure under one site must be similar to that beneath its adjacent sites); $\mathbf{m}$ and $\mathbf{m}_0$ are $(n_y \cdot n_z)$ vectors containing the new and starting models; and $\mathbf{d}$ and $\mathbf{d}_0$ are n_d element vectors containing the measured and calculated data.

Some features can be added to allow for more general problems. For instance, the apparent resistivity commonly has an unknown, frequency-independent multiplier because of static distortion of the surface electric field (Jones, 1988). Smith (1988) successfully incorporates estimation of static shifts into the inversion. In order to contain such features, one can modify equations (3.8) and (3.9) to

$$\text{minimize} \quad W = (\mathbf{Rm} - \mathbf{b})^T(\mathbf{Rm} - \mathbf{b}) + \beta \mathbf{e}^T \mathbf{e} \tag{3.10}$$

$$\text{subject to} \quad \tilde{\mathbf{d}} = \mathbf{Fm} + \mathbf{Gp} + \mathbf{e} \tag{3.11}$$

where $\tilde{\mathbf{d}}$ is defined as

$$\tilde{\mathbf{d}} = \mathbf{d} - \mathbf{d_0} + \mathbf{Fm_0} + \mathbf{Gp_0} \tag{3.12}$$

One can modify $\mathbf{c}$ (now written as $\mathbf{b}$) to allow finding models with $\mathbf{Rm}$ close to some prefered $\mathbf{b}$. $\mathbf{G}$ is the sensitivity matrix of the data to changes in the parameters $\mathbf{p}$ which one might want to consider separately from the model parameters such as static shift coefficients.

Smith (1988) derives solutions for the problem (3.10) and (3.11). First, $\tilde{\mathbf{d}}$ is rewritten as

$$\tilde{\mathbf{d}} = \left(\mathbf{FR}^{-1}\right)(\mathbf{Rm} - \mathbf{b}) + \mathbf{Gp} + \mathbf{e} + \mathbf{FR}^{-1}\mathbf{b} \tag{3.13}$$

where $\mathbf{R}$ is assumed to be full rank for simplicity. If not, a partition of $\mathbf{R}$ using a singular value depcomposition can be done and the row vectors corresponding to its zero eigenvalue can be moved into matrix $\mathbf{G}$ (Smith and Booker, 1991).

The object function (3.10) can now be minimized subject to the constraints (3.11) by introducing n_d Lagrange multipliers. After some algebra, one can derive the following formulas

$$\mathbf{e}^T \mathbf{e} = (\mathbf{d} - \mathbf{Gp})^T \mathbf{U}(\beta\lambda + \mathbf{I})^{-2}\mathbf{U}^T(\mathbf{d} - \mathbf{Gp}) \tag{3.14}$$

$$(\mathbf{m} - \mathbf{b}) = \mathbf{HU}\left(\lambda + \frac{1}{\beta}\mathbf{I}\right)^{-1}\mathbf{U}^T(\mathbf{d} - \mathbf{Gp}) \tag{3.15}$$

$$\mathbf{p} = \alpha \mathbf{d} \tag{3.16}$$

$$\alpha = \left[\mathbf{G} \mathbf{U} \left(\lambda + \frac{1}{\beta} \mathbf{I} \right) \mathbf{U}^T \mathbf{G} \right] \mathbf{G} \mathbf{U} \left(\lambda + \frac{1}{\beta} \mathbf{I} \right)^{-1} \mathbf{U}^T \qquad (3.17)$$

and

$$\mathbf{H} = \mathbf{F} \mathbf{R}^{-1} = \mathbf{U} \lambda^{\frac{1}{2}} \mathbf{V}^T \qquad (3.18)$$

where λ is a diagonal matrix with the eigenvalues of $\mathbf{H}$.

These solve the probelm (3.10) and (3.11). At each iteration, the singular value decomposition of $\mathbf{H}$ is first performed as indicated in (3.18), then Newton's method is applied to (3.14) to calculate β for a given prescribed misfit, finally, unknowns $\mathbf{p}$ and ($\mathbf{Rm} - \mathbf{b}$) are computed using (3.15) and (3.16).

3.4   A review of the RRI method of MT

3.4.1   RRI algorithm

Rapid Relaxation Inversion (RRI) of MT (Smith and Booker, 1993) is based on the observation that electric and magnetic fields can generally be expected to have smaller horizontal derivatives than vertical derivatives. Therefore, it is reasonable to approximate the horizontal second derivatives by their values from the previous iteration. This approximation makes the Fréchet kernel function of a 2-D model identical to the one derived by Oldenburg (1979) for 1-D model except the electric and magnetic fields in the kernel are computed from the 2-D model. This provides an efficient method to compute Fréchet derivatives. One can speed up the computation of model change by performing inversion at each site rather than a 2-D inversion for all sites. That is, a 2-D inversion is approximated by a set of single-site inversions. The resistivity structure beneath the observation sites is first recovered from the inversions site by site. These structures are then used to interpolate a 2-D model for calculating the 2-D EM fields required for the next iteration. The iterations continue until convergence is achieved. Further details of this method are discussed by Smith and Booker (1991).

3.4.2 Justification of the RRI

Although RRI has been successfully applied to numerous field data sets, it is useful to examine why (and when) the approximation works. No such examination has been carried out so far.

I first check the assumption about the horizontal and vertical second derivatives. Consider the configuration shown in Figure 3.1. The earth is considered to be a half-space having conductivity σ_0, except for a two-dimensional inhomogeneity with conductivity σ_1. Assuming a plane incoming wave polarized with the electric field parallel to the strike x, and with magnitude E_0 at the surface, the incident field (or primary field) inside the earth is

$$E_x^i(y, z) = E_0 e^{-ikz} \qquad (3.19)$$

Now let

$$E_x^T(y, z) = E_x^i(y, z) + E_x^s(y, z) \qquad (3.20)$$

where $E_x^T(y, z)$ and $E_x^s(y, z)$ denote the total and scattered fields. $E_x^s(y, z)$ is generated by the scattering current J_s, existing only in the inhomogeneity. J_s is given by

$$J_s = (\sigma_1 - \sigma_0) E_x^T \qquad (3.21)$$

The total field $E_x^T(y, z)$ is given by Hohmann (1971) in integral form.

$$E_x^T(y, z) = E_x^i(y, z) + \iint J_s(y', z') G(y, z; y', z') \, dy' \, dz' \qquad (3.22)$$

where G is the Green's function, which is the electric field due to a line source in the earth. The formula (3.22) is general for any two-dimensional inhomogeneity of arbitrary cross-section. If the inhomogeneity is at the surface and small enough, one can get a formula in closed form with the first order approximation to the formula (3.22)

$$E_x^T(y, z) = E_0 e^{-ikz} + \frac{iw\mu_0}{2\pi}(\sigma_1 - \sigma_0) E_0 \, K_0[ik(y^2 + z^2)] \qquad (3.23)$$

Note that far away from the inhomogeneity, the primary fields will dominate and have zero horizontal second derivatives. In the area close to the inhomogeneity, the vertical second derivatives become of the same order as the horizontal second derivatives. So I conclude the approximation is valid away from an inhomogeneity, but may be marginal near one. I do not expect, however, to see a situation where the horizontal derivative dominates the vertical derivative for these kind of models.

However, there are more extreme situations such as two abutting quarter spaces. Using the formulas for magnetic fields for the TM mode derived by d'Erceville and Kunetz (1962), one can compute the vertical and horizontal second derivatives of the magnetic fields. Figure 3.2 shows $\partial^2 H / \partial z^2$ and $\partial^2 H / \partial y^2$ at a site on the conductive side that is one half skin depth from the contact. The $\partial^2 H / \partial y^2$ curve gradually increases from zero to a maximum at about one skin depth, then decreases to zero with depth. $\partial^2 H / \partial z^2$ on the other hand is a monotonically-decreasing function of depth. $\partial^2 H / \partial z^2$ is larger than $\partial^2 H / \partial y^2$ shallower than one skin depth and smaller below one skin depth. Due to the skin depth effect, the structure within one skin depth of the surface dominates the MT response. Thus in the region MT constrains the model, the observation that vertical derivatives dominate is true. Therefore, approximating the horizontal second derivatives with quantities computed from last iteration should work well if the model change is not too large.

The second approximation is that the sensitivity of the data to the structure directly underneath is reasonable when 2-D fields are used in 1-D Fréchet derivatives. I will investigate this approximate sensitivity in the next chapter and one will see that the approximate sensitivity is verified.

3.4.3 Computation of RRI

Inversion methods for EM data typically divide the earth model into cells with constant conductivity, linearize the problem about an initial model, compute the sensitivities, solve an optimization problem to obtain model change, and update the current

Table 3.1: Methods used in several recent magnetotelluric inversion algorithms. Rapid Relaxation Inversion (Smith and Booker, 1991), OCCAM (deGroot-Hedlin and Constable, 1990), Conjugate Gradient (Mackie and Madden, 1993).

	RRI	OCCAM	Conjugate Gradient
Fwd Modeling	2-D	2-D	2-D
Sensitivity	approximate	2-D	2 Fwd modelings
Update model	small linear systems	large linear system	large linear system

model to get a new model. This process is repeated until a satisfactory model is reached. The main computation steps of this process consist of

1. Forward modeling - Computing EM response of a given resistivity model.

2. Calculating the sensitivity matrix - Computing how changes in each model parameter change each datum.

3. Solving the resulting large system of equations to compute the model change at each iteration.

A number of methods have been used for each step in EM data inversion. Table 3.1 lists some MT inversion algorithms which use different methods for these three computational steps. If one of these methods cannot be carried out in reasonable time then an alternate method is sought. Viable methods should balance accuracy, speed and computational requirements. RRI is the fastest existing method as long as its approximations hold.

For the step of forward modeling, the accuracy of forward modeling is critical to determining if a given model fits the data. Compared with other two steps, forward modeling computation is generally a small fraction of the whole inversion. Nevertheless, RRI solves the forward modeling in a fast way using an iterative method with

the fields of the last iteration as its initial values. The forward solutions converge in only a few iterations.

To compute and store the sensitivity matrix can be the most demanding stage for computer resources when fully 2-D sensitivities are used. The RRI approximate sensitivities, which will be discussed in detail in the next chapter, dramatically reduce these computer resources.

The computation of the model change is the second largest. Due to RRI approximate sensitivity, sites are not coupled in the 2-D linear inversion system. Thus, RRI is solving a number of small linear systems of equations instead of solving a large linear system of equations.

3.5 A review of previous CSAMT inversion methods

A variety of methods exist for inverting CSAMT data to find a conductivity model which fits the data. In the far-field, CSAMT data are indistinguishable from plane wave data and an obvious strategy is to use MT inversion to interpret them. This approach has been used to recover 1-D and 2-D earth models (Sasaki *et al.*, 1992; Wannamaker, 1997). The main disadvantages with this practice are that: (a) The horizontal attenuation inherent in the controlled source is not considered in the MT forward modeling; (b) data collected in the transition zone and near field cannot be utilized; and (c) it is difficult to determine where the far-field begins without knowing the electric structure of the earth. This last factor can result in significant artifacts in the model even when data is thought to be at least three skin depths away from the transmitter. Figure 3.3 shows an example from Lu *et al.* (1997). The model consists of two 10 Ωm conductive prisms embedded in 100 Ωm half-space with HEDx transmitter (Figure 3.3(a)). Figure 3.3(b) shows CSAMT synthetic data with 10% Gaussian noise. Data above the blue dash lines are three skin depths away from the source and are used as far-field data. MT inversion is used to invert those far-field

data and the recovered resistivity model is shown in Figure 3.3(c). Note the high resistivity artifact close to the source. Also note that the inversion does not recover the two conductive prisms.

An alternative approach is to attempt to correct transition zone and/or near-field data, so that it is equivalent to plane wave MT data. The corrected data are then inverted with conventional MT techniques. Various correction schemes have been proposed (Yamashita and Hallof, 1985; MacInnes, 1987; Bartel and Jacobson, 1987). Although these methods may work under some situations, the problems with this approach include: (a) the correction can not be appraised quantitatively; (b) it is physically impossible to correct CSAMT data to be MT data when the subsurface resistivity model is unknown. The correction requires an assumption about the structure. If these assumptions are wrong, the correction is wrong. Thus artifacts can be introduced into the resulting resistivity model. Figure 3.4(a) shows that the correction method cannot correct CSAMT data to be MT data. The inverted model from the corrected data gave misleading information of a relatively resistive layer at a depth where actually is a relatively conductive layer (Figure 3.4(b)).

Another approach is to use 1-D CSAMT inversion (Boerner *et al.*, 1993; Routh and Oldenburg, 1996). While this method accurately models the electromagnetic fields, it is restricted to 1-D conductivity models. This is often a useful approach for simple electric structures, but since it places the same conductivity structure beneath the transmitter and the receiver, it can give misleading results in a 2-D or 3-D environment. In order to cope with the finite source effect and the high dimensionality of electric structure in the earth, Wannamaker (1997) combined 1-D CSAMT inversion and 2-D MT inversion in field data interpretation.

Newman and Alumbaugh (1997) have developed an inversion method which models both 3-D EM sources and 3-D conductivity structures on a massively parallel computer. This approach demands expensive computational resources at the present time, but is a vital tool for evaluating inversion techniques that use a lower dimen-

sionality.

In recent years a number of approximate methods have dramatically reduced the computational cost of MT inversion (Smith and Booker, 1991; Farquharson and Oldenburg, 1995). In the next section, the approximate method of Smith and Booker will be extended to CSAMT data. 3-D transmitter fields and a 2-D earth structure are considered.

3.6 CSAMT-RRI inversion algorithm

CSAMT-RRI inversion algorithm is an extension of RRI to CSAMT inversion. Computation time for computing sensitivities is in general proportional to the time needed for forward modeling. CSAMT forward modeling is always much slower than MT forward modeling, since a higher number of dimensions and a nearly singular field close to the transmitter must be modeled. Therefore, CSAMT inversion will demand much more in computation and computer resources than MT inversion. The RRI method to invert MT data appears to be one of the fastest available, so it is natural to consider if the method will be useful for CSAMT data. This extension requires that the assumption about horizontal and vertical second derivatives is valid for CSAMT. In this section, we will investigate this assumption.

Since it is difficult to derive an analytic solution for a 2-D model and a finite source, we will compute vertical and horizontal second derivatives numerically by using the forward modeling method described in Chapter 2. Figure 3.5 shows $\partial^2 H/\partial z^2$ and $\partial^2 H/\partial y^2$ at the site on the conductive side half skin depth from the contact between two quarter spaces. The transmitter is located three skin depths from the contact and oriented in the y-direction. Both curves monotonically decrease with the depth and $\partial^2 H/\partial z^2$ is larger than $\partial^2 H/\partial y^2$ everywhere above one skin depth.

This computation shows that the fundamental approximation on which RRI is based does hold for CSAMT. Therefore, it should be possible to extend the RRI

inversion method to CSAMT. The crucial requirement for this extension is that the sensitivities can be approximated sufficiently accurately that the model perturbation leads us in the right direction. In the next chapter, I will derive CSAMT sensitivities and compare them with the true sensitivities.

In extending RRI to CSAMT data inversion, I extend it first to CSAMT data from infinite-length line source, then to data from finite sources (HED, HMD and FLHED). Although an infinite-length line source is ideal, it is the first order approximation to finite sources. Thus I first approximated a 3-D source by a 2-D infinite-length line source and modeled 2-D geoelectric structure. This is a good compromise between computation and complexity. If it had not worked for this situation, it is unlikely that it would extended to more realistic sources. Lu *et al.* (1997) inverted synthetic HED CSAMT data using an infinite-length line source. Figure 3.6 shows an example with the same model as in the direct MT inversion method described in the last section. The inverted resistivity model is shown in Figure 3.6(c). Note that the two conductive prisms are resolved well, although a resistive artifact appears close to the source. The appearance of this resistive artifact in the inverted model indicates that it is necessary to model the source more accurately in order to get reliable inversion result. Examples of CSAMT data inversion of finite sources are given in Chapter 5.
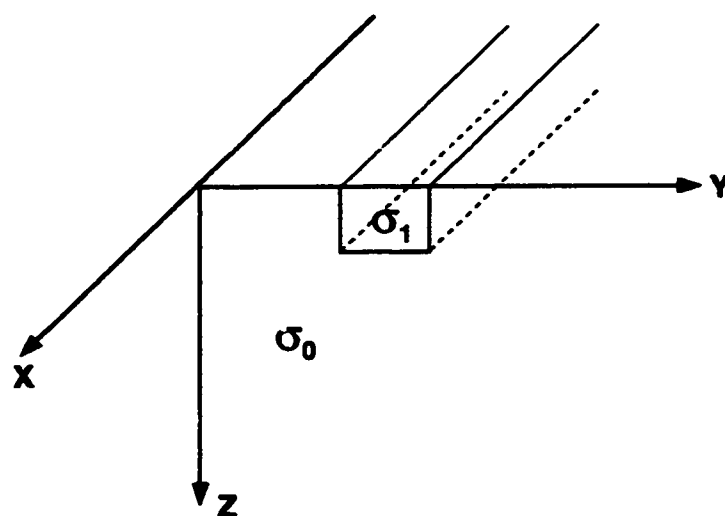
Figure 3.1: Section view of a two-dimensional inhomogeneity in the earth.
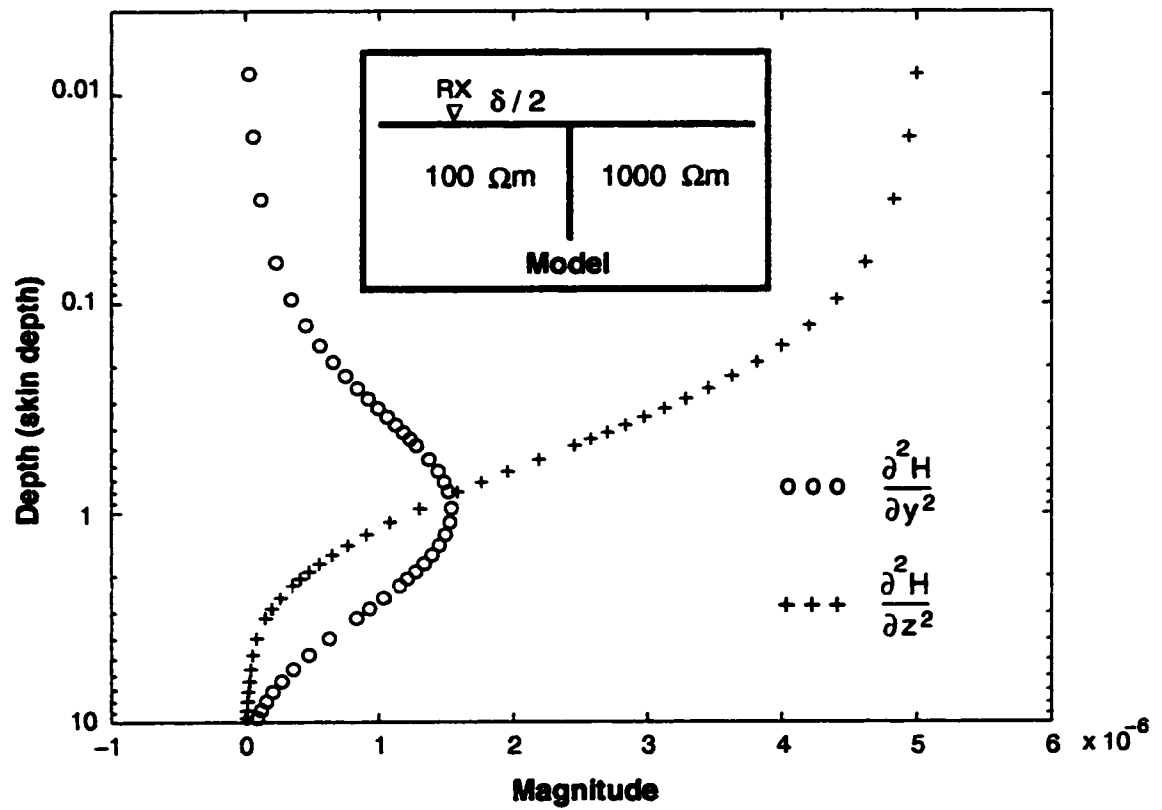
Figure 3.2: MT vertical and horizontal second derivatives of the magnetic field for a model with two abutting quarter-spaces with resistivities 100 Ωm and 1000 Ωm.
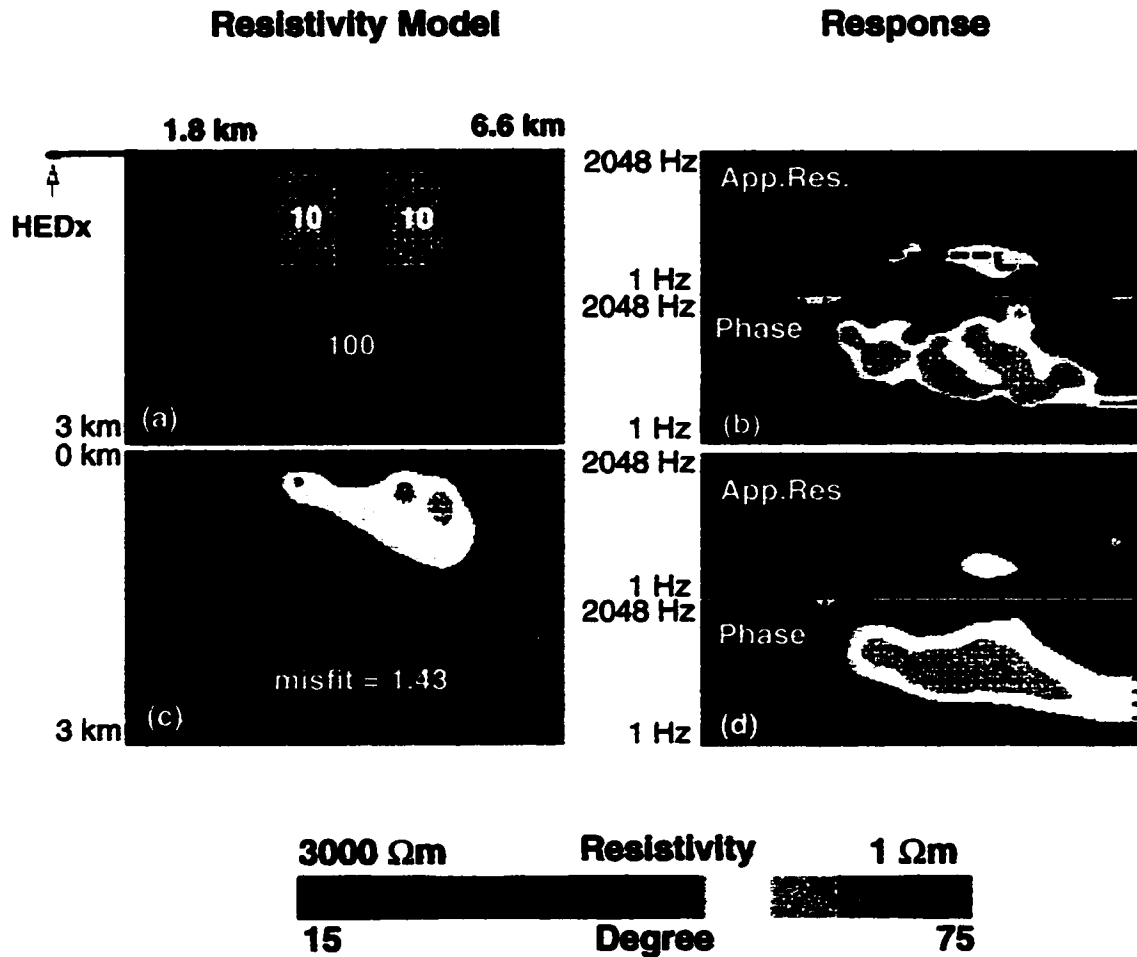
Figure 3.3: Interpreting far-field CSAMT data with MT inversion. (a) Resistivity model. (b) Synthetic data with 10% Gaussian noise. Data above the blue dashed lines are three skin depths away from an HEDx source and were used as far-field data. (c) Inverted model for the far-field CSAMT data with MT inversion. Misfit = 1.43. (d) Computed MT response of model (c).
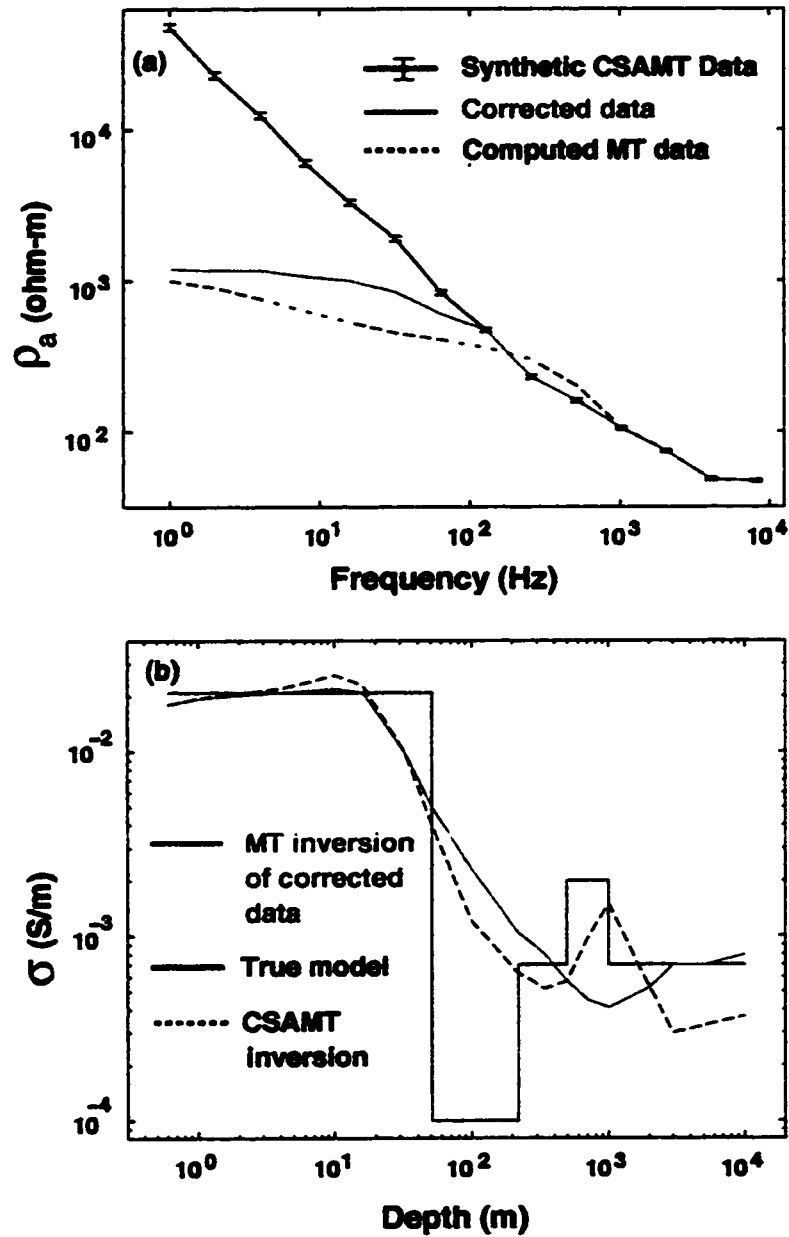
Figure 3.4: Corrected CSAMT data inversion with MT techniques. (a) Synthetic CSAMT ρ_a data, corrected ρ_a data and computed MT ρ_a data. (b) The true conductivity model, the inverted model from the corrected data and the model inverted using CSAMT inversion. (From Routh and Oldenburg (1996)).
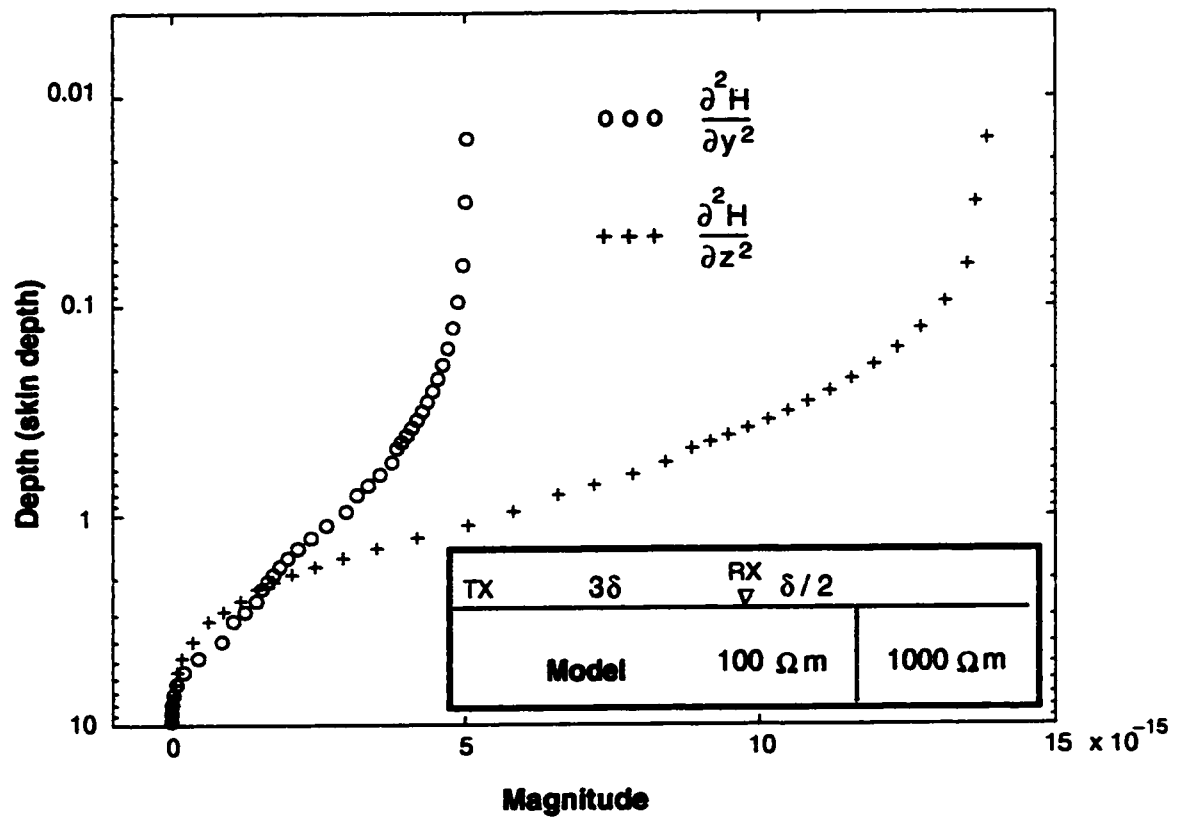
Figure 3.5: CSAMT vertical and horizontal second derivatives of the magnetic field for a two abutting quarter spaces model with resistivities 100 Ωm and 1000 Ωm.

Resistivity Model **Response**
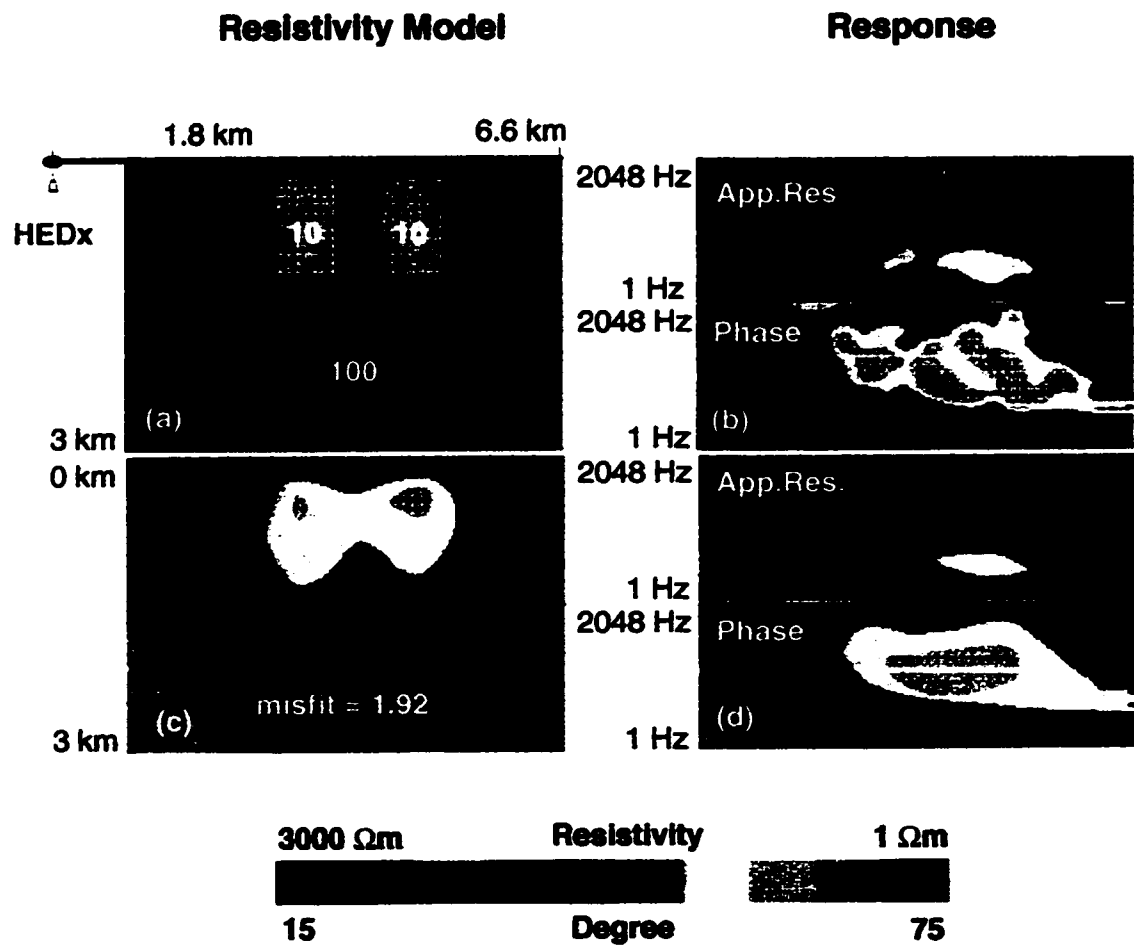
Figure 3.6: Inverting CSAMT data with infinite-length line source inversion. (a) Resistivity model. (b) Synthetic data with 10% Gaussian noise. (c) Inverted model. Misfit = 1.92. (d) Computed response of model (c).

Chapter 4

FRÉCHET DERIVATIVES AND SENSITIVITIES

In order to solve the inverse problem, one needs to compute the Fréchet derivatives or sensitivities that quantify how a change in the model affects each datum. If one part of the model is changed slightly and the data are significantly altered as a result, one can say that the observation is sensitive to this part of the model. Conversely, if there is no appreciable change in any of the data, the observation is insensitive to change in the model. Sensitivity analysis is used by geophysicists to judge the capability of geophysical measurements to detect or resolve specific geological features, or to aid in the design of better survey methods. Due to the importance of the Fréchet derivatives and sensitivities in inversion, I will focus on the computation and validity of sensitivities in this chapter. First, the Fréchet derivatives and sensitivities will be briefly introduced; then the methods of computing the Fréchet derivatives and sensitivities will be reviewed. After this, I will discuss the RRI Fréchet derivative and its features. Finally, I will derive the Fréchet derivative for CSAMT by using the perturbation analysis, and then compare them with those sensitivities from the perturbation method to justify their validity.

4.1 Introduction

The forward problem (3.1) is rewritten as

$$d_i = F_i(\mathbf{m}) \qquad i = 1, 2, \ldots, N \tag{4.1}$$

where F_i is a functional which relates a given model m to the ith datum d_i. Then, the ith observation data can be written in terms of the expansion around an estimated

model $\mathbf{m}_{est}$

$$d_i^{obs} = F_i(\mathbf{m}_{est}) + F_i^{(1)}(\mathbf{m}_{est})\delta\mathbf{m} + \frac{1}{2!}F_i^{(2)}(\mathbf{m}_{est})\delta\mathbf{m}^2 + \ldots \qquad (4.2)$$

where $F_i^{(n)}(\mathbf{m})$ is called the nth order Fréchet derivative of $F_i(\mathbf{m})$ (Griffel, 1981; Zeidler, 1985). The first-order derivative $F_i^{(1)}(\mathbf{m})$ is simply referred to as the Fréchet derivative.

The misfit δe_i for the ith observation can be written as

$$\delta e_i = F_i^{(1)}(\mathbf{m}_{est})\delta\mathbf{m} + O(\|\delta\mathbf{m}\|^2) \qquad (4.3)$$

where $\delta e_i = d_i^{obs} - F_i(\mathbf{m}_{est})$. If the high-order terms are neglected, (4.3) can be written as

$$\delta e_i = \int g_i(\mathbf{r}, \mathbf{m}_{est})\,\delta\mathbf{m}(\mathbf{r})\,d^3\mathbf{r} \qquad (4.4)$$

where $g_i(\mathbf{r}, \mathbf{m}_{est})$ is the Fréchet kernel associated with the ith observation. The Fréchet kernel function relates small changes in the model parameters to the corresponding changes in the data. The properties of Fréchet kernels determine the resolution of the inversion. For instance, if the kernel functions consist of a series of delta functions, then the model parameters may be precisely resolved. On the other hand, if the kernel functions are constant functions, only an average of the model can be obtained from the data. Normally, the kernel functions lie somewhere between delta functions and a constant. Analytic expression for the Fréchet kernel function $g_i(\mathbf{r}, \mathbf{m}_{est})$ in (4.4) is presently not available for multi-dimensional models.

In multi-dimensional inversions, the model is usually divided into a finite set of cells with parameters $m_j, j = 1, 2, \ldots, M$. The ith observation can be written in the Taylor series expansion as

$$d_i^{obs} = F_i(\mathbf{m}_{est}) + \sum_{j=1}^{M} \frac{\partial F_i(\mathbf{m}_{est})}{\partial m_j}\delta m_j + \frac{1}{2!}\sum_{j=1}^{M}\sum_{k=1}^{M} \frac{\partial^2 F_i(\mathbf{m}_{est})}{\partial m_j \, \partial m_k}\,\delta m_j\,\delta m_k + \ldots \qquad (4.5)$$

where $\partial^n F_i(\mathbf{m}_{est})/\partial m_j\,\partial m_k\cdots$ is the nth order sensitivity of $F_i(\mathbf{m})$ with respect to

the parameters $m_j, m_k, \cdots$. Then, the misfit for the ith observation can be given by

$$\delta e_i = \sum_{j=1}^{M} \frac{\partial F_i(\mathbf{m}_{est})}{\partial m_j} \delta m_j + O(\|\delta \mathbf{m}\|^2) \qquad (4.6)$$

Equation (4.6) can be rearranged in matrix form by neglecting the higher-order terms,

$$\delta \mathbf{e} = \mathbf{J} \, \delta \mathbf{m} \qquad (4.7)$$

where $\mathbf{J}$ is the sensitivity, or Jacobian, matrix. The elements of this matrix, the sensitivities, are the first-order partial derivatives of the data with respect to the model parameters.

Equations (4.4) and (4.7) are linear and can be easily solved for the model update $\delta \mathbf{m}(\mathbf{r})$. Almost all linearized inversion methods use these two equations. Computing Fréchet derivatives and sensitivities is thus a crucial step to solving most non-linear inverse problems.

4.2 Methods of Computing Fréchet Derivatives and Sensitivities

Inverse problems which have been solved using Fréchet derivatives and sensitivities include the DC resistivity inverse problem (Oldenburg, 1978), MT (Rodi, 1976; Parker, 1977; Jupp and Vozoff, 1977; Oldenburg, 1979; Hohmann and Raiche, 1988; Smith and Booker, 1991), the EM induction problem (Oristaglio and Worthington, 1980; Chave, 1984), the seismic problem (Tarantola, 1984; Chen, 1985), the ground water flow problem (Neuman, 1980; Sykes and Wilson, 1984; Townley and Wilson, 1985), the reservoir evaluation problem (Carter et al., 1974), computer-aided design problems (Branin, 1973; Brayton and Spence, 1980), and others. The problems are so diverse that a range of methods for computing Fréchet derivatives and sensitivities have been developed. They can be classified as

1. Analytic

2. Perturbation

3. Sensitivity-equation

4. Adjoint-equation

5. Approximation

McGillivray and Oldenburg (1990) give an excellent review on the first four methods. In this section, I will briefly outline those methods largely by following McGillivray and Oldenburg (1990).

4.2.1 Analytic methods

Adjoint Green's function approach

By applying perturbation analysis to equation (2.40), one can get the first-order equation for δV

$$\mathcal{D}\delta V = R(\mathbf{r}) \tag{4.8}$$

where $R(\mathbf{r}) = -\delta\mathcal{D}V$, $\delta\mathcal{D}$ is a new differential operator. The problem (4.8) concerns the Fréchet derivative δV and can be solved by using the adjoint Green's function (Lanczos, 1960; Roach, 1982). The adjoint problem is defined as

$$\mathcal{D}^*G^* = \delta(\mathbf{r}, \mathbf{r}_0) \tag{4.9}$$

where $\mathcal{D}^*$ is the adjoint operator, which is defined below. G^* is then called the adjoint Green's function and $\delta(\mathbf{r}, \mathbf{r}_0)$ is the Dirac delta function. Multiplying (4.8) by G^* and (4.9) by δV, subtracting and integrating over the domain Ω, leads to the Fréchet derivative

$$\delta V(\mathbf{r}_0) = \int_\Omega G^*(\mathbf{r}, \mathbf{r}_0)\, R(\mathbf{r})\, d\Omega \tag{4.10}$$

where the operator $\mathcal{D}^*$ and the adjoint boundary conditions are chosen such that

$$\int_\Omega (G^*\mathcal{D}\,\delta V - \delta V\,\mathcal{D}^*G^*)d\Omega = 0 \tag{4.11}$$

for all G^* and δV.

Equation (4.10) shows that computing the response perturbation $\delta V(\mathbf{r}_0)$ at $\mathbf{r}_0$ due to a unit source at $\mathbf{r}$ is equivalent to calculating the adjoint Green's function at $\mathbf{r}$ from a unit source at $\mathbf{r}_0$ and then superposing the complete source term $R(\mathbf{r})$. This property is called reciprocity. Parker (1977) used this approach to derive the Fréchet derivative for the 1-D MT problem and Chave (1984) obtained the Fréchet derivative for the 1-D EM induction problem.

Series expansion approach

This approach is based on writing the response of a perturbed system in terms of a Taylor series expansion. Fundamentally, this approach is not different from the adjoint Green's function approach, but it shows how higher-order Fréchet derivatives can be evaluated. For example, the normalized response $\tilde{S}$ for 1-D DC resistivity problem can be written as

$$\frac{d^2\tilde{S}}{dz^2} - w(z)\frac{d\tilde{S}}{dz} - \lambda^2\tilde{S} = 0 \tag{4.12}$$

where $w(z)$ is the model, $\tilde{S} = \lambda\tilde{\phi}(\lambda,z)/(\lambda\tilde{\phi}(\lambda,0))'$ and $\tilde{\phi}$ is the Hankel transform of the potential ϕ. By writing $\tilde{S}$ in terms of a Taylor series expansion, substituting it into (4.12) and rearranging, one can obtain a relationship between higher-order Fréchet derivatives with lower-order Fréchet derivatives

$$\frac{d^2\tilde{S}_k}{dz^2} - w(z)\frac{d\tilde{S}_k}{dz} - \lambda^2\tilde{S}_k = k\eta\frac{d\tilde{S}_{k-1}}{dz} \qquad k = 1, 2, \ldots \tag{4.13}$$

where $\tilde{S}_k = \partial^k\tilde{S}/\partial\varepsilon^k$, $\delta w(z) = \varepsilon\eta(z)$. Equation (4.13) can be solved to get higher-order Fréchet derivatives using the adjoint Green's function.

Riccati equation approach

This approach is restricted to the second-order homogeneous linear equation in one-dimension.

$$V''(z) + A(z)V'(z) + B(z)V(z) = 0 \tag{4.14}$$

Equation (4.14) can be transformed to the Riccati equation by using the substitution

$$y(z) = -\frac{V'(z)}{a(z)V(z)} \qquad (4.15)$$

or

$$y(z) = -\frac{a(z)V(z)}{V'(z)} \qquad (4.16)$$

Then the Riccati equation for δy can be obtained by perturbating the model and solved by using standard techniques such as the integrating factor technique. Oldenburg (1978, 1979) uses this approach to derive the Fréchet derivatives for the 1-D DC resistivity problem and the 1-D MT problem.

Although the adjoint Green's function approach is general and yields an expression in integral form for the Fréchet derivative, solving for the adjoint Green's function is theoretically as hard as the problem itself. Nevertheless, the computation can be decreased by using the reciprocity of the adjoint Green's function. So far, those analytic approaches are only successful in deriving Fréchet derivatives for one-dimensional problems. For multi-dimensional problems, one must make use of the parameter sensitivities, which can be computed by the methods in the next section.

4.2.2 Perturbation method

The perturbation method, also called the brute-force method, computes the sensitivities by representing the derivative with the finite-difference approximation,

$$\frac{\partial F_i(\mathbf{m})}{\partial m_j} \approx \frac{F_i(\mathbf{m} + \Delta m_j) - F_i(\mathbf{m})}{\Delta m_j} \qquad (4.17)$$

The method requires two forward calculations for each parameter, but $M+1$ forward calculations for all M parameters. This method is straightforward, but it is very inefficient and often impractical in inversion.

4.2.3 Sensitivity-equation method

Equations (2.36) and (2.37) represent a steady-state diffusion problem, which can be described by the following boundary-value problem

$$-\nabla \cdot (m(\mathbf{r}) \nabla V) + q(\mathbf{r}) V = Q(\mathbf{r}) \quad in \quad \Omega \tag{4.18}$$

$$\alpha(\mathbf{r})V + \beta(\mathbf{r})\frac{\partial V}{\partial n} = 0 \quad on \quad \partial\Omega \tag{4.19}$$

where $m(\mathbf{r})$ and $q(\mathbf{r})$ jointly specify the model and $Q(\mathbf{r})$ describes the source distribution. If $m(\mathbf{r})$ is taken as the model and is parameterized by

$$m(\mathbf{r}) = \sum_{i=1}^{M} m_i \psi_i(\mathbf{r}) \tag{4.20}$$

where $\{\psi_i\}$ is set of basis function, the above boundary-value problem can be written as

$$-\nabla \cdot \left(\sum_{i=1}^{M} m_i \psi_i(\mathbf{r}) \nabla V\right) + q(\mathbf{r}) V = Q(\mathbf{r}) \quad in \quad \Omega \tag{4.21}$$

$$\alpha(\mathbf{r})V + \beta(\mathbf{r})\frac{\partial V}{\partial n} = 0 \quad on \quad \partial\Omega \tag{4.22}$$

Differentiating (4.21) and (4.22) with respect to m_i, yields

$$-\nabla \cdot \left(m(\mathbf{r}) \nabla \frac{\partial V(\mathbf{r})}{\partial m_i}\right) + q(\mathbf{r})\frac{\partial V(\mathbf{r})}{\partial m_i} = \nabla \cdot (\psi_i(\mathbf{r}) \nabla V) \quad in \quad \Omega \tag{4.23}$$

$$\alpha(\mathbf{r})\frac{\partial V(\mathbf{r})}{\partial m_i} + \beta(\mathbf{r})\frac{\partial}{\partial n}\left(\frac{\partial V(\mathbf{r})}{\partial m_i}\right) = 0 \quad on \quad \partial\Omega \tag{4.24}$$

Equations (4.23) and (4.24) are called the sensitivity problem and can be solved for the sensitivities $\partial V(\mathbf{r})/\partial m_i$ in the following manner. First, the forward problem (4.18) and (4.19) is solved for $V(\mathbf{r})$ at all points $\mathbf{r}$ in Ω, then the corresponding sensitivity problem is solved to get $\partial V(\mathbf{r})/\partial m_i$ for each model parameter m_i. Thus a total of $M + 1$ forward problems have to be solved to obtain all sensitivities. But they can be solved efficiently by a direct method such as the *LU* decomposition, since the original forward problem and the sensitivity problems differ only in their

source terms. Obviously, this method is more efficient than the perturbation method, but its computation is still very demanding. Rodi (1976), Jupp and Vozoff (1977), Hohmann and Raiche (1988) use this method for the 2-D MT problem, Oristaglio and Worthington use it for the 2-D induction problem with a line source.

4.2.4 Adjoint-equation method

The adjoint-equation method is based on the adjoint Green's function concept discussed earlier. The adjoint problem for (4.18) and (4.19) is constructed as

$$-\nabla \cdot (m(\mathbf{r}) \nabla G^*) + q(\mathbf{r}) G^* = \delta(\mathbf{r}, \mathbf{r}_j) \qquad in \quad \Omega \tag{4.25}$$

$$\alpha(\mathbf{r})G^* + \beta(\mathbf{r})\frac{\partial G^*}{\partial n} = 0 \qquad on \quad \partial\Omega \tag{4.26}$$

Following the similar derivation to that for Adjoint Green's function approach, one can obtain,

$$\frac{\partial V(\mathbf{r}_j)}{\partial m_i} = \int_\Omega G^* \nabla \cdot (\psi_i \nabla V) d\Omega \tag{4.27}$$

To compute the sensitivities, the adjoint problem (4.25) and (4.26) must be solved for each observation site $\mathbf{r}_j$. Then, equation (4.27) is used to compute sensitivities for each parameter. Since the source term in the adjoint problem differs for each observation site, a total of $N + 1$ forward problems must be solved. Again, this can be done efficiently by a factorization method (e.g. LU). Generally, the number of model parameters is considerably greater than the number of data, so the adjoint-equation method is the most efficient method to compute exact sensitivities. This method is used by Weildelt (1975) and Madden and Mackie (1989).

4.2.5 Conjugate Gradient method

Mackie and Madden (1993) use a conjugate gradient approach for solving the magnetotelluric inverse problem that does not explicitly need the sensitivity matrix but rather the effects of this matrix or its transpose multiplying a given vector. They show

that each of these requires one forward problem with a distributed set of sources either in the volume (for the sensitivity matrix multiplying a vector) or on the surface (for the transpose multiplying a vector). Although this significantly reduces the computational requirements, it still needs three forward-modelings with various sources for each inversion iteration.

4.2.6 Approximation methods

The approximation method of RRI (Smith and Booker, 1991) is based on the one-dimensional Fréchet derivative, but uses two-dimensional forward calculations. No extra forward calculation is required. Therefore it is extremely fast. The sensitivity matrix is not only approximate but also incomplete. Its derivation, features and accuracy will be discussed in the following section. I refer to this method as the RRI approximation method.

Farquharson and Oldenburg (1995) present an approximation method which is based on the adjoint-equation method. In the adjoint-equation method, the sensitivities are obtained by integrating the product of an adjoint field (the adjoint Green's function) with the field generated by the forward calculation of the last iteration. They approximate the adjoint field either by computing fields from a homogeneous or layered half-space, or by using the Born approximation, instead of computing the adjoint field from the updated model at each iteration. This method can reasonably be called the approximate adjoint-equation method. It also requires no extra forward calculation. The sensitivity matrix generated by this method is approximate, but complete.

An approximation method should be considerably faster than exact methods but needs to be sufficiently accurate to allow an iterative inversion algorithm to converge to the solution.

4.2.7 Comparison of sensitivity computations

In conclusion, the analytic Fréchet derivative is the most convenient way to compute sensitivity, but it is normally restricted to one-dimensional models. For multi-dimensional models, parameter sensitivities are calculated either exactly by perturbation, sensitivity-equation and adjoint-equation methods, or approximately by the approximation methods. The perturbation method requires a large number of forward calculations and is not practically feasible in general. The sensitivity-equation and adjoint-equation methods compute sensitivities more efficiently if a numerical solution for the forward calculation based on a matrix factorization is used, but the computation for the sensitivities still requires considerable time. The approximation methods generate fast sensitivities for inversion and have been shown to be sufficiently accurate for the MT inversion.

Relative computation times for each method are listed in Table 4.1. As the size of the problem increases, the amount of computation becomes increasingly unrealistic for perturbation, sensitivity-equation and adjoint equation methods. Thus the conjugate gradient and approximation methods become attractive. I will use the RRI approximation method for CSAMT data inversion.

4.3 RRI Sensitivities

4.3.1 Derivation of RRI sensitivities

In this section I will outline the extension of RRI sensitivity to CSAMT.

TE mode

First, consider the transverse electric (TE) mode in which the electric field (E_x) is parallel to the strike of the structure. For a 2-D electric model $\sigma(y, z)$, with x aligned with strike, y perpendicular to strike and z positive downward, the governing equation

Table 4.1: Comparison of Computation Time. M is the number of model parameters, N_f is the number of frequencies, and N_{obs} is the number of observation sites. A typical 2-D example: $M = 100 \times 100$, $N_f = 20$, $N_{obs} = 20$.

Method	No. of Forward Modeling	A Typical Example
Brute-Force	$M \times N_f$	10000×20
Sensitivity-Equation	$M \times N_f$	10000×20
Adjoint-Equation	$N_f \times N_{obs}$	20×20
Conjugate-Gradient	$3 \times N_f$	3×20
Approximation	N_f	20

for E_x is given by

$$\frac{1}{E_x}\frac{\partial^2 E_x}{\partial z^2} + \frac{1}{E_x}\frac{\partial^2 E_x}{\partial y^2} + i\omega\mu_0\sigma = 0 \tag{4.28}$$

The datum V is defined as

$$V = \frac{1}{E_x}\frac{\partial E_x}{\partial z} = i\omega\mu_0\frac{H_y}{E_x} = i\omega\mu_0\frac{1}{Z_{xy}} \tag{4.29}$$

From this definition, (4.28) can be written as

$$\frac{\partial V}{\partial z} + V^2 + \left\{\frac{1}{E_x}\frac{\partial^2 E_x}{\partial y^2}\right\} + i\omega\mu_0\sigma = 0 \tag{4.30}$$

Suppose that V_0 and E_{x0} satisfy equation (4.30) when $\sigma = \sigma_0$, and $V = V_0 + \delta V$ when $\sigma = \sigma_0 + \delta\sigma$. Due to the skin depth effect, the horizontal gradients in braces are normally smaller than the vertical gradients, and are approximated by

$$\frac{1}{E_x}\frac{\partial^2 E_x}{\partial y^2} = \frac{1}{E_{x0}}\frac{\partial^2 E_{x0}}{\partial y^2} \tag{4.31}$$

Applying the perturbation analysis to equation (4.30) and neglecting higher-order terms, one obtains the first-order linear differential equation for δV,

$$\frac{\partial}{\partial z}\delta V + 2V_0\delta V + i\omega\mu_0\delta\sigma = 0 \tag{4.32}$$

It can be solved for δV to yield

$$\delta V(y_i, 0) = \frac{i\omega\mu_0}{E_{x0}^2(y_i, 0)} \int E_{x0}^2(y_i, z)\delta\sigma(z)dz \tag{4.33}$$

Equation (4.33) describes the Fréchet derivative of $1/Z_{xy}$.

Apparent resistivity ρ_a and phase ϕ are usually used as data. If d_{TE} is defined as

$$d_{TE} = \ln\left[-i\omega\mu_0\left(\frac{H_y}{E_x}\right)^2\right] = \ln\left(\frac{V^2}{-i\omega\mu_0}\right) \tag{4.34}$$

it has the following relationship with ρ_a and ϕ,

$$Re[d_{TE}] = -\ln\rho_a \qquad Im[d_{TE}] = \frac{3\pi}{2} - 2\phi \tag{4.35}$$

By differentiating equation (4.34), one can easily derive

$$\delta d_{TE} = \frac{2}{V(y_i, 0)}\delta V = \int \frac{2\sigma_0(z)E_{x0}^2(y_i, z)}{E_{x0}(y_i, 0)H_{y0}(y_i, 0)}\delta(\ln\sigma(z))dz \tag{4.36}$$

TM mode

The governing equation for the TM mode can be written as

$$\frac{1}{H_x}\frac{\partial}{\partial z}\rho\frac{\partial H_x}{\partial z} + \frac{1}{H_x}\frac{\partial}{\partial y}\rho\frac{\partial H_x}{\partial y} + i\omega\mu_0\sigma = 0 \tag{4.37}$$

The datum is defined as

$$U = \frac{\rho}{H_x}\frac{\partial H_x}{\partial z} = \frac{E_y}{H_x} = Z_{yx} \tag{4.38}$$

Similarly, one can derive the Fréchet derivative δU

$$\delta U(y_i, 0) = \frac{1}{H_{x0}^2(y_i, 0)} \int E_{y0}^2(y_i, z)\delta\sigma(z)dz \tag{4.39}$$

For TM apparent resistivity and phase, one can define

$$d_{TM} = \ln\left[-i\omega\mu_0\left(\frac{H_x}{E_y}\right)^2\right] = \ln\left(\frac{-i\omega\mu_0}{U^2}\right) \tag{4.40}$$

where d_{TM} is related to ρ_a and ϕ in exactly analogous form as (4.35). Then one can get

$$\delta d_{TM} = -\frac{2}{U(y_i, 0)}\delta U = \int \frac{-2\sigma_0(z)E_{y0}^2(y_i, z)}{E_{y0}(y_i, 0)H_{x0}(y_i, 0)}\delta(\ln\sigma(z))dz \tag{4.41}$$

Equations (4.33) and (4.39) are scaled Fréchet derivatives of impedances $1/Z_{xy}$ and Z_{yx}, while Equations (4.36) and (4.41) are Fréchet derivatives for apparent resistivities and phases. Equations (4.33) and (4.39) have the same form as that obtained by Oldenburg (1979) for the 1-D problem, but use 2-D fields from the last iteration instead of the 1-D fields. Equations (4.33), (4.39), (4.36) and (4.41) are a relationship between data residuals and model changes. So these four equations can be inverted for model changes directly beneath the site.

The complete RRI iterative cycle is as follows: Given an initial model $\sigma_0(y, z)$, equations (4.28) and (4.37) are solved for $E_{x0}(y, z)$ and $H_{x0}(y, z)$. These fields are used to compute the Fréchet kernels of equations (4.33) and (4.39) (or (4.36) and (4.41)) and the data residuals at each site. Equations (4.33) and (4.39) (or (4.36) and (4.41)) are then inverted for the model update $\delta\sigma$ directly beneath the site. Then $\sigma(y_i, z)$ is updated at all sites and interpolated between sites to generate a new 2-D model $\sigma(y, z)$. Equations (4.28) and (4.37) are solved again for the fields of the updated model. This cycle is repeated until a satisfactory fit to the observed data is reached.

4.3.2   RRI sensitivity matrix

RRI inverts data site by site and constructs a new 2-D model by interpolation. Thus RRI does not explicitly use the 2-D sensitivity matrix J defined in equation (4.7). This is the major difference from the standard inversion method and makes comparison difficult between RRI and other inversion methods. This difference can be eliminated by constructing an RRI sensitivity matrix based on its inversion scheme.

The standard inversion method computes a fully-2D sensitivity matrix, which relates data to the change of *each* model cell. RRI computes the sensitivities of the data only to the cells which are directly below the measurement site, but does not use the sensitivities to the cells that are not directly below the measurement site (for ease, side cells). RRI's site by site inversion scheme is equivalent to setting the

side cell sensitivities to zero. Therefore the RRI sensitivity matrix can be related to the standard sensitivity matrix in this way: The sensitivities of data to the cells directly below its site are computed from the formulas (4.36) and (4.41) and the sensitivities of data to side cells are approximated to be zero. Setting sensitivities of data to side cells to zero enables RRI to (1) invert data site by site rather than do a 2-D inversion for all sites at once and (2) require much less computation time and memory for model changes. The accuracy of the sensitivity matrix is crucial to inversion convergence. Therefore it is important to check how close the RRI sensitivity is to the true sensitivity.

Figure 4.1 (a) and (b) show sensitivities of apparent resistivity ρ_a and phase ϕ respectively from RRI and the perturbation method over 100 Ωm half-space at the frequency of 64 Hz. $d\rho_a/d\sigma_i$ and $d\phi/d\sigma_i$ are normalized by the thickness of the perturbed cell. From Figure 4.1 (a), note that $d\rho_a/d\sigma_i$ and $d\phi/d\sigma_i$ for TE and TM modes from RRI are the same for the half-space model (this is also true for any 1-D layered model). Also note that $d\rho_a/d\sigma_i$ from RRI is larger than TE $d\rho_a/d\sigma_i$ because of the different volumes perturbed in each case. The perturbation sensitivity is with respect to a cell of finite width, whereas the RRI sensitivity for this cell is equivalent to perturbating an infinitely wide layer. Also note that perturbation TM $d\rho_a/d\sigma_i$ is larger than both RRI sensitivity and perturbation TE $d\rho_a/d\sigma_i$. This can be understood to be the result of charges that build up on the two side surfaces of the perturbed cell for TM mode. The sensitivities of apparent resistivity from both methods quickly decay to zero below one skin depth. Figure 4.1 (b) shows that TE $d\phi/d\sigma_i$ from the perturbation method is larger than TM $d\phi/d\sigma_i$ from the perturbation method. This can be explained by looking at the physical meaning of phase. Phase is not related to the magnitude of the impedance, but concerns how quickly the electric field responds to a change of the magnetic field. The charges built on the edges of the perturbed cell for the TM mode slow down the response of the electric field caused by the perturbation of the conductivity σ_i of the cell.

Thus one can expect that $d\phi/d\sigma_i$ from RRI should be closer to TE $d\phi/d\sigma_i$ from the perturbation method than to TM $d\phi/d\sigma_i$ from the perturbation method. The shape of $d\phi/d\sigma_i$ from RRI is very similar to the shape, but larger than the magnitude of TE $d\phi/d\sigma_i$ from the perturbation method. Also note that the sensitivities of phase decay to zero below two skin depths, which indicates that phase is more sensitive to deep structure than apparent resistivity. Overall, for this simple model, it is observed that the corresponding Fréchet derivatives for $d\rho_a/d\sigma_i$ and $d\phi/d\sigma_i$ from both RRI and the perturbation method are broadly similar in shape, although they have different magnitudes. A more thorough comparison of the RRI and true sensitivities of data to the cells directly below the site will be made in Section 4.5 with the same conclusion.

While RRI approximates sensitivities in cells directly below each site by the formulas (4.36) and (4.41), it approximates sensitivities to side cells by zero. The approximation of setting sensitivities of data to side cells zero seems very crude. But if the resulting model beneath each site from "pseudo" 1-D inversions is close enough to the correct model, the roughness of this approximation may be compensated by the interpolation of the 2-D model from the 1-D models. So far numerous synthetic and field data inversions show that this approximation often works well.

4.3.3 Horizontal derivatives

Equation (4.41) can be rewritten as

$$\delta d_{TM} = -\frac{2}{E_{y0}(y_i,0)H_{x0}(y_i,0)} \int \frac{1}{\sigma(y_i,z)} \left(\frac{\partial H_{x0}(y_i,z)}{\partial z} \right)^2 \delta(\ln\sigma(y_i,z))dz \qquad (4.42)$$

The Fréchet kernel function in this equation only has the vertical derivative of the magnetic field. For a multi-dimensional model, at first thought, it would be expected that the Fréchet kernel function should include both vertical and horizontal derivatives, because structures not only directly below but also horizontally adjacent to the site have significant contributions to the measurement at this site. It seems that RRI would do better if the horizontal derivative was included. This is what Yamane *et al.*

(1996) attempted with their generalized RRI algorithm (or GRRI). Integrating over a domain consisting of just one vertical column instead of three columns and assuming small model perturbation, equation (10) of the GRRI paper can be simplified to

$$\delta d_{TM} = -\frac{2}{E_{y0}(y_i, 0) H_{x0}(y_i, 0)} \int \frac{1}{\sigma(y_i, z)} \left[\left(\frac{\partial H_{x0}(y_i, z)}{\partial y}\right)^2 + \left(\frac{\partial H_{x0}(y_i, z)}{\partial z}\right)^2 \right] \delta(\ln \sigma(y_i, z)) dz \tag{4.43}$$

Equation (4.43) includes the horizontal derivative as well as the vertical derivative of the magnetic field.

Sensitivities of apparent resistivity and phase can be easily computed from equations (4.42) and (4.43). Figures 4.2 (a) and (b) show sensitivities of TM apparent resistivity and phase from the perturbation method, RRI and GRRI for the same two quarter-space model shown in Figure 3.2. Note that the perturbation method and RRI give very similar curves in shape, which decrease in magnitude with depth. However GRRI gives very different curves, which oscillate with depth and have much larger magnitudes at one skin depth than at the shallow depths. This contradicts the nature of the diffusion process. Physically, MT is more sensitive to the shallow structures than to the deep ones. The only difference between equation (4.42) and (4.43) is the horizontal derivative, therefore, the horizontal derivative should not be included in the Fréchet kernel function. Also note that RRI and GRRI have almost identical Fréchet derivatives at shallow depths because the horizontal derivative is very small near to the surface. Looking closely at the RRI derivation, it can been seen that RRI does consider the horizontal derivatives by approximating them with those from last iteration, rather than simply discarding them. So where should the contribution from the structures horizontally adjacent to the measurement site be represented in the sensitivities? The contribution should be represented by the sensitivities of data to side cells. In RRI, the affect of adjacent structures enters indirectly through the use of the 2-D fields. Thus even though the side cell sensitivities are set to zero, the side

cells affect the next iteration because the 2-D fields will change.

4.3.4 Inversion examples

In this section, RRI and GRRI will be tested on two synthetic models. GRRI is developed by incorporating horizontal derivative into the Fréchet kernel function based on equation (4.43). It just has one column of cells in the "pseudo" 1-D inversion. GRRI (Yamane et al., 1996) uses three adjacent columns together in the inversion, but under the constraint of seeking the smoothest model, these three adjacent columns are very similar to each other. Therefore, no significant improvement could be gained from having three adjacent columns as long as no new site is included.

Figure 4.3 shows the inversion results from RRI and GRRI inversions for the two quarter-space model. Both recover very similar models and fit the data well. RRI fits the data to a misfit of 1.44 while GRRI fits the data with misfit of 1.67. The ideal misfit is 1.0. Figure 4.2 shows that including horizontal derivative causes severe deviation from the correct sensitivity, especially at depth, but surprisingly, GRRI still converges to a model that is almost identical model to that derived by RRI. This can be explained as follows. Horizontal derivatives quickly decrease to zero with the distance from the contact, so only a fraction of the data is strongly affected by the horizontal derivative. This implies that even though sensitivities of a small part of the data are not correct, inversion can still progress in the correct direction if the sensitivities of a majority of data are accurate enough.

Figure 4.4 shows inversion results from RRI and GRRI for a more complicated model, which is two dipping prism model with conductive overburden. RRI and GRRI give almost identical models and the same data misfits. Horizontal derivatives of any intermediate inversion model for this inversion starting from 100 Ωm half-space are very small, so the two Fréchet kernel functions are almost the same.

4.4 CSAMT-RRI sensitivities

In this section, I will derive the approximate sensitivities for CSAMT. The derivation is identical to that used by Smith and Booker (1991) for the MT inverse problem.

The governing equations (2.20) and (2.22) is the starting point to derive the approximate sensitivities for CSAMT. If extrinsic sources $\mathbf{J}_e^s$ and $\mathbf{J}_m^s$ are given by

$$\mathbf{J}_e^s = J_{ex}\mathbf{x} + J_{ey}\mathbf{y} + J_{ez}\mathbf{z} \tag{4.44}$$

and ·

$$\mathbf{J}_m^s = J_{mx}\mathbf{x} + J_{my}\mathbf{y} + J_{mz}\mathbf{z} \tag{4.45}$$

where $\mathbf{x}, \mathbf{y}, \mathbf{z}$ are the unit vectors in x, y, z—directions, respectively. The expressions for the components of $\mathbf{E}$ and $\mathbf{H}$ in equations (2.20) and (2.22) are in Cartesian coordinates given by

$$-\nabla^2 E_x - i\omega\mu_0\sigma E_x = i\omega\mu_0 J_{ex} - \left(\frac{\partial}{\partial y}J_{mz} - \frac{\partial}{\partial z}J_{my}\right) \tag{4.46}$$

$$-\nabla^2 E_y - i\omega\mu_0\sigma E_y = i\omega\mu_0 J_{ey} - \left(\frac{\partial}{\partial z}J_{mx} - \frac{\partial}{\partial x}J_{mz}\right) \tag{4.47}$$

$$-\nabla^2 E_z - i\omega\mu_0\sigma E_z = i\omega\mu_0 J_{ez} - \left(-\frac{\partial}{\partial y}J_{mx} + \frac{\partial}{\partial x}J_{my}\right) \tag{4.48}$$

and

$$-\nabla^2 H_x - i\omega\mu_0\sigma H_x = -\sigma J_{mx} - \left(\frac{\partial}{\partial y}J_{ez} - \frac{\partial}{\partial z}J_{ey}\right) \tag{4.49}$$

$$-\nabla^2 H_y - i\omega\mu_0\sigma H_y = -\sigma J_{my} - \left(\frac{\partial}{\partial z}J_{ex} - \frac{\partial}{\partial x}J_{ez}\right) \tag{4.50}$$

$$-\nabla^2 H_z - i\omega\mu_0\sigma H_z = -\sigma J_{mz} - \left(-\frac{\partial}{\partial y}J_{ex} + \frac{\partial}{\partial x}J_{ey}\right) \tag{4.51}$$

where $\nabla^2 = \partial^2/\partial x^2 + \partial^2/\partial y^2 + \partial^2/\partial z^2$.

4.4.1   Horizontal electric dipole parallel to the strike (HEDx)

A horizontal electric dipole source parallel to the strike, which is located at the origin, can be expressed as

$$\mathbf{J}_e^s = Idl\delta(x)\delta(y)\delta(z)\mathbf{x} \qquad (4.52)$$

where Idl is the dipole moment. Substituting in the above equations and setting $\mathbf{J}_m^s = 0$, one has the TE mode with (E_x, H_y)

$$\frac{1}{E_x}\frac{\partial^2 E_x}{\partial x^2} + \frac{1}{E_x}\frac{\partial^2 E_x}{\partial y^2} + \frac{1}{E_x}\frac{\partial^2 E_x}{\partial z^2} + i\omega\mu_0\sigma = \frac{1}{E_x}i\omega\mu_0 Idl\delta_{(x)}\delta_{(y)}\delta_{(z)} \qquad (4.53)$$

$$\frac{\partial E_x}{\partial z} - \frac{\partial E_z}{\partial x} = i\omega\mu_0 H_y \qquad (4.54)$$

and the TM mode with (E_y, H_x)

$$\frac{1}{H_x}\frac{\partial}{\partial x}\frac{1}{\sigma}\frac{\partial H_x}{\partial x} + \frac{1}{H_x}\frac{\partial}{\partial y}\frac{1}{\sigma}\frac{\partial H_x}{\partial y} + \frac{1}{H_x}\frac{\partial}{\partial z}\frac{1}{\sigma}\frac{\partial H_x}{\partial z} + i\omega\mu_0 = 0 \qquad (4.55)$$

$$\frac{\partial H_x}{\partial z} - \frac{\partial H_z}{\partial x} = \sigma E_y \qquad (4.56)$$

TE mode

With the same definition for the datum V as (4.29), the perturbation analysis can be applied to equation (4.53). If the perturbation $\delta\sigma$ is small enough, one can make the following approximations,

$$\frac{1}{E_x}\frac{\partial^2 E_x}{\partial x^2} = \frac{1}{E_{x0}}\frac{\partial^2 E_{x0}}{\partial x^2} \qquad (4.57)$$

$$\frac{1}{E_x}\frac{\partial^2 E_x}{\partial y^2} = \frac{1}{E_{x0}}\frac{\partial^2 E_{x0}}{\partial y^2} \qquad (4.58)$$

$$\frac{1}{E_x}i\omega\mu_0 Idl\delta_{(x)}\delta_{(y)}\delta_{(z)} = \frac{1}{E_{x0}}i\omega\mu_0 Idl\delta_{(x)}\delta_{(y)}\delta_{(z)} \qquad (4.59)$$

where E_{x0} satisfies equation (4.53) when $\sigma = \sigma_0$ (the starting model or the model from last iteration, not the model for computing primary fields in forward modeling), and get the same differential equation as (4.32) for δV. Therefore,

$$\delta V(x_i, y_i, 0) = \frac{i\omega\mu_0}{E_{x0}^2(x_i, y_i, 0)}\int E_{x0}^2(x_i, y_i, z)\delta\sigma(z)dz \qquad (4.60)$$

TM mode

Similarly, defining the data U as in (4.38), applying the the perturbation analysis to equation (4.55), and making the following approximations

$$\frac{1}{H_x}\frac{\partial}{\partial x}\frac{1}{\sigma}\frac{\partial H_x}{\partial x} = \frac{1}{H_{x0}}\frac{\partial}{\partial x}\frac{1}{\sigma}\frac{\partial H_{x0}}{\partial x} \qquad (4.61)$$

$$\frac{1}{H_x}\frac{\partial}{\partial y}\frac{1}{\sigma}\frac{\partial H_x}{\partial y} = \frac{1}{H_{x0}}\frac{\partial}{\partial y}\frac{1}{\sigma}\frac{\partial H_{x0}}{\partial y} \qquad (4.62)$$

one can obtain

$$\delta U(x_i, y_i, 0) = \frac{1}{H_{x0}^2(x_i, y_i, 0)} \int E_{y0}^2(x_i, y_i, z)\delta\sigma(z)dz \qquad (4.63)$$

4.4.2 Horizontal electric dipole perpendicular to the strike (HEDy)

The relevant equations used for deriving the approximate sensitivities with the horizontal electric dipole source perpendicular to the strike become, for TE mode,

$$\frac{1}{E_x}\frac{\partial^2 E_x}{\partial x^2} + \frac{1}{E_x}\frac{\partial^2 E_x}{\partial y^2} + \frac{1}{E_x}\frac{\partial^2 E_x}{\partial z^2} + i\omega\mu_0\sigma = 0 \qquad (4.64)$$

and for TM mode,

$$\frac{1}{H_x}\frac{\partial}{\partial x}\frac{1}{\sigma}\frac{\partial H_x}{\partial x} + \frac{1}{H_x}\frac{\partial}{\partial y}\frac{1}{\sigma}\frac{\partial H_x}{\partial y} + \frac{1}{H_x}\frac{\partial}{\partial z}\frac{1}{\sigma}\frac{\partial H_x}{\partial z} + i\omega\mu_0 = \frac{1}{H_x}\frac{\partial}{\partial z}(\frac{1}{\sigma}Idl\delta_{(x)}\delta_{(y)}\delta_{(z)}) \quad (4.65)$$

For this case, the HED located at the origin is represented by

$$\mathbf{J}_e^s = Idl\delta(x)\delta(y)\delta(z)\mathbf{y} \qquad (4.66)$$

After some algebra and suitable equivalents of (4.57 - 4.59) and (4.61 - 4.62) one obtains exactly the same results as (4.60) and (4.63).

4.4.3 Horizontal magnetic dipoles and finite-length horizontal electric dipoles

The horizontal magnetic dipole parallel (HMDx) and perpendicular (HMDy) to the strike, located at the origin, can be represented by

$$\mathbf{J}_m^s = i\omega\mu_0 AI\delta(x)\delta(y)\delta(z)\mathbf{x} \qquad (4.67)$$

and

$$\mathbf{J}_m^s = i\omega\mu_0 AI\delta(x)\delta(y)\delta(z)\mathbf{y} \tag{4.68}$$

where AI is the magnetic dipole moment.

The finite-length horizontal electric dipole sources, centered at the origin and extended from $-L/2$ to $L/2$ along the x-axis and the y-axis, can be represented by, respectively,

$$\mathbf{J}_e^s = IL\,B(x)\,\delta(y)\,\delta(z)\,\mathbf{x} \tag{4.69}$$

$$\mathbf{J}_e^s = IL\,\delta(x)\,B(y)\,\delta(z)\,\mathbf{y} \tag{4.70}$$

where $B(x)$ is the box car function defined as

$$B(x) = \begin{cases} 1 & \text{if } |x| \leq \frac{L}{2} \\ 0 & \text{otherwise.} \end{cases} \tag{4.71}$$

Substituting in equations (4.46) to (4.51) and following the same derivation, one comes to (4.60) and (4.63).

4.5 Comparison of the Sensitivities

In this section I compare sensitivities obtained by the approximation method described above (which is the RRI version of CSAMT, and abbreviated CSAMT-RRI) and the perturbation method. The purpose of the comparison is to illustrate when the CSAMT-RRI sensitivities will be valid. The quantities to be compared are $\partial\rho_a/\partial\sigma_i$ and $\partial\phi/\partial\sigma_i$ normalized by the thickness of the perturbed cell, where ρ_a is apparent resistivity, ϕ is phase, and σ_i is the conductivity of the ith cell. The perturbation method requires two forward calculations per cell. $\partial\rho_a/\partial\sigma_i$ and $\partial\phi/\partial\sigma_i$ are calculated with respect to the ith cell of a mesh, which is used in the forward calculation in Chapter 2. In order to compare sensitivities from cells with the same size for CSAMT-RRI and the perturbation method, all observations are located in the region with uniform horizontal node spacing. I compare the sensitivities from these two methods for a

homogeneous half-space, a layered earth, then for a more complicated 2-D model. The sensitivities I compare are those on the co-linear profiles for TE mode due to an HEDx source at $64Hz$.

4.5.1 Homogeneous half-space

To examine sensitivities in the far field, transition zone, and near-field, sensitivities were computed at the four receivers shown in Figure 4.5. TE mode sensitivities on the co-linear profile are shown in Figure 4.6. Note that $\partial\rho_a/\partial\sigma_i$ and $\partial\phi/\partial\sigma_i$ from CSAMT-RRI have been scaled to plot the two sensitivities together, allowing their shapes to be compared. The CSAMT-RRI sensitivity is typically larger than the perturbation sensitivity because of the different volumes perturbed in each case. The perturbation sensitivity is with respect to a cell of finite horizontal width, whereas the CSAMT-RRI sensitivity for this cell is equivalent to perturbing an infinitely wide layer. From Figure 4.6, it can be seen that the CSAMT-RRI and perturbation sensitivities are similar in shape at transmitter-receiver offsets greater than one skin depth. Also note that sensitivities at these offsets decay quickly with depth and are essentially zero below a depth of two skin depths. This indicates that CSAMT data are most sensitive to conductivity structure within two skin depths of the surface. It should be noted that $\partial\rho_a/\partial\sigma_i$ and $\partial\phi/\partial\sigma_i$ have opposite signs. The negative sign of $\partial\rho_a/\partial\sigma_i$ occurs because an increase in the conductivity of the ground produces a lower ρ_a. As in magnetotellurics, a decrease in ρ_a corresponds to phases above 45 degrees and vice versa, so $\partial\phi/\partial\sigma_i$ is positive. At transmitter-receiver offsets less than a skin depth, the shapes of the two sensitivity curves are quite different, suggesting that the approximate sensitivities will not be valid in the near field.

4.5.2 Layered model

The three-layered model and sensitivities are shown in Figure 4.7 for the same receiver locations used in the previous section. $\partial\rho_a/\partial\sigma_i$ and $\partial\phi/\partial\sigma_i$ from CSAMT-RRI

are again scaled for display purposes. Again note that the approximate sensitivities are similar in shape to those from the perturbation method, although they have different magnitudes. From Figure 4.7, it is obvious that the exact sensitivities from the perturbation method are discontinuous at model interfaces, but the approximate CSAMT-RRI sensitivities are continuous. The jumps in the perturbation sensitivities at interfaces of the layered model can be explained by considering the impedances. Although the magnetotelluric impedance in the far field is a continuous function of conductivity and layer thicknesses, its derivative with respect to the conductivity of a layer is not continuous at an interface where the conductivity has a discontinuity. Conversely, the sensitivities from the approximate method are continuous because of the boundary conditions on the horizontal electric fields at an interface. From equation (4.60), the approximate sensitivities are integrals of continuous horizontal electric fields and thus the approximate CSAMT-RRI sensitivities are continuous. Note that at all receivers there is significant sensitivity to the third layer. This is because the skin depth (630 m) in the first layer is much larger than the layer thickness (100 m), and the skin depth (200 m) in the second conductive layer is comparable with its thickness (100 m). Thus energy reaches the third layer and, owing to its low conductivity, diffuses efficiently within it. Note that the sensitivities in the third layer are larger than in the second layer at some sites. This enhanced sensitivity phenomenon is quite different from the results from the half space, where the corresponding sensitivities decrease monotonically with depth. Also note that the sensitivities from the perturbation method in the third layer decay to zero quickly below 1000 m depth, which is about one skin depth (1098 m) in the third layer for 64 Hz. Sensitivities from CSAMT-RRI in the third layer decay to zero at greater depths, because although electromagnetic energy in CSAMT travels horizontally and vertically, formula (4.60) assumes that the energy only travels vertically as in the MT case.

4.5.3 2-D model

The 2-D conductivity model shown in Figure 4.8 was also used to generate synthetic data for the inversion study in next chapter. The model consists of two conductive dipping prisms embedded in a layered earth. The CSAMT-RRI and perturbation sensitivities are shown in Figure 4.9 for three receivers at a frequency of 64 Hz. $\partial\rho_a/\partial\sigma_i$ and $\partial\phi/\partial\sigma_i$ from CSAMT-RRI are again scaled for display. Again, note that the corresponding curves for $\partial\rho_a/\partial\sigma_i$ and $\partial\phi/\partial\sigma_i$ have similar shapes. Also note that $\partial\rho_a/\partial\sigma_i$ at 3600 m and 5600 m are almost the same, but different from that at 4600 m. Since all three receivers are approximately the same number of skin depths from the transmitter, the electrical structures beneath 3600 m and 5600 m are the same, but different beneath 4600 m. Surprisingly, this most complicated model gives the best agreement, partly due to the presence of the conductive overburden which ensures that all three receivers lie in the far-field zone.

4.5.4 Validity of sensitivities

From the above comparisons it can be seen that the corresponding curves for $\partial\rho_a/\partial\sigma_i$ and $\partial\phi/\partial\sigma_i$ from CSAMT-RRI and the perturbation method are broadly similar in shape for each of the three models considered, although they have different magnitudes. Specifically, the ratio of CSAMT-RRI to exact sensitivities is approximately constant for all sites at transmitter-receiver offsets greater than one skin depth. Sensitivities were also computed at other frequencies and similar agreement was obtained. The same agreement was observed for TM mode sensitivities. By comparing CSAMT-RRI sensitivities with those from the perturbation method for various models, it appears that CSAMT-RRI sensitivities are generally a good approximation to the exact sensitivities in the far field and transition zone. The CSAMT-RRI sensitivities may be inaccurate in the near field, where electric currents exhibit zero frequency effects and the fundamental approximation inherent to the method is invalid.
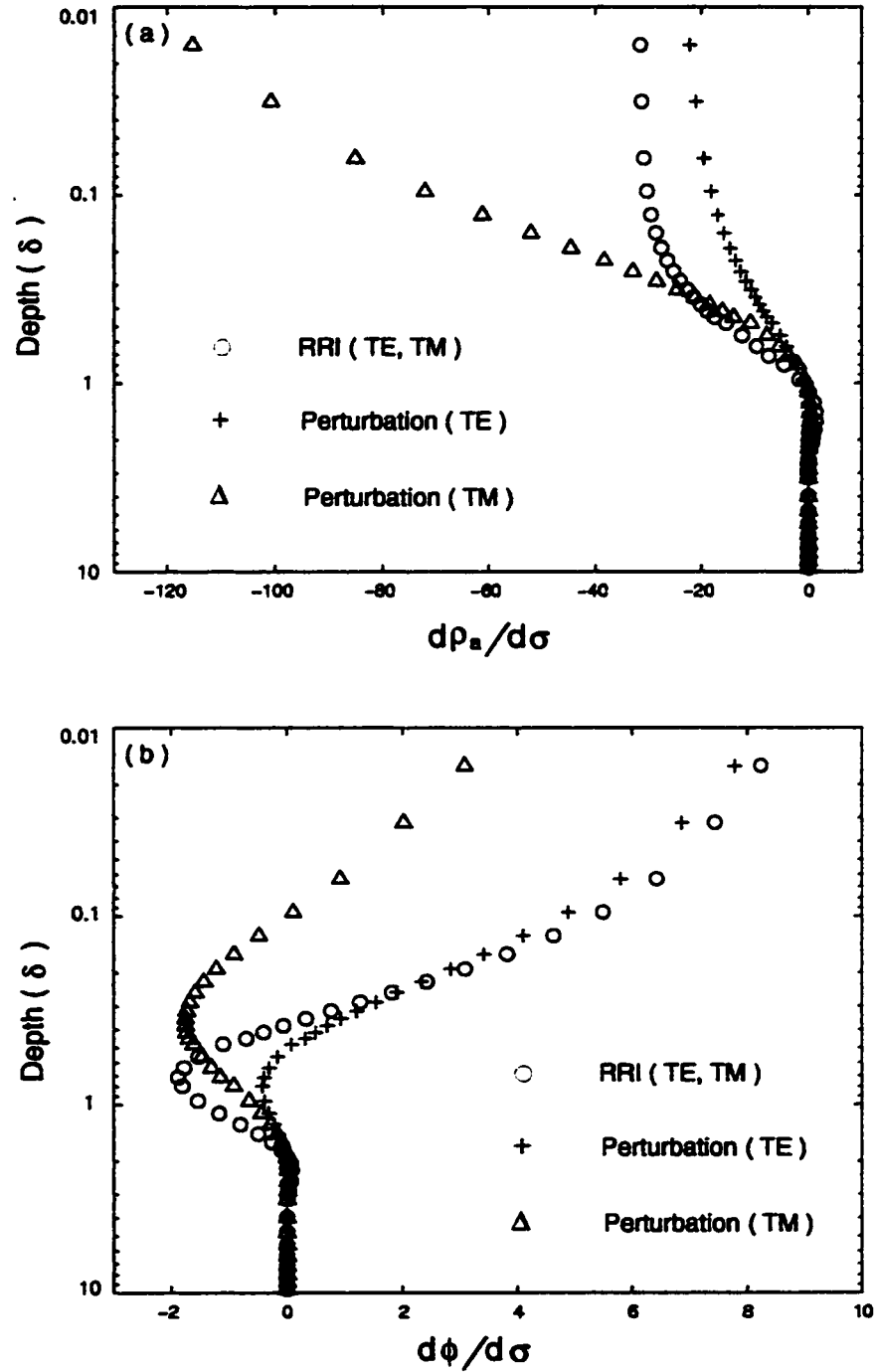
Figure 4.1: Sensitivities normalized by the cell thickness from RRI and the perturbation method for a 100 Ωm half-space at $f = 64Hz$. (a) Sensitivities for apparent resistivity. (b) Sensitivities for phase.
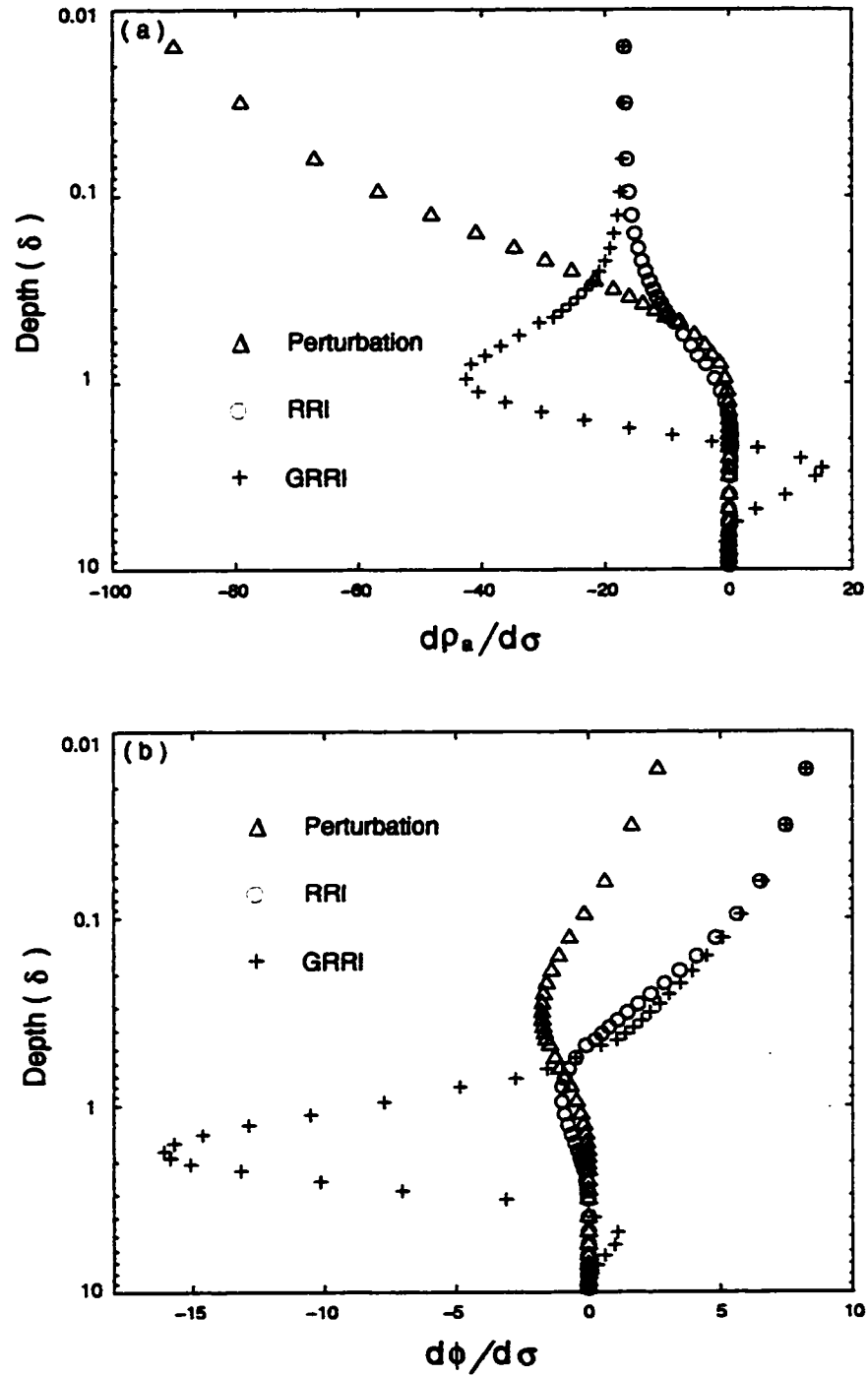
Figure 4.2: Sensitivities of TM data from RRI, GRRI and the perturbation method for the two quarter-space model. (a) Sensitivities for apparent resistivity. (b) Sensitivities for phase.
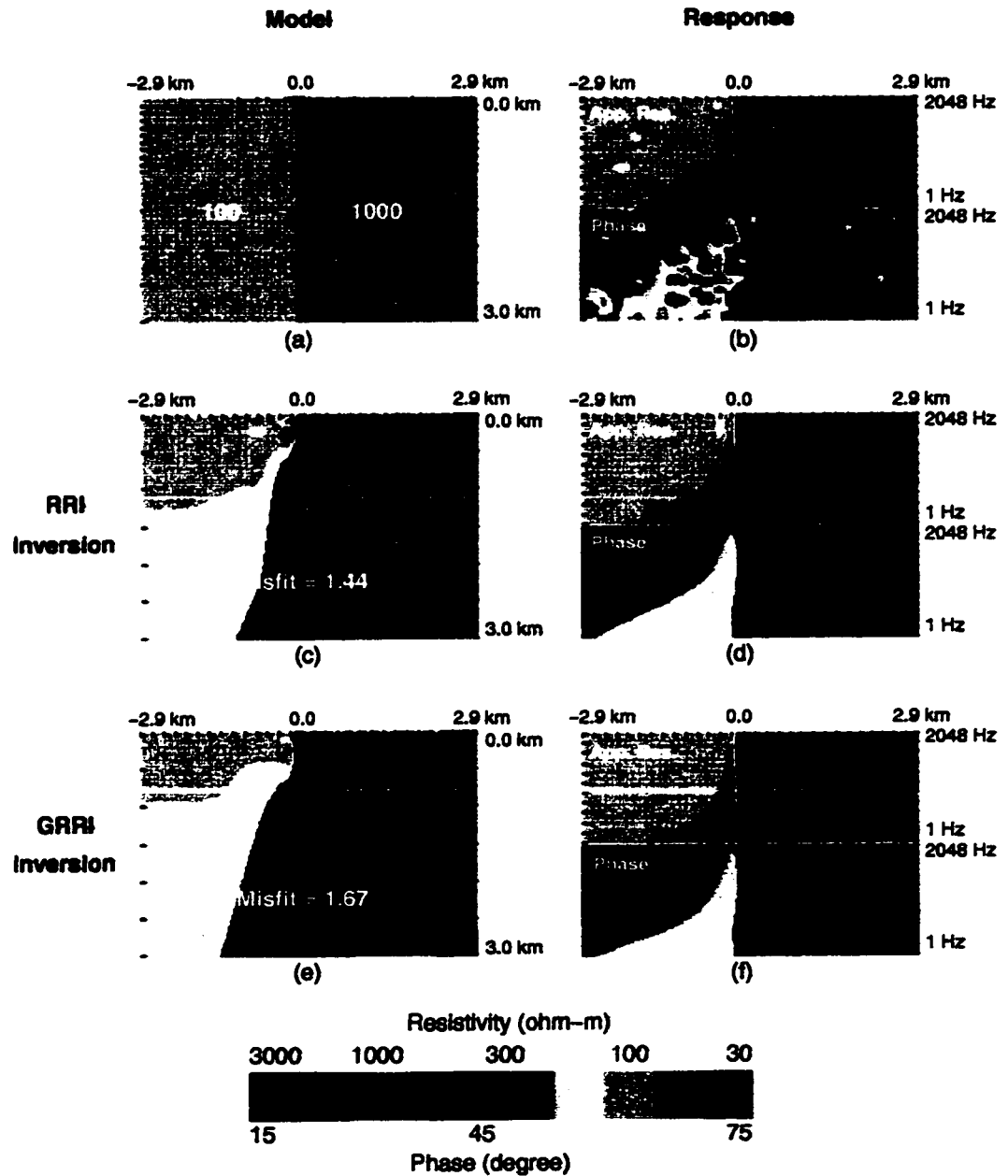
Figure 4.3: Inversions of the two quarter-space model. (a) Resistivity model. (b) Synthetic data for model (a) with 10% Gaussian noise. (c) RRI inversion with a misfit of 1.44. (d) Computed response of model (c). (e) GRRI inversion with a misfit of 1.67. (f) Computed response of model (e).
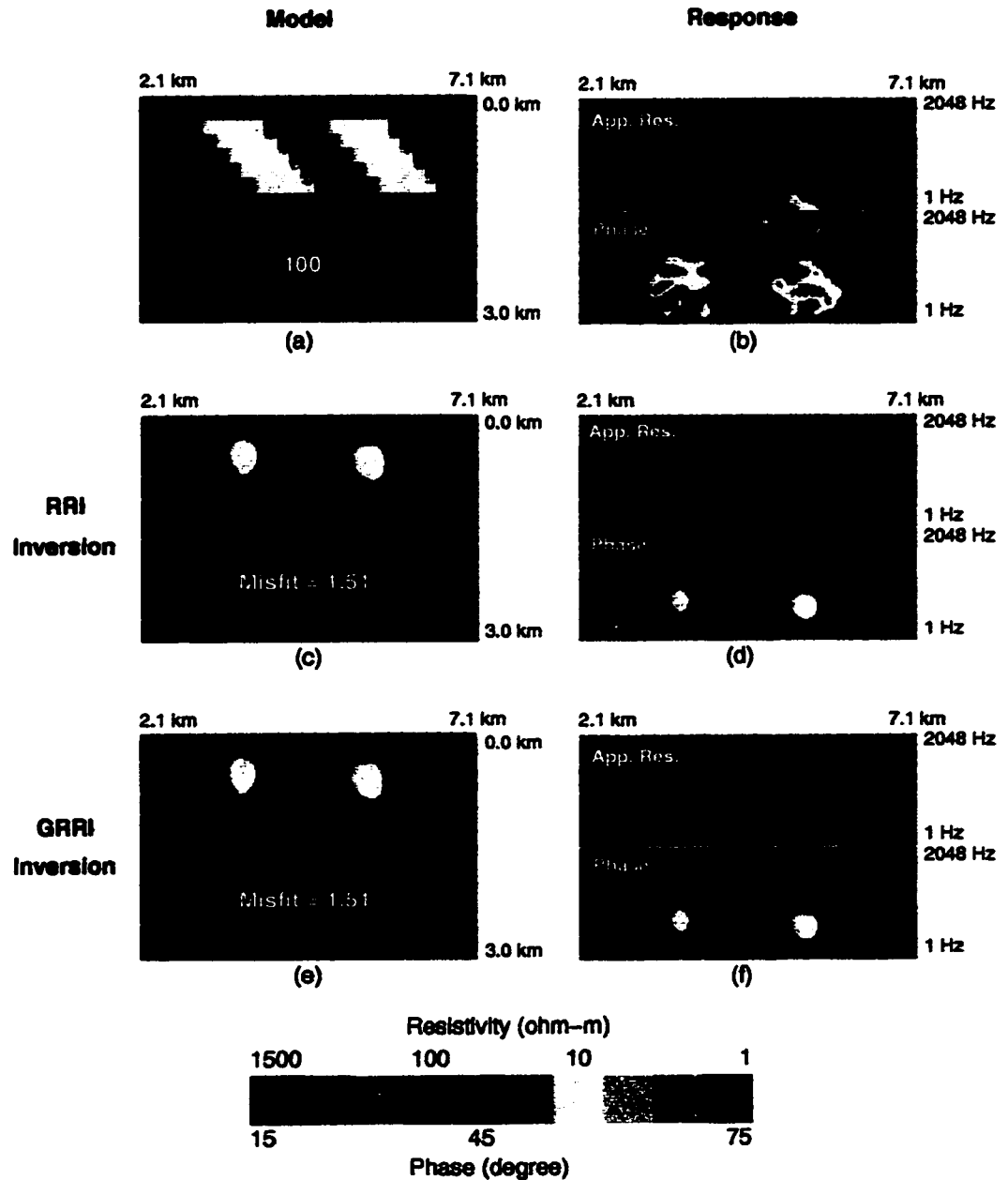
Figure 4.4: Inversions using RRI and GRRI for the two dipping prism model. (a) Resistivity model. (b) Synthetic data for model (a) with 10% Gaussian noise. (c) RRI inversion with a misfit of 1.51. (d) Computed response of model (c). (e) GRRI inversion with a misfit of 1.51. (f) Computed response of model (e).
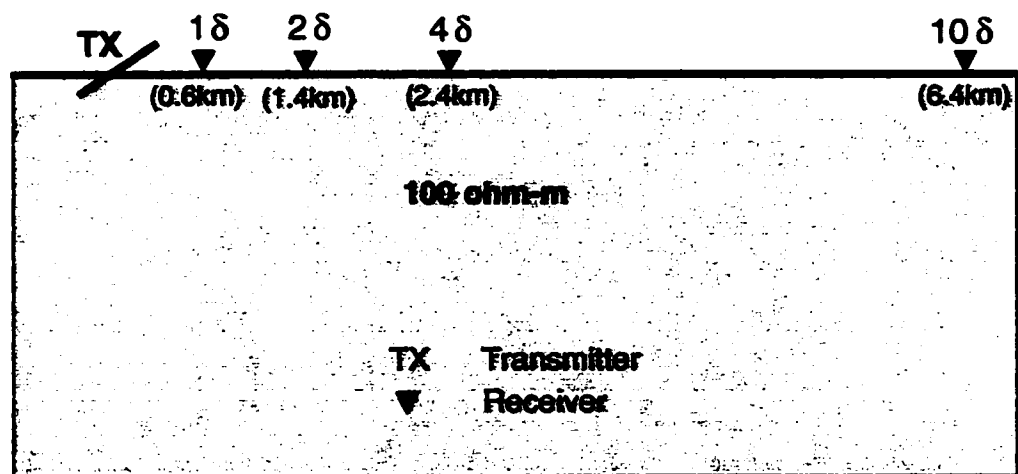
Figure 4.5: Model and receivers for computing sensitivities for the 100 Ωm half-space.
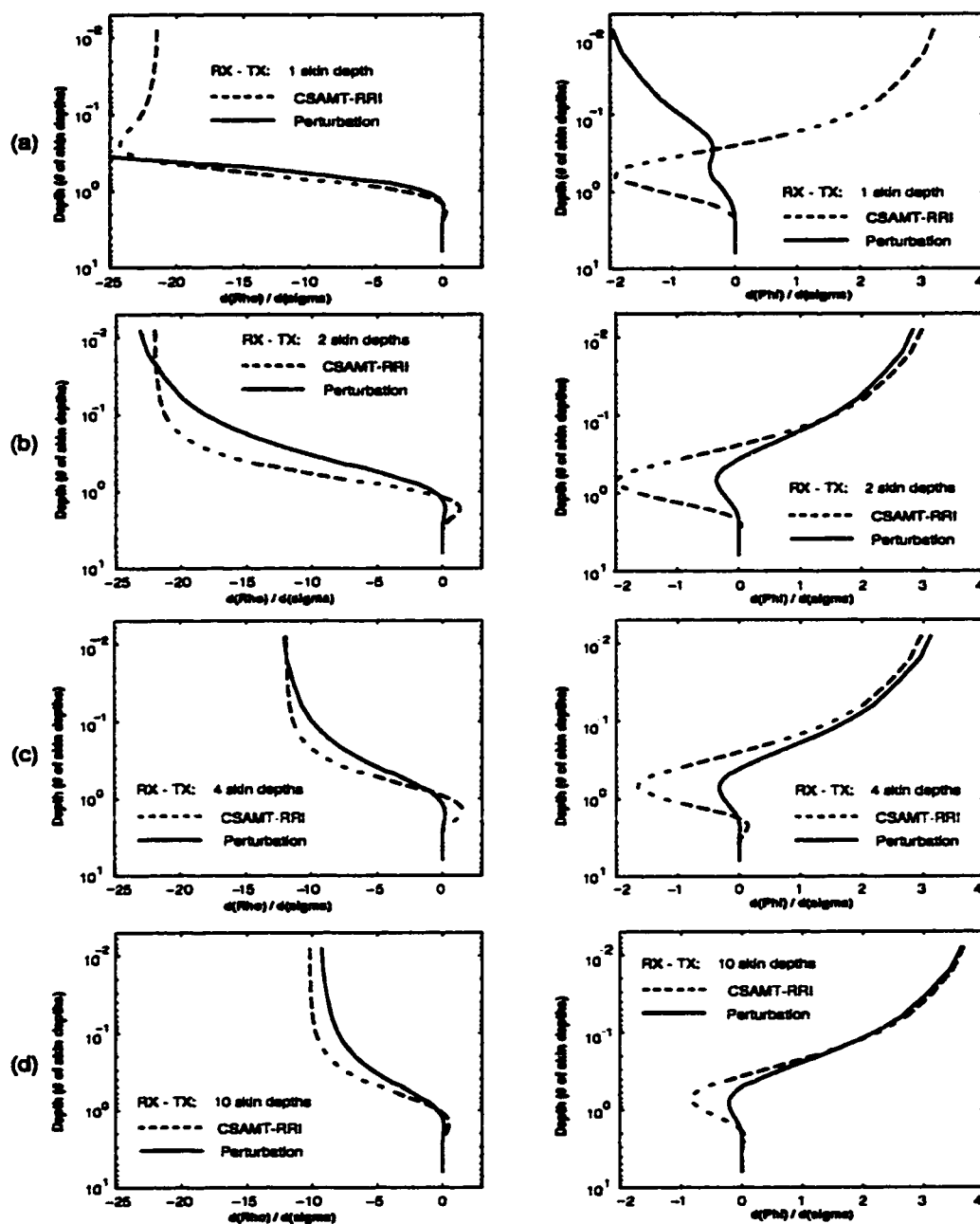
Figure 4.6: Sensitivities for CSAMT-RRI and the perturbation method at receivers over the 100 Ωm half-space. $\partial \rho_a / \partial \sigma_i$ and $\partial \phi / \partial \sigma_i$ from CSAMT-RRI are scaled by 0.31 and 0.43, respectively. Units for $\partial \rho_a / \partial \sigma_i$ and $\partial \phi / \partial \sigma_i$ are m/S^2 and $degree/S$, respectively.
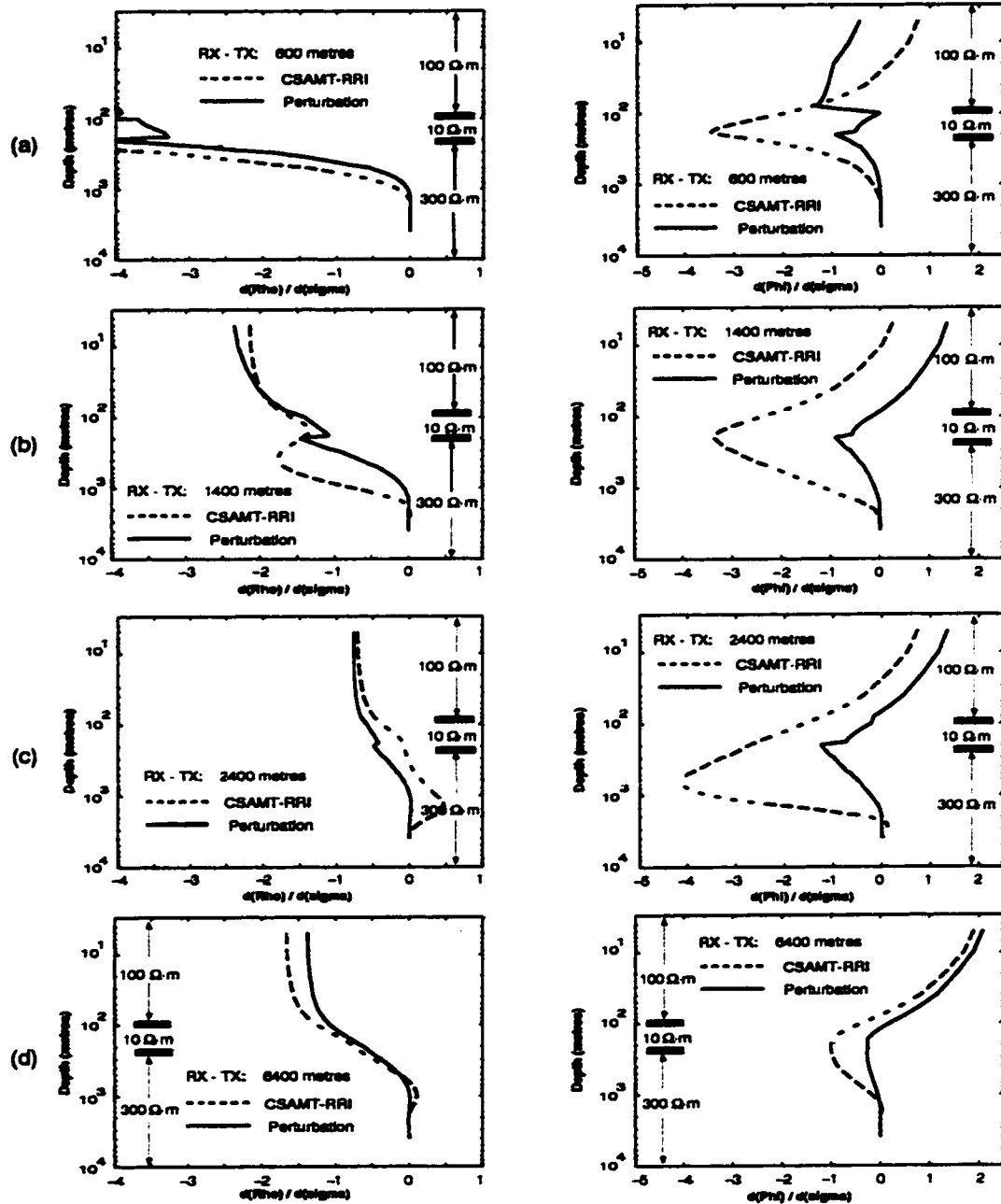
Figure 4.7: Sensitivities for CSAMT-RRI and the perturbation method at various receivers over a three-layer model. $\partial \rho_a/\partial \sigma_i$ and $\partial \phi/\partial \sigma_i$ from CSAMT-RRI are scaled by 0.40 and 0.50, respectively. Refer to Figure 4.6 for units.
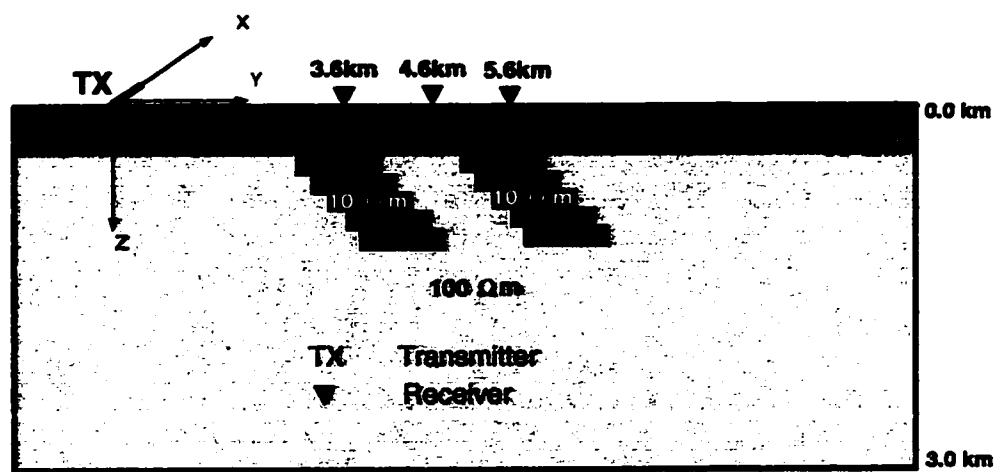
Figure 4.8: Resistivity model and transmitter-receiver geometry used for computing sensitivities of the 2-D model.
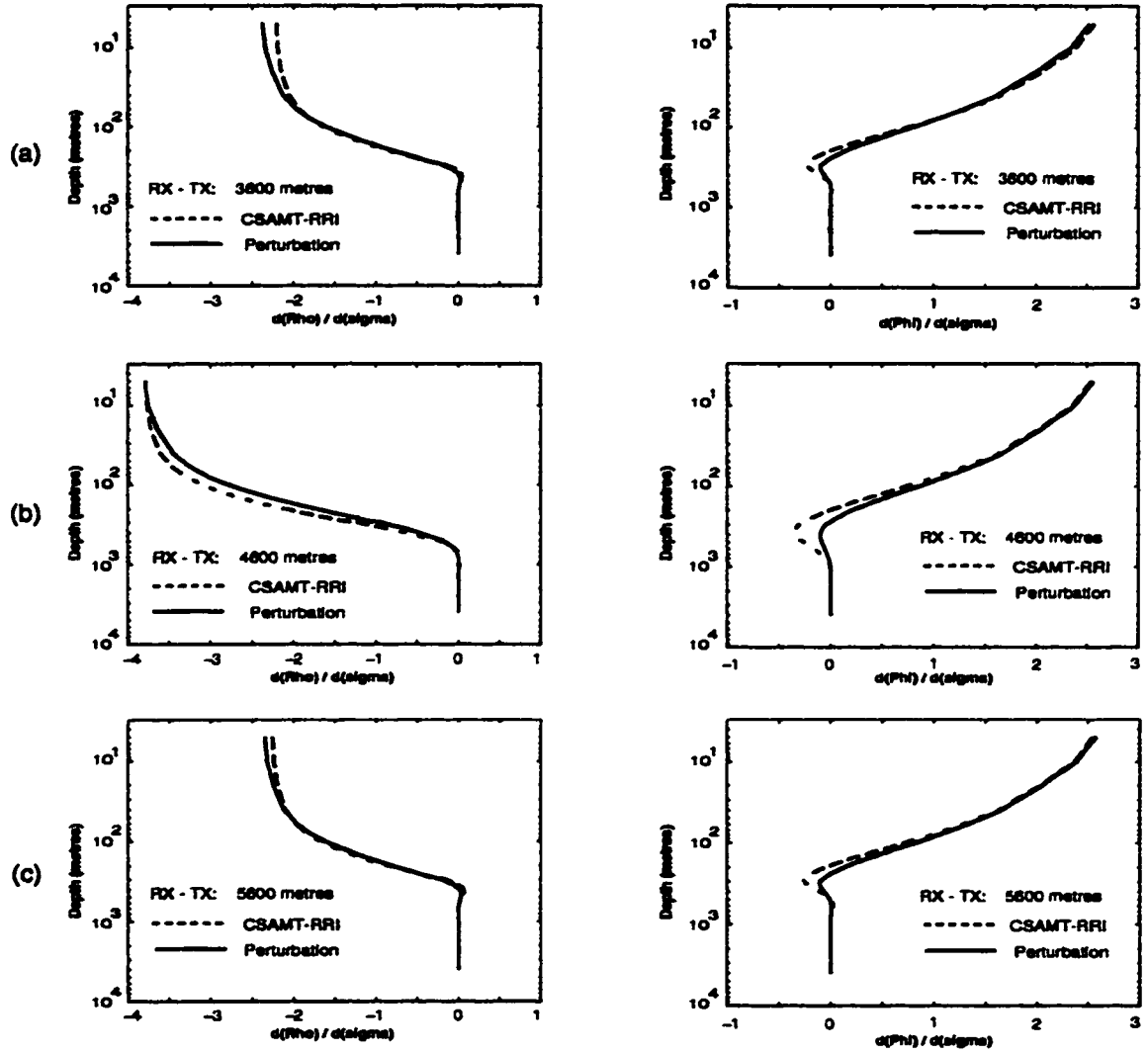
Figure 4.9: Sensitivities for CSAMT-RRI and the perturbation method at various receivers over the 2-D model. $\partial\rho_a/\partial\sigma_i$ and $\partial\phi/\partial\sigma_i$ from CSAMT-RRI are scaled by 0.31 and 0.45, respectively. Refer to Figure 4.6 for units.

Chapter 5

INVERSIONS OF SYNTHETIC DATA AND FIELD DATA

In the previous two chapters, I have extended the RRI inversion algorithm to CSAMT and justified CSAMT-RRI sensitivities on several models. In this chapter, the CSAMT-RRI inversion will be tested on synthetic data, and then applied to field data. Finally, application to CSAMT survey design is discussed.

5.1 Synthetic Data Inversion I: Two Conductive Dipping Prisms

In this section, I present inversions of synthetic data generated from a 2-D model (Figure 4.9) which was described in Section 2.5.1. The two conductive dipping prisms are placed close enough to interact with one another and, by introducing a surface conductive layer, currents are shielded from fully penetrating into the earth, potentially decreasing resolution. All synthetic data used below are obtained from the results in Section 2.5.3 and contaminated with 10% Gaussian distributed noise.

I have tested inversions from different starting models and found that the final result may depend on the starting model. This is not a surprise since linear inversion cannot guarantee to get the global minimum for a nonlinear problem and the inverse problem itself is nonunique. I also observe that inversion will not converge if it is started with a very resistive model. The reason for this is as follows. For a very resistive model, all observation sites would be in the near-field zone, then CSAMT-RRI sensitivities would not be good enough for computing a reasonable model update. In this situation, the inversion can diverge. Normally, inversion converges from a conductive starting model. For MT, Smith and Booker (1991) found that a 1-D min-

imum structure inversion of the horizontally average of the data makes an extremely effective starting model. If using this 1-D MT average model as a starting model for CSAMT, one should be very careful when the source effect is significant in data, because assuming the data are MT can produce a model that is too resistive layer and cause the inversion to diverge. There are several other ways to generate an effective starting model: 2-D MT inversion, 1-D CSAMT inversion, and CSAMT inversion with an infinite line source. However, all inversions presented below were started from a 100 Ωm half-space since my primary goal is to test the algorithm, rather than to interpret specific data.

5.1.1 Inversions of Synthetic HEDx Data

Inversions of HEDx data are shown in Figure 5.1. Figure 5.1(a) shows the inversion results for TE data on the main profile (no offset in strike direction). The inversion reduced rms data misfit from 13.4 for 100 Ωm half-space starting model to 1.5 for the resulting model (5.1(a-3)) after 60 iterations (30 smoothings). The expected rms data misfit is 1.0. The computed response of the resulting model is shown in 5.1(a-2), which indicates an even fit. The conductive overburden and two dipping prisms are resolved. The resolved conductive bodies are located at the correct depth and have approximately the correct resistivity in the upper two thirds of the prisms where the induced currents are the strongest, and also show evidence of the dip of the prisms. The resolved right conductive body spreads deeper and away from the source side. This could be caused by the left conductive prism's "shadow effect" (Kuznetzov, 1982, Zonge and Hughes, 1991), which arises from local features between the source and the sounding site. No extraneous structure appears in the resulting model.

Results from the inversion of TE data on a non-main profile with an offset of 3.0 km in the strike direction are shown in Figure 5.1(b). The data misfit is reduced to 1.8 after 25 iterations (5 smoothings) from an initial 14.2 misfit. Inversion could not reduce misfit further after 25 iterations, although 60 maximum iterations was allowed

(30 smoothings). The computed response is shown in Figure 5.1(b-2). The inversion resolves the conductive overburden and two conductive bodies. The dipping sides are apparent in the inverted result, though their slopes are smaller than the true one. The resistivity of the upper two thirds of the prism is recovered correctly, but smaller than the true resistivity for the lower one third, which has been shielded from the inducing magnetic field by the upper conductive part. Both upper and lower edges appear to be resolved. The inversion results are visually as good as those from the main-profile data, but the measurement of the data might be difficult if a site happens to be in the null zone.

Inversion results for TM data of the non-main profile are shown in Figure 5.1(c), and achieve a reduction in misfit to 1.9 from 13.1 of the uniform half-space starting model after 60 iterations. The conductive overburden and two prisms are resolved separately. The prism at the right hand side is resolved clearly, with correct resistivity and size. Also, its upper and lower edges are located correctly. But the left prism is resolved poorly, with no evidence of dip and is visually much smaller than the actual body. Figure 5.1(c-1) and (c-2), the synthetic data of the true model and the computed response of the inverted model, respectively, show that the inversion does not achieve a good fit for the right-hand anomaly, especially for phase data. The right-hand anomaly is mainly the response from the right-hand dipping prism. Note that source effect is very significant in data, especially in phase data, which might have affected the inversion.

5.1.2 Inversions of Synthetic HEDy Data

For the HEDy source, I inverted TM data from the main profile, and TE and TM data from the non-main profile, respectively. The results of the non-main profile TE data inversion are shown in Figure 5.2(a) after 44 iterations, achieving a data misfit of 2.0, which was reduced from an initial rms misfit of 13.2. The inversion resolves the overburden and two prisms, but the two prisms are recovered poorly. The right-

hand conductive body is bigger in size than the true prism, while the left-hand one is smaller. Both have no evidence that they are dipping. Comparing with the results of TM data on the non-main profile, they are very similar to each other. For both cases, the model progression reveals that the inversion recovers a much bigger conductive body for the right-hand prism than for the left-hand one at the early iterations, and fails to recover them well at later iterations.

Figure 5.2(b) shows the inversion results of TM data on the main profile. The data misfit is reduced to 1.7, after 60 iterations, from an initial 13.7 misfit. Figure 5.2(b-2) and (b-3) show the synthetic response and the resulting model, respectively. The overburden and two prisms are recovered separately. Two recovered conductive bodies have approximately the correct resistivity and are located at the correct depth, but have no indication of dipping.

Results for TM data on the non-main profile is shown in 5.2(c), achieving misfit reduction from 14.6 to 3.2 after 60 iterations. Two conductive bodies are resolved, without evident dipping. The upper edges appear to be located correctly, but the lower edges are extended deeper.

5.1.3 Inversions of Synthetic HMDx Data

Figure 5.3 shows the inversion results for HMDx data. Overall, the inversion results are very similar to those for HEDy due to the similarity of the physics in HEDy and HMDx configuration. Recall the similarity of HEDy and HMDx, mentioned in Section 2.5.

Figure 5.3 (a-2) and (a-3) show the computed response and the recovered model, after 60 iterations, for TE data on the non-main profile, which reduces data misfit to 2.0 from 12.1 of the uniform half-space starting model. Two conductive bodies are barely recovered, the right-hand body with smaller size and the left-hand one with larger size. Neither of them has evidence of dip. The model is very similar to the one (Figure 5.2 (a-3)) inverted from HEDy TE data on the non-main profile.

The inversion model from TM data of the main profile is shown in Figure 5.3 (b-3). Two conductive bodies are resolved, with no evidence of dip. Both are extended in the vertical direction, while the lower edge of the right-hand body is deeper. The corresponding response of the model is shown 5.3 (b-2), with misfit of 1.9, after 60 iterations, from original misfit 11.7. Again, the model similarity can be observed from Figure 5.3 (b-3) and Figure 5.2 (b-3).

Results for TM data of the non-main profile are shown in 5.3 (c), after 44 iterations (30 smoothings), and achieve a reduction in misfit from 13.2 to 4.5. The computed response and the inverted model are shown in 5.3 (c-2) and (c-3), respectively. A conductive body is recovered poorly for the left-hand prism, with much smaller size and higher resistivity than the true model, while the right-hand one is recovered better, with deeper lower edge. No dip is apparent in the inverted model. The null zone might have significant effect on inversion. From the data (Figure 5.3 (c-1)), the response from the left-hand prism is severely distorted by the inaccuracy in the null zone.

5.1.4   Inversions of Synthetic HMDy Data

There exists a similarity between HMDy and HEDx in physics, so their inversion results are very similar to each other for corresponding data sets. Inversion results for HMDy data are shown in Figure 5.4.

The computed response and resulting model from the inversion of TE data on the main profile are shown in Figures 5.4 (a-2) and (a-3). The inversion reduces data misfit to 3.1 from an original misfit of 12.7 for the uniform half-space starting model. The conductive overburden is recovered and two conductive bodies appear to be resolved, though they are not completely separated. The recovered left-hand body has the correct resistivity in the upper two thirds of the body. Its upper edge is resolved clearly, but the lower edge is blurred. Its dip is apparent in the inverted model. For the recovered right-hand body, the correct resistivity is resolved in most of

the body. The upper edge is resolved, but the lower edge is also blurred and extended deeper. No dip appears in the model.

Figures 5.4 (b-2) and (b-3) show the computed response and inverted model from the inversion of TE data on the non-main profile. Data misfit is reduced from 15.9 to 5.0 after 41 iterations. The conductive overburden is recovered. Two conductive bodies are resolved. The left one is recovered as a vertically-stretched body, with the resistivity of 30 Ωm. Its upper and lower edges are not resolved. The right one is resolved as a rectangular body with correct resistivity. The upper edge is resolved, but the lower edges is blurred. Both recovered bodies have no evidence of dipping. The inversion does not recover the model well. The null zone has effected the inversion. Figures 5.4 (b-1) and (b-2) show the data is not fit well, especially phase.

Results from the inversion of TM data on the non-main profile are shown in Figure 5.4 (b). Data misfit is 2.2 after 60 iterations, with the original misfit 11.8 for the uniform half-space starting model. The inverted model is shown in 5.4 (b-3). The overburden and two conductive bodies are recovered. The left conductive body is a 1.0 km × 1.0 km square, with correct resistivity in the center of the body. The right one is a vertically-stretched body, with the volume (about 1.6 km × 2.5 km) of larger than the true prism. The resistivity is recovered in two thirds of the body. Its upper edge appears to be resolved, but the lower edge is blurred and extended deeper than 3.0 km. There is no evidence of dip in the inverted model. Figure 5.4 (b-2), the computed response of the inverted model, shows that the left anomaly in data is not fit as well as the right one, both for apparent resistivity and phase.

5.1.5   Inversions of Synthetic FLHEDx Data

Figure 5.5 shows the inversion results for data from an FLHEDx with the length of 4 skin depths. The results are similar to those from the inversion of HEDx data (5.1). As noted in Section 2.5.3, the FLHEDx data is very similar to the HEDx data. Thus their inversion results are expected to be similar to each other.

Figure 5.5(a) shows the inversion results for TE data on the main profile. The inversion reduced data misfit from 13.4 for the 100 Ωm haf-space starting model to 1.6 for the resulting model (5.5(a-3)) after 32 iterations. The computed response is shown in Figure 5.5(a-2). Compared with the inversion of its corresponding HEDx data, the inversion does not resolve the two conductive bodies separately. Also note that a resistive body appears at the end of the profile near the transmitter.

Figures 5.5(b-3) and (b-2) show the recovered model from TE data on the non-main profile and its computed response. The data misfit is reduced to 1.6 after 60 iterations from an initial 13.8. The conductive overburden and two conductive bodies are resolved. The resolved two conductive bodies are located at the correct depth. The recovered left-hand-side one shows evidence of the dip of the prism, but no evidence is shown from the recovered right one.

Figure 5.5(c-3) shows the resulting model inverted from TM data on the non-main profile. The inversion reduces the data misfit from 13.0 to 2.9 after 60 iterations. The inversion recovered the conductive overburden and the right-hand-side conductive body, but did not resolved the left prism well. Figure 5.5(c-2) and (c-1), the data and the computed response, show that the inversion does not have a good data fit.

5.1.6   Inversions of Synthetic FLHEDy Data

Figure 5.6 shows the inversion results for data from an FLHEDy with the length of 4 skin depths. The results are very similar to those from the inversion of HEDy data (5.2). So the description of inversion results is omitted.

5.1.7   Inversions on joint HEDx TE and HEDy TM data

Figure 5.7 shows the inversion results of joint HEDx TE and HEDy TM data on the main profile. The joint inversion reduces the data misfit to 1.6 after 70 iterations from 10.7 for 100 Ωm half-space starting model. The resistivity model and corresponding computed TE and TM responses from the joint inversion are shown in Figure 5.7(e),

(c) and (d) respectively. The joint inversion recovers a better model than HEDx TE inversion (Figure 5.1 (a-3)) and HEDy TM inversion (Figure 5.1 (b-3)). The inversion separates two conductive bodies clearly and resolves them equally well. The two recovered conductive bodies are located at correct depth and dip.

In summary, all synthetic data inversions presented here for this two conductive dipping prisms model show that the algorithm generally works well, however it obtains better results for some configurations than others. Inversions provide model parameters of the target such as location, size, resistivity and others, but how well those parameters are resolved varies from one data set to another. In data fitting, inversions fit the data on the main profile better than the data on the non-main profile and fit the data without the null zone better than the data affected by the null zone if they are from the same non-main profile. Accordingly, the faithfulness of the recovered model to the true one decreases from the data on the man profile, the data on the non-main profile without the null zone, to the data on the non-main profile with the null zone. TE mode inversion gives evidence of dip, while TM mode inversion separates targets better, but does not have information of dip. Joint inversion results are better than the results of single mode data inversion. Finally, one clarification should be made. The inversion results depend to some extent on initial model and on controlling parameters such as the exact form of $w(x, y)$ and $g(y, z)$ in (3.6). No attempt has been made to optimize these.

5.2 Synthetic Data Inversion II: Two Resistive Dipping Prisms

In the last section, CSAMT-RRI was examined on synthetic data from a conductive 2-D model. In this section, I present inversions of synthetic data generated from a resistive 2-D model (Figure 5.8), which is essentially the same as the one used last section except two dipping prisms are resistive (1000 Ωm). All synthetic data used

below are contaminated with 10% Gaussian distributed noise.

5.2.1 Inversions of Synthetic HEDx TE Data

Figure 5.9 shows the inversion results of HEDx TE data on the main profile. The inversion reduced data misfit from 9.7 to 1.2 after 32 iterations. The inversion resolves the conductive overburden and two resistive prisms. Two resistive prisms are not resolved equally well. The right-hand resistive body approximately has the same size of the true prism, whereas the left hand one is much smaller than the true one, both have no evidence of dip. The inverted model (Figure 5.1 (a-3)) from HEDx TE data on the main profile from the conductive model shows some evidence of dip. This is because conductive bodies, which provide current channels, can be resolved well at deep, whereas resistive bodies at deep are not. The synthetic data (Figure 5.9 (a)) shows that there are almost no anomalies for the left-hand resistive prism in apparent resistivity and phase, and the source effect is very strong close to the transmitter and at low frequencies. Therefore the left-hand resistive body cannot recovered well. Figure 5.9 (b) shows computed responses of the inverted model and indicates a good fit to the data.

5.2.2 Inversions of Synthetic HEDy TM Data

Figure 5.10 shows the inversion results of HEDy TM data on the main profile. The data misfit is reduced to 1.4 from an initial misfit of 10.6 after 22 iterations. Figures 5.10 (b) and (c) show the computed response and the recovered model, respectively. The conductive overburden and two resistive bodies are recovered. The two recovered resistive bodies are separate, have the same size as the true prism, but have no indication of dip. The synthetic data (Figure 5.10 (a)) shows anomalies in apparent resistivity from both resistive dipping prisms are very weak, whereas anomalies in phase from them are clearly visible, but source effect is much stronger in phase than in apparent resistivity.

5.2.3 Inversions of Synthetic HMDx TM Data

Figure 5.11 shows the inversion results of HMDx TM data on the main profile. The inversion reduces the data misfit to 1.7 from an initial misfit of 9.1 after 32 iterations. Figures 5.11 (b) and (c) show the computed response and the recovered model, respectively. The inverted model is very similar to the model from HEDy TM data on the main profile. The conductive overburden and two resistive bodies are recovered. The two recovered resistive bodies are separate, have approximately the same size as the true prism, but have no indication of dip. The synthetic data (Figure 5.11 (a)) shows anomalies in both apparent resistivity and phase from both resistive dipping prisms are visible, while they are stronger in phase than in apparent resistivity.

5.2.4 Inversions of Synthetic HMDy TE Data

Figure 5.12 shows the inversion results of HMDy TE data on the main profile. The data misfit s reduced from 11.6 to 1.5 after 54 iterations. The inversion recovers the conductive overburden and two resistive prisms. The right-hand resistive body has approximately the same size as the true prism, whereas the left hand one is much smaller than the true one. Both have no evidence of dip. The synthetic data (Figure 5.12 (a)) show that anomaly from the left-hand resistive prism in apparent resistivity is very weak, and 10% noise masks the anomaly. Therefore the left-hand resistive body cannot recovered well. Figure 5.9 (b) shows the computed responses of the inverted model.

In summary, all synthetic data inversions presented here are from the main profile for two resistive dipping prisms. Again, all inversions show that the algorithm generally works well. In the sense that we have produced smooth models that fit the data within a reasonably small multiple of the expected misfit. For resistive targets, neither TE nor TM mode inversions provide information about dip. Furthermore, the

TE mode inversion does not resolve the right-hand side resistor as well as the TM mode inversion.

5.3 Examples of Field Data

5.3.1 Sellafield Data

The Sellafield data were collected as part of the search by NIREX (Nuclear Industry Radioactive Waste Executive) to locate an underground facility for the long term storage of intermediate and low level radioactive waste in the United Kingdom. The long term storage of radioactive waste is an unsolved problem for industrial countries. Among potential storage, underground storage is the most-commonly used technique. The requirements for such storage are very high. For instance, such storage should be safe for the life time of 10,000 years. Therefore, extensive site characterization is required to investigate if a proposed site meets the safe requirements. Electrical resistivity is sensitive to the presence of interconnected electrolytic fluids such as water contained in the pores (see Chapter 1). Thus EM methods are important geophysical tools in site characterization. The proposed Sellafield site is very close to the Sellafield Works (Figure 5.13) and intense cultural noise was present. Thus CSAMT is one of the most suitable EM methods to get high quality data. For more information about the project, previous geological and geophysical studies of Sellafield site, one is referred to papers by Chaplow (1996) and Unsworth et al (1998).

Sites with high quality data were grouped into 4 profiles as shown in Figure 5.13. Figure 5.13 also shows the geological frame work and borehole locations. The transmitter is approximately parallel to the regional geological strike, and the four profiles are almost perpendicular to the transmitter. Only TE mode data were collected at these sites. The purpose of the field data examples is to demonstrate the applicability of the developed algorithm to real data sets. Thus I take Line 1 (the principal survey line) as a field data example of HEDx TE data. The results of other three lines are

not presented in this dissertation, but are described by Unsworth *et al.*, (1998).

Line 1 passed through the proposed storage site and consists of 18 sites, which are located from 1.6 *km* to 7.7 *km* away from the transmitter. Four boreholes (BH-1, BH-10, BH-4 and BH-8) are located close to Line 1. These boreholes give independent electrical resistivity data for comparison with results inverted from CSAMT data. Figure 5.14(a) shows the TE data collected along Line 1. Note the high resistivities that occur close to the transmitter and which move to lower frequencies as transmitter-receiver offset increases. There are two possible causes for this phenomenon. One could be due to the source effect. The other could be the presence of a resistive structure under the transmitter that deepens to the west. It is important to determine how much of the high apparent resistivity derives from geoelectric structure and how much is due to the source effect.

The data were inverted starting from 100 Ωm half-space using the CSAMT-RRI algorithm. After 43 iterations the data misfit was reduced from 11.3 to 1.7, with the expected misfit of 1.0. Figure 5.14(b) and (c) show the model response and the final resistivity model. BH-1, BH-10, BH-4 and BH-8 are projected on the profile (Figure 5.14(c)). The comparison between the inverted resistivity model and the well log data is shown in Figure 5.14(d), which shows they are in good agreement generally. CSAMT inversion gives a smooth change in resistivity with depth. This is because we seek the smoothest model to overcome the nonuniqueness of the inversion. At the potential storage site, BH-4 and the inversion results agree well. Both show low resistivity of the sedimentary rocks at shallow depth, then a resistivity rise at the depth of 400 m representing the Borrowdale volcanic group. Further to the east at BH-8 this agreement is also observed, but there is some discrepancy below 500 m. At the area near the coast, BH-1 and the inversion model both show a conductor at depth from 500 m to 1000 m, which is denoted by Unsworth *et al.* (1998) as the coastal conductor due to an intrusion of hypersaline fluids. Further inshore, good agreement can be observed between the inversion model and BH-10, which is in the transition

zone from the saline zone at the west to the fresh water zone at the east. The principal mapped faults are also shown in the resistivity model (Figure 5.14(c)). A coincidence can be observed between the main geological structure and the resistivity model.

In summary, CSAMT successfully recovers the subsurface electric resistivity structure in the site characterization of radioactive waste disposal. Comparison of the inverted resistivity model with well log data shows generally good agreement. This shows that CSAMT-RRI correctly recovered resistivity model and we should have confidence in using this inversion technique.

5.3.2 Salt Dome Data

The interpretation of this data set is very brief because of the confidential nature of the project. The data were collected during oil and gas exploration. The primary objective of the CSAMT survey is to delineate the structure of a salt dome. Some other geophysical surveys were carried out before the CSAMT survey. A seismic survey defined the salt body as a steep-sided diaper in cross-section and elbow-shaped in plan view. Time domain EM (TDEM) preceded CSAMT data acquisition in order to get the background resistivity values important to CSAMT transmitter-receiver separation considerations. TDEM data also were used in the static shift correction of CSAMT data. The survey consisted of two profiles transversing the salt body. The interpretation of one of the two profiles, Line A (Figure 5.15), is presented as an example. Figure 5.15 shows the survey geometry of Line A. Power lines and pipelines are present in the survey area and some of them transverse the two profiles. Data at some sites and frequencies are severely contaminated and eliminated. Figure 5.16(a-1) and 5.16(a-2) show TE and TM data of Line A, respectively. Note that the TM data of the three middle sites are very different from those of their neighbor sites, which are caused by a gas pipeline passing through at the middle site of these three sites and are excluded in inversion.

From Figure 5.16(a-1) and 5.16(a-2) also note that there is no obvious source

effect. Therefore, I first invert TE and TM data with MT inversion. The resulting model clearly recovered a resistive body at the right side of the profile and has a data misfit of 1.5. But 2.5-D CSAMT forward modeling shows that the MT model fits the data at a misfit of 8.9. Obviously, the data is not fit well in the CSAMT context. This shows that even though the data appear to have no obvious source effect and can be fit well with MT inversion, the resulting model is still questionable in the sense of data fit in the CSAMT context. CSAMT inversions with various starting models are performed on the data. Experiments show that the inversion starting with the model from the MT inversion results in the model with smallest data misfit of 2.6 of all tests. Figure 5.16(c) shows the CSAMT inversion model with the smallest data misfit. The shallow structure above 500 m of this survey area is very simple. It basically consists of two layers, an upper resistive layer and a lower conductive layer. At the left end of the profile, a layered earth is recovered. This agrees with the results from TDEM. A resistive body, the salt body, is recovered with the resistivity of 50 Ωm at the right hand side half of the profile. The resolved salt body has its center located between the sixth and seventh sites from the right, the upper and lower edges located at the depths of 500 m and 2100 m. Although we have no other information to verify the model, CSAMT inversion does recover a resistive body and fits the data fairly well (5.16(b-1) and 5.16(b-2)).

5.4 Application to Survey Design

My synthetic data inversions of a conductive model and a resistive model provide several suggestions for designing a CSAMT survey.

5.4.1 Transmitter

Physically, HED and HMD are equivalent. Therefore, HED and HMD should resolve targets equally well, theoretically. The appearance of the EM field of an HED at the

surface of the earth is similar to that of the EM field of an HMD (see Figures 2.4 and 2.6). However, if both an HED and an HMD have a unit dipole moment, the EM field of an HED is about 2 orders of magnitude stronger than an HMD EM field. Also, an HED transmitter can be made to have larger dipole moment than an HMD transmitter. Thus using an HED can enhance signal to noise ratio (SNR), improve data quality and investigate deeper. In practice, therefore HED could possibly get better results because of its quality data. However, an HMD transmitter is safer than an HED, which has two grounded electrodes.

For a specific transmitter, particular configurations can have higher SNR than others. For the same transmitter, signals are stronger on the main profile than on non-main profiles, but only one mode can be measured on the main profile (TE for HEDx and HMDy, TM for HEDy and HMDx). Null zone can appear for one mode on a non-main profile (TE for HEDx and HMDy, TM for HEDy and HMDx). SNR is extremely low close to the null zone for those modes. For different transmitters, for example, HEDx and HEDy, HEDx has stronger signals than HEDy on the main profile; HEDx TM and HEDy TE have the same signal strength on the same non-main profile, whereas HEDx TE and HEDy TM measurements could go into the null zone. Those comments are also hold for HMDy and HMDx if HMDx and HMDy are substituted for HEDy and HEDx.

In practice, a real CSAMT electric source is an FLHED. When the length of an FLHED is less than 2-3 skin depths, an FLHED can be approximated by an HED with about 5% error in apparent resistivity and phase in most areas except close to the null zone. Appearances of the EM field, apparent resistivity and phase of an FLHED are more complicated than those of an HED. The conditions used to define the near-field, transition zone and far-field in Chapter 2 are still suitable for an FLHED. Specifically, the far-field of an FLHED is the region which is 3-5 skin depths away from the electrodes and the straight line between the two electrodes.

5.4.2   TE, TM modes

If investigated targets are conductors, TE mode data possibly resolve more structure details such as dip than TM mode data, whereas TM data possibly separate two adjacent conductors better than TE data. If investigated targets are resistors, TM data can resolve the model better than TE data since TE data cannot recover geometry such as dip of a resistive model.

For transmitters HEDx (similarly, FLHEDx), HEDy (FLHEDy), HMDx, and HMDy, in a 2-D environment, only one mode can be measured on the main profile. But on non-main profiles, both modes can be measured. Normally, a survey should be designed to collect data on the main profile to avoid the null zone on non-main profiles, at which data are not accurate.

Inversion of single mode data can provide general informations about the target such as approximate location, resistivity, size etc, but those parameters are not constrainted well. If a survey aims to reveal finer informations of targets, measurement of both modes is strongly recommended since joint inversion provides better results than each individual inversion. This implies that if only one transmitter is used, survey profiles should be off the main profile whenever possible.

5.4.3   Data quality

Figure 5.17 shows the inversion results of HMDy TE data with 3%, 10% and 20% Gaussian noise. The model is the same as the one of synthetic HMDy TE data example in Section 5.2. The inversion results deteriorate as data has more noise. Inversion of data with 3% noise recovered two connected resistive bodies, whereas inversion of data with 20% noise only recovered the right-hand resistive body, but it is much smaller than the true one. Tests on other models also shows that inversion resolution degrades as noise increases. Therefore, the quality of data is very important to inversion.
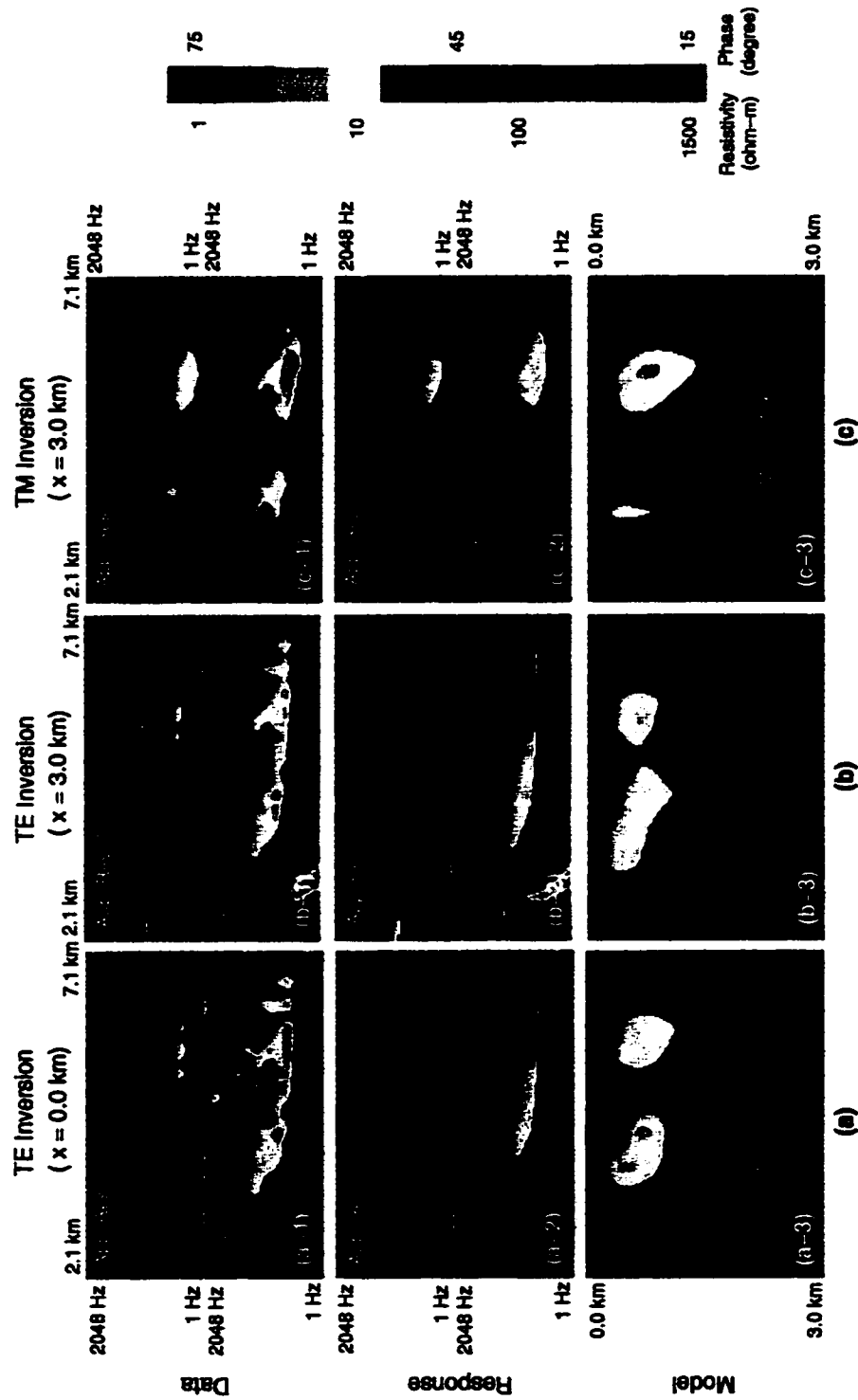
Figure 5.1: Inversion results for HEDx data. (a) Inversion of HEDx TE data on the main profile. (a-1) HEDx TE synthetic data (x=0.0 km) with 10% Gaussian noise. (a-2) Computed response of inversion model (a-3). (a-3) Resistivity model inverted from data (a-1). (b) Inversion of HEDx TE data on a non-main profile. (b-1) HEDx TE synthetic data (x=3.0 km) with 10% Gaussian noise. (b-2) Computed response of inversion model (b-3). (b-3) Resistivity model inverted from data (b-1). (c) Inversion of HEDx TM data on the non-main profile. (c-1) HEDx TM synthetic data (x=3.0 km) with 10% Gaussian noise. (c-2) Computed response of inverted model (c-3). (c-3) Resistivity model inverted from data (c-1).

128
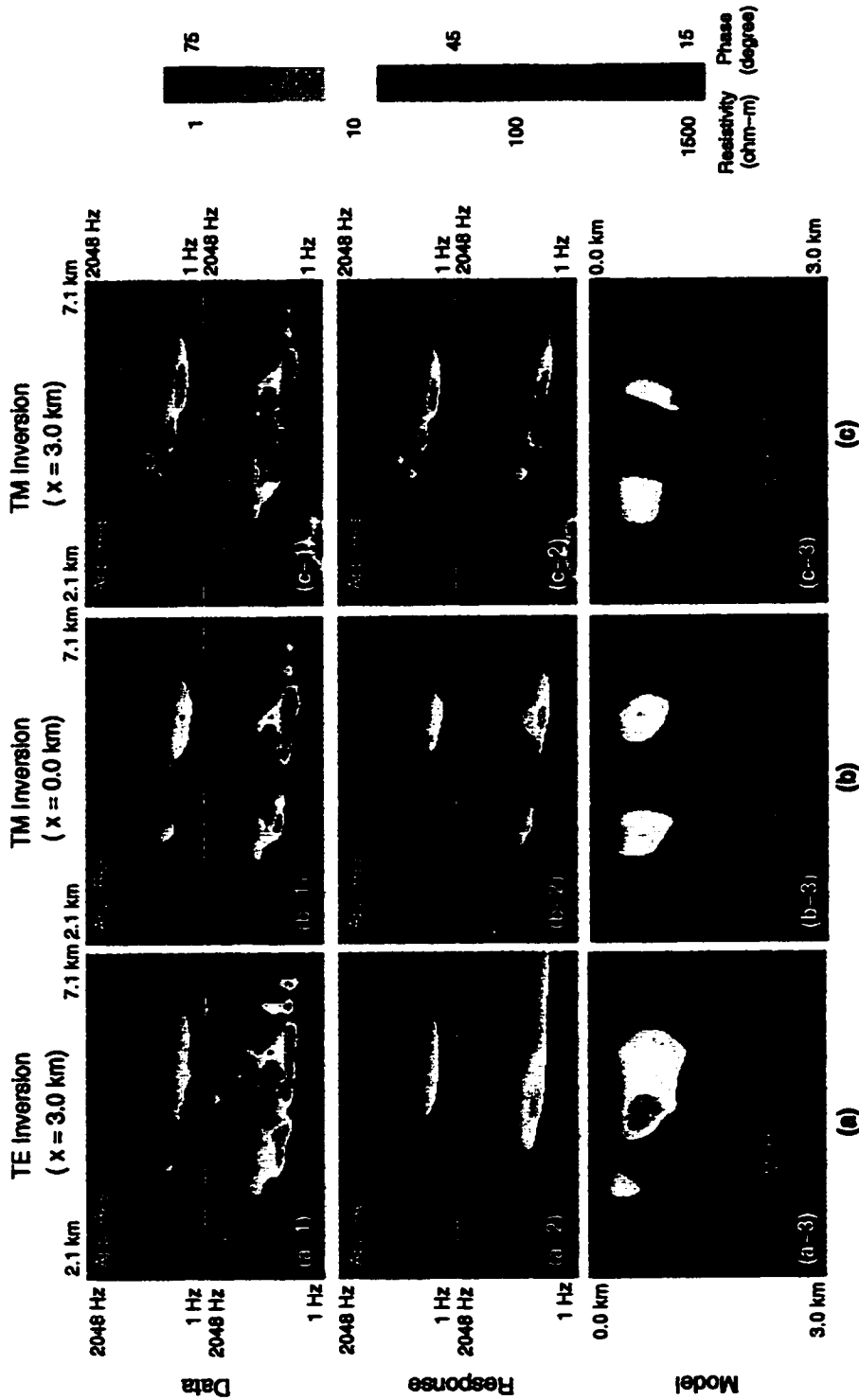
Figure 5.2: Inversion results for HEDy data. (a) Inversion of HEDy TE data on the non-main profile. (a-1) HEDy TE synthetic data (x=3.0 km) with 10% Gaussian noise. (a-2) Computed response of inversion model (a-3). (a-3) Resistivity model inverted from data (a-1). (b) Inversion of HEDy TM data on the main profile. (b-1) HEDy TM synthetic data (x=0.0 km) with 10% Gaussian noise. (b-2) Computed response of inversion model (b-3). (b-3) Resistivity model inverted from data (b-1). (c) Inversion of HEDy TM data on the non-main profile. (c-1) HEDy TM synthetic data (x=3.0 km) with 10% Gaussian noise. (c-2) Computed response of inverted model (c-3). (c-3) Resistivity model inverted from data (c-1).
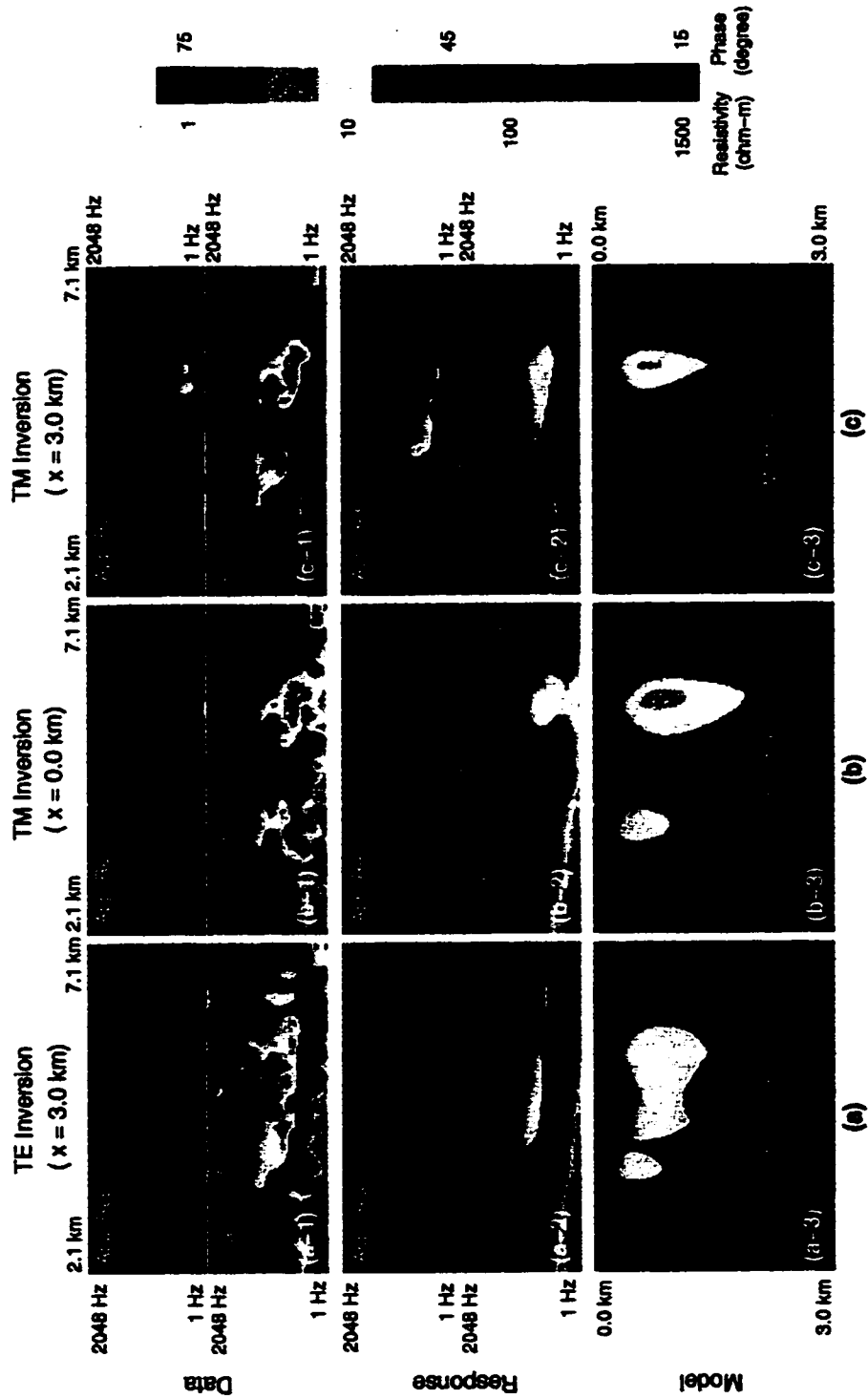
Figure 5.3: Inversion results for HMDx data. (a) Inversion of HMDx TE data on the non-main profile. (a-1) HMDx TE synthetic data (x=3.0 km) with 10% Gaussian noise. (a-2) Computed response of inversion model (a-3). (a-3) Resistivity model inverted from data (a-1). (b) Inversion of HMDx TM data on the main profile. (b-1) HMDx TM synthetic data (x=0.0 km) with 10% Gaussian noise. (b-2) Computed response of inversion model (b-3). (b-3) Resistivity model inverted from data (b-1). (c) Inversion of HMDx TM data on the non-main profile. (c-1) HMDx TM synthetic data (x=3.0 km) with 10% Gaussian noise. (c-2) Computed response of inverted model (c-3). (c-3) Resistivity model inverted from data (c-1).
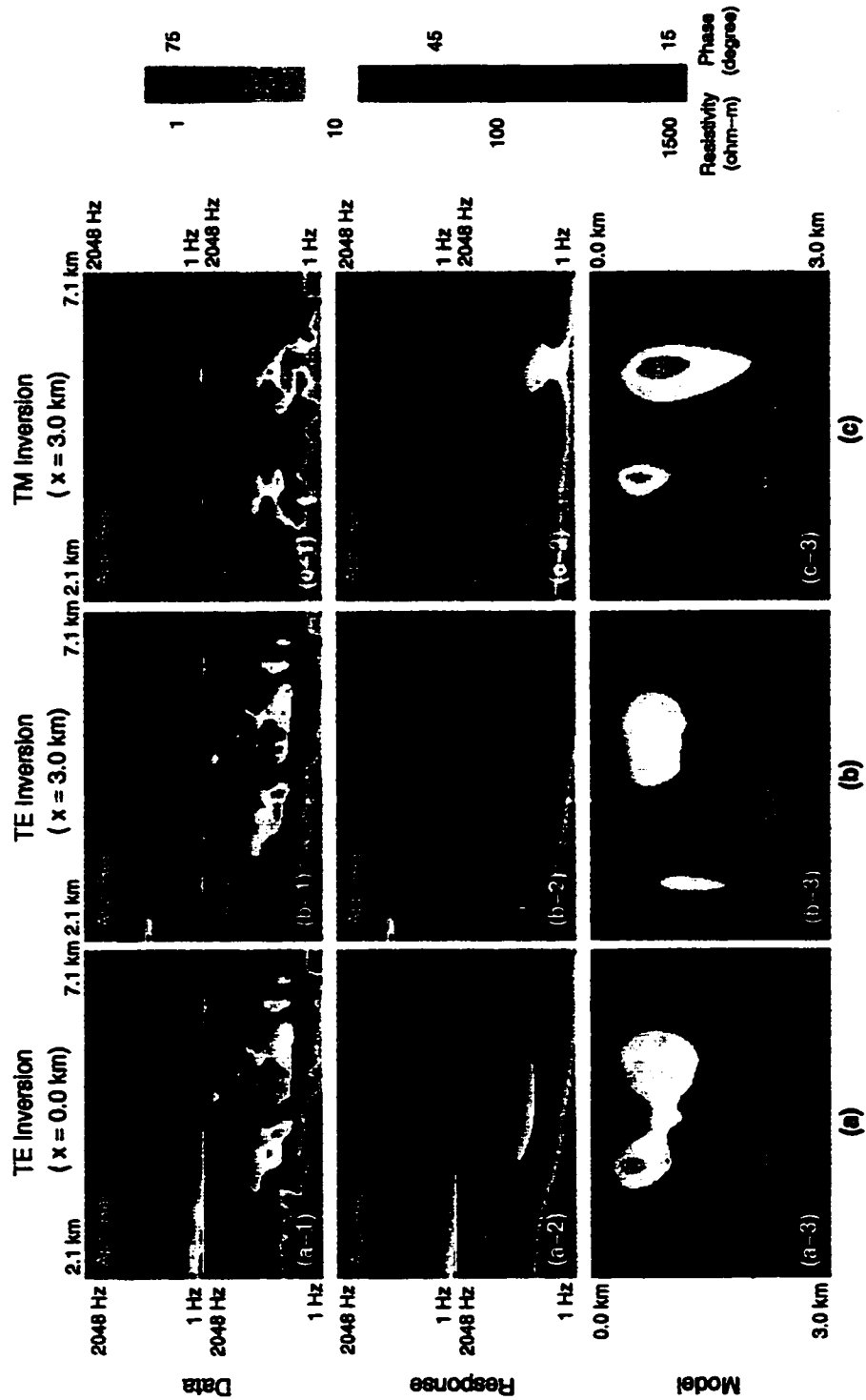
Figure 5.4: Inversion results for HMDy data. (a) Inversion of HMDy TE data on the main profile. (a-1) HMDy TE synthetic data (x=0.0 km) with 10% Gaussian noise. (a-2) Computed response of inversion model (a-3). (a-3) Resistivity model inverted from data (a-1). (b) Inversion of HMDy TE data on the non-main profile. (b-1) HMDy TE synthetic data (x=3.0 km) with 10% Gaussian noise. (b-2) Computed response of inversion model (b-3). (b-3) Resistivity model inverted from data (b-1). (c) Inversion of HMDy TM data on the non-main profile. (c-1) HMDy TM synthetic data (x=3.0 km) with 10% Gaussian noise. (c-2) Computed response of inverted model (c-3). (c-3) Resistivity model inverted from data (c-1).

130
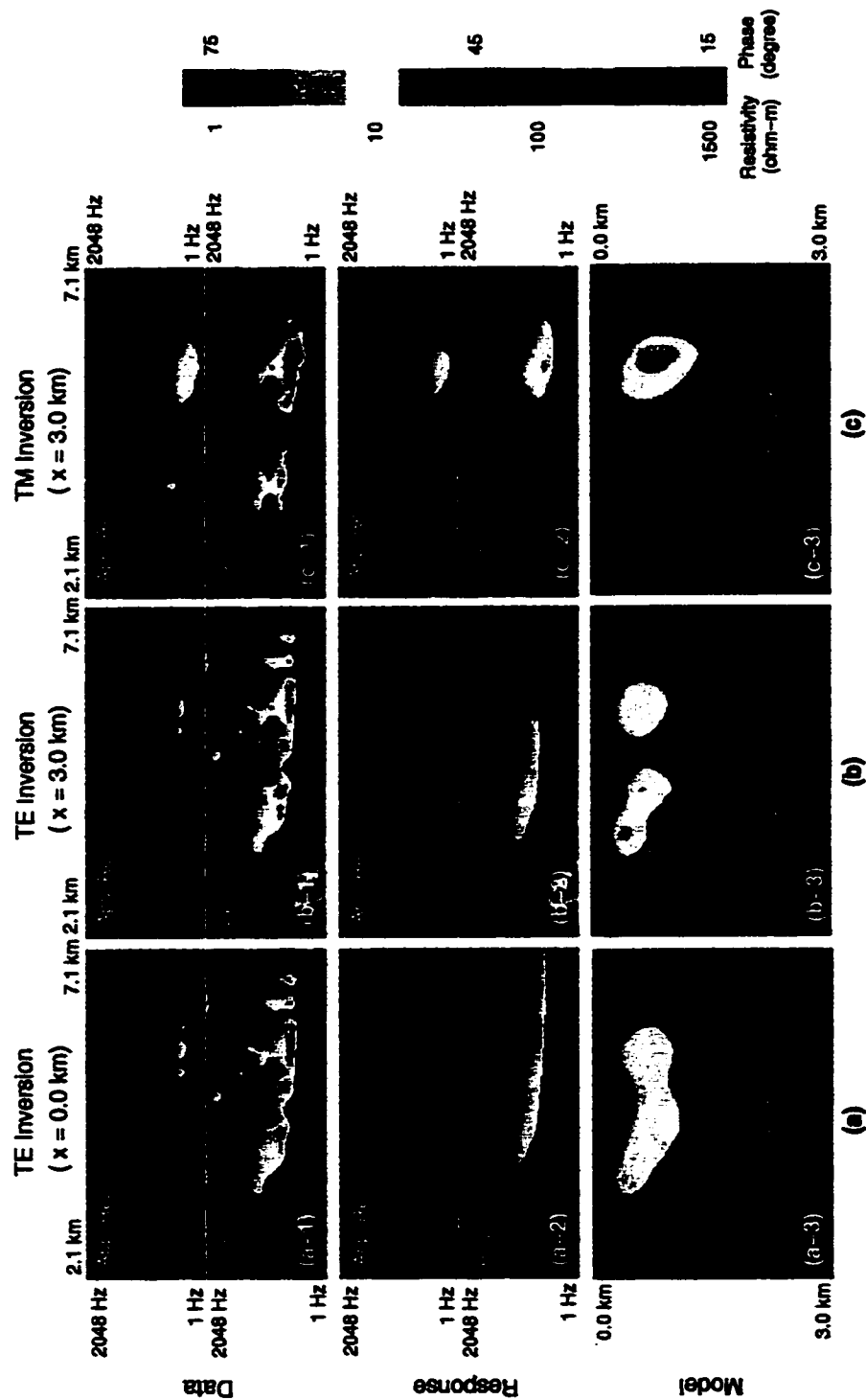
Figure 5.5: Inversion results for FLHEDx data. (a) Inversion of FLHEDx TE data on the main profile. (a-1) FLHEDx TE synthetic data (x=0.0 km) with 10% Gaussian noise. (a-2) Computed response of inversion model (a-3). (a-3) Resistivity model inverted from data (a-1). (b) Inversion of FLHEDx TE data on the non-main profile. (b-1) FLHEDx TE synthetic data (x=3.0 km) with 10% Gaussian noise. (b-2) Computed response of inversion model (b-3). (b-3) Resistivity model inverted from data (b-1). (c) Inversion of FLHEDx TM data on the non-main profile. (c-1) FLHEDx TM synthetic data (x=3.0 km) with 10% Gaussian noise. (c-2) Computed response of inverted model (c-3). (c-3) Resistivity model inverted from data (c-1).

132
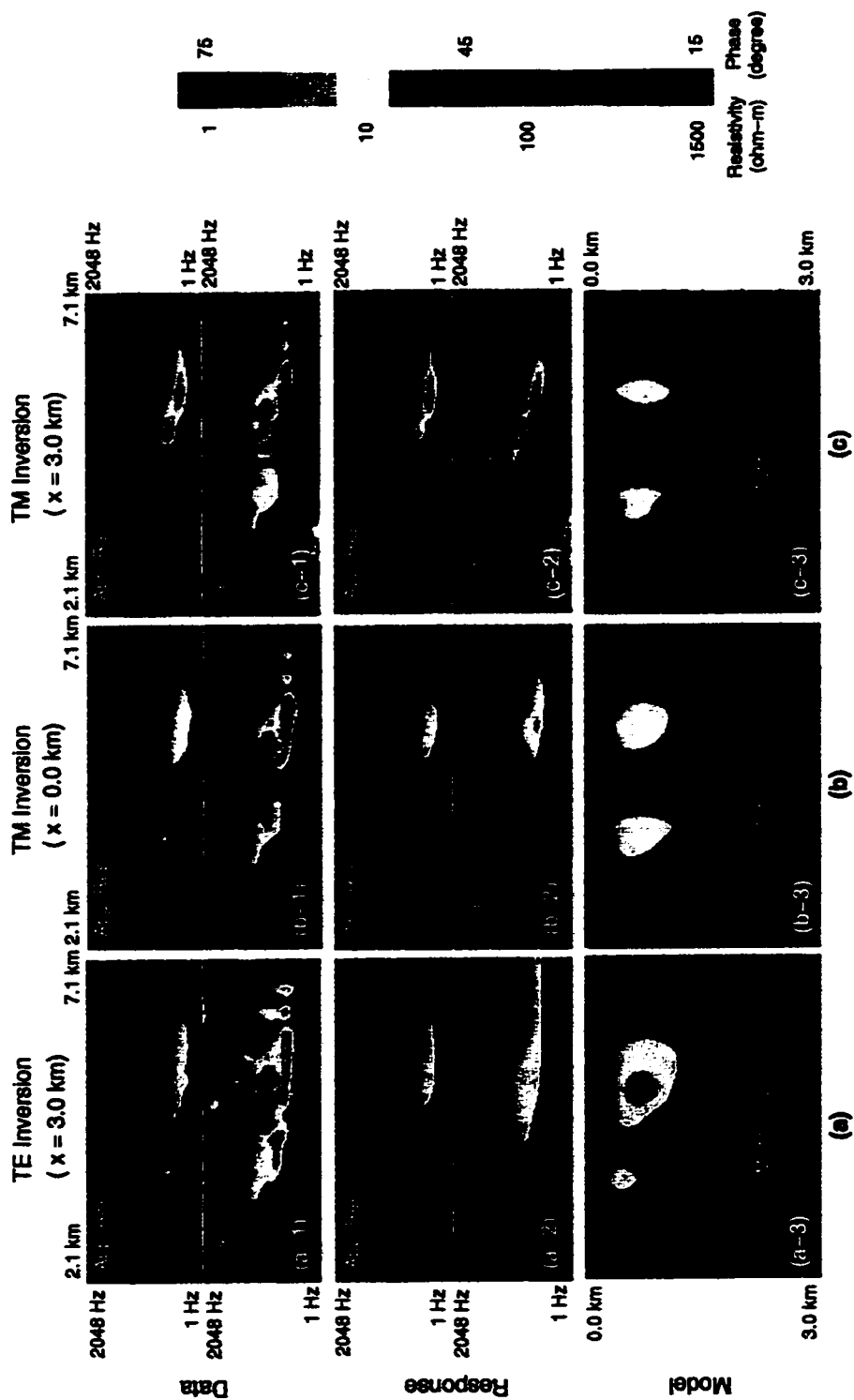
Figure 5.6: Inversion results for FLHEDy data. (a) Inversion of FLHEDy TE data on the non-main profile. (a-1) FLHEDy TE synthetic data (x=3.0 km) with 10% Gaussian noise. (a-2) Computed response of inversion model (a-3). (a-3) Resistivity model inverted from data (a-1). (b) Inversion of FLHEDy TM data on the main profile. (b-1) FLHEDy TM synthetic data (x=0.0 km) with 10% Gaussian noise. (b-2) Computed response of inversion model (b-3). (b-3) Resistivity model inverted from data (b-1). (c) Inversion of FLHEDy TM data on the non-main profile. (c-1) FLHEDy TM synthetic data (x=3.0 km) with 10% Gaussian noise. (c-2) Computed response of inverted model (c-3). (c-3) Resistivity model inverted from data (c-1).

HEDx TE
(x =0.0 km)
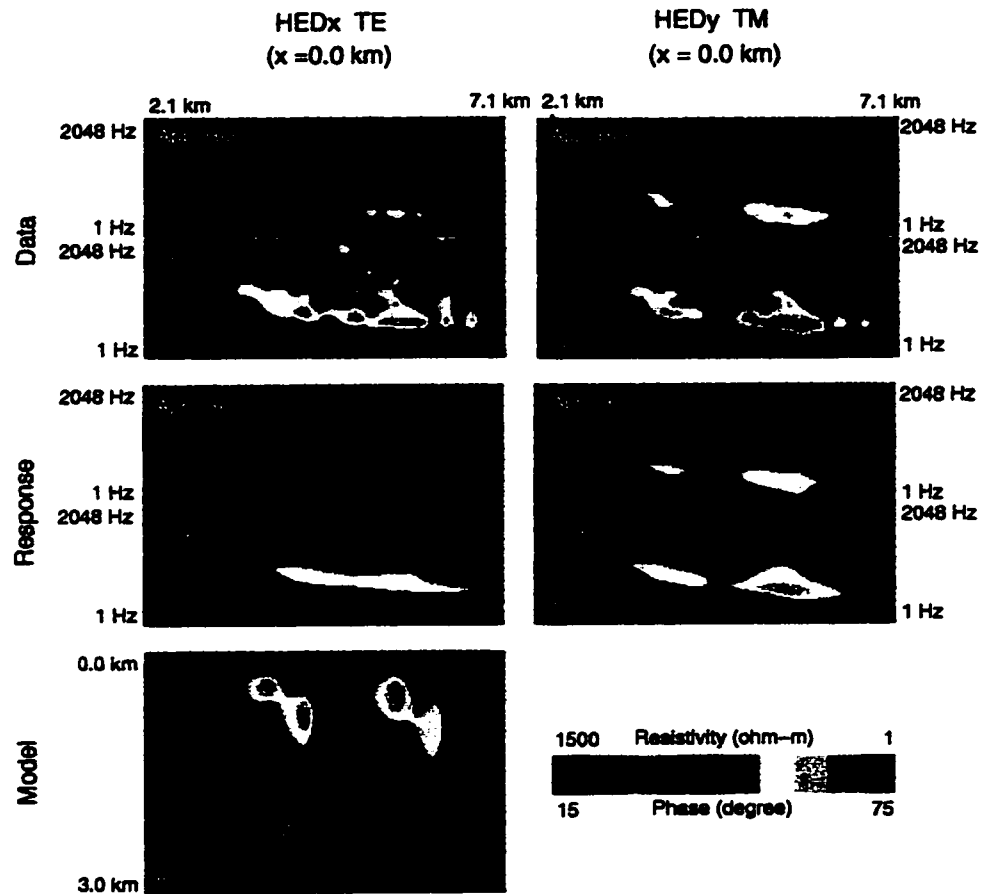
HEDy TM
(x = 0.0 km)

Figure 5.7: Joint inversion of HEDx TE data and HEDy TM data. (a) HEDx TE data on the main profile withe 10% Gaussian noise. (b) HEDy TM data on the main profile withe 10% Gaussian noise. (c) Computed TE response for inverted model (e). (d) Computed TM response for model (e). (e) Joint inversion model.

2.1 km   **7.1 km**
0.0 km

3.0 km

1500   100   10   1

Resistivity (ohm–m)
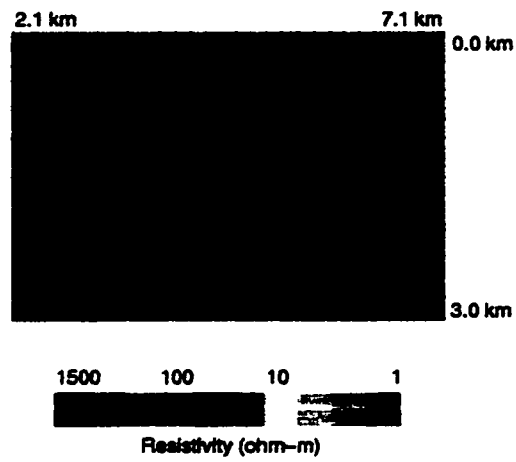
Figure 5.8: 2-D resistive model. Two resistive dipping prisms (1000 Ωm) embedded in a homogeneous bedrock (100 Ωm) with a conductive overburden.

HEDx TE Data Inversion
(x = 0.0 km)

2.1 km   7.1 km

2048 Hz

Data

1 Hz
2048 Hz

(a)   1 Hz

2048 Hz

Response

1 Hz
2048 Hz

(b)   1 Hz

0.0 km

Model

(c)   3.0 km

1500   Resistivity (ohm-m)   1

15   Phase (degree)   75
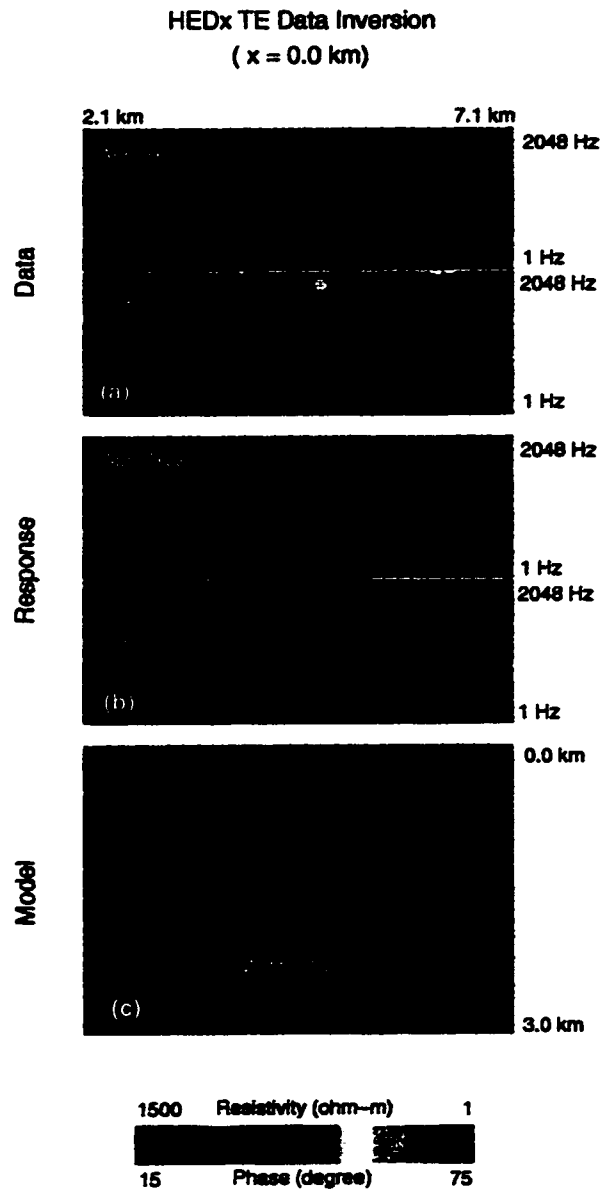
Figure 5.9: Inversion results for HEDx TE data for the resistive 2-D model. (a) HEDx TE data on the main profile with 10% Gaussian noise. (b) Computed response for inverted model (c). (c) Resistivity model inverted for data (a).

HEDy TM Data Inversion
(x = 0.0 km)

2.1 km   7.1 km

2048 Hz

Data

1 Hz
2048 Hz

1 Hz

2048 Hz

Response

1 Hz
2048 Hz

1 Hz

0.0 km

Model

3.0 km

1500   Resistivity (ohm-m)   1

15   Phase (degree)   75
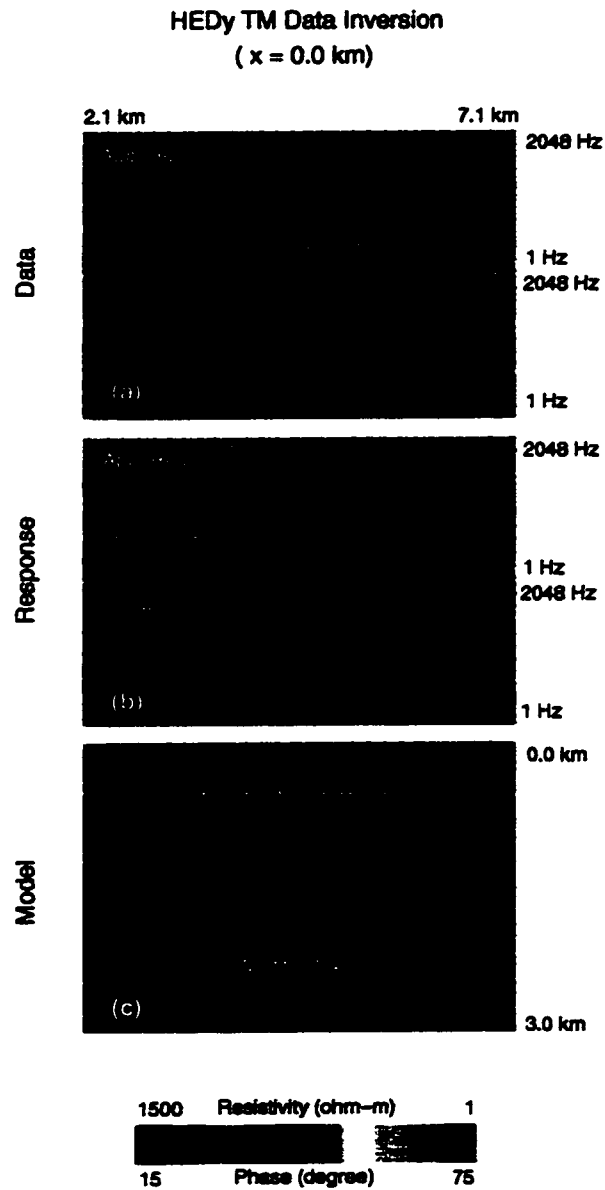
Figure 5.10: Inversion results for HEDy TM data for the resistive 2-D model. (a) HEDy TM data on the main profile with 10% Gaussian noise. (b) Computed response for inverted model (c). (c) Resistivity model inverted for data (a).

HMDx TM Data Inversion
(x = 0.0 km)
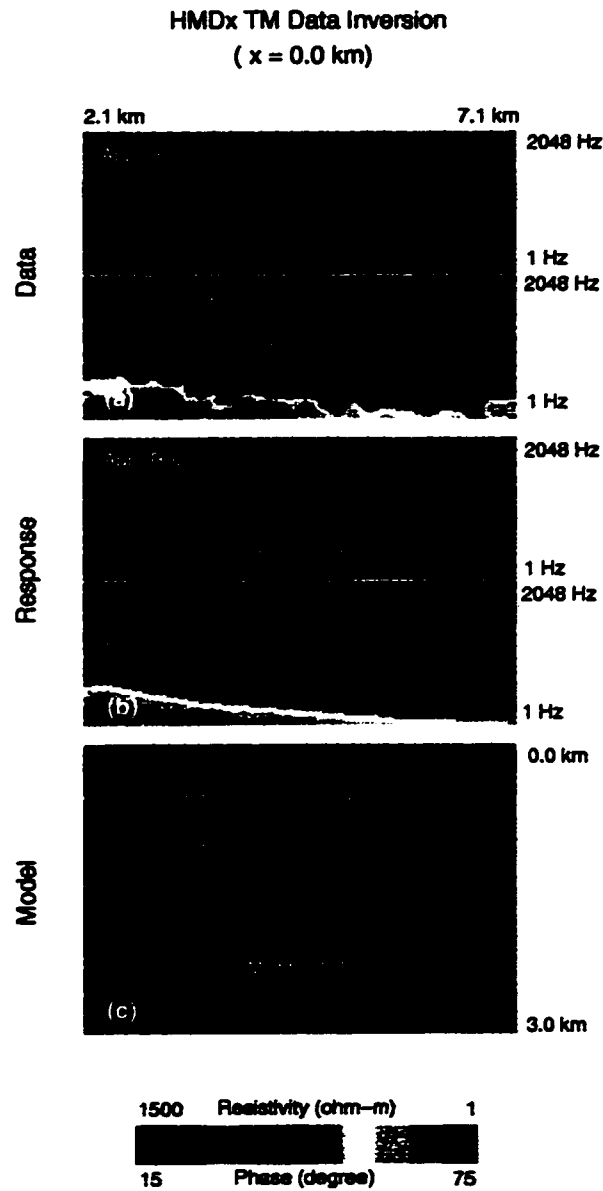
Figure 5.11: Inversion results for HMDx TM data for the resistive 2-D model. (a) HMDx TM data on the main profile with 10% Gaussian noise. (b) Computed response for inverted model (c). (c) Resistivity model inverted for data (a).

HMDy TE Data Inversion
(x = 0.0 km)
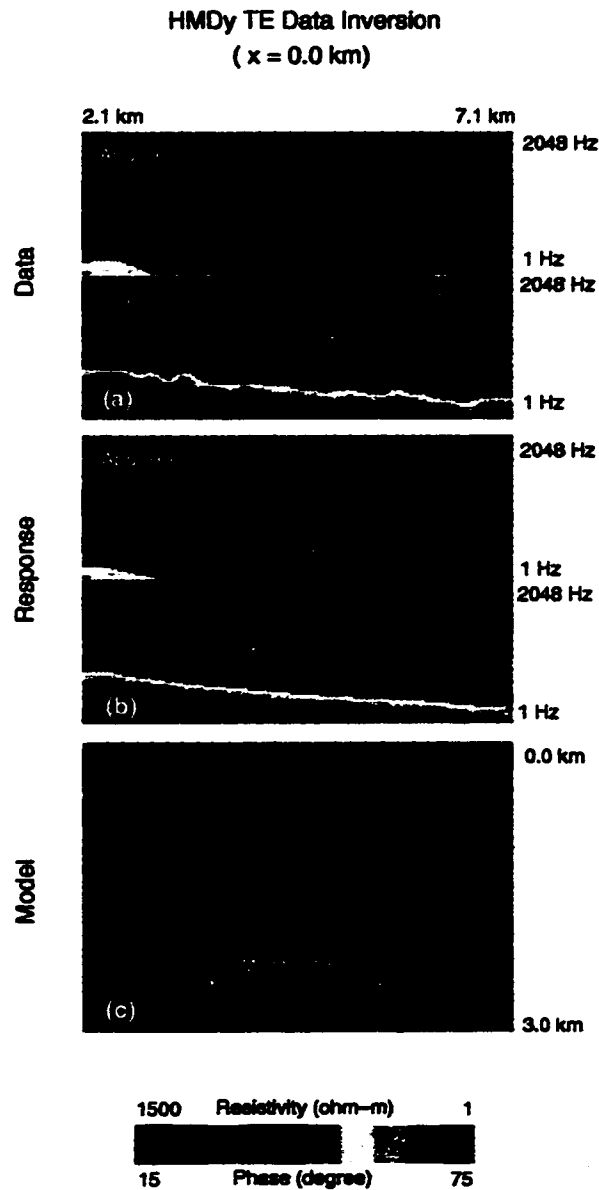
Figure 5.12: Inversion results for HMDy TE data for the resistive 2-D model. (a)
HMDy TE data on the main profile with 10% Gaussian noise. (b) Computed response
for inverted model (c). (c) Resistivity model inverted for data (a).
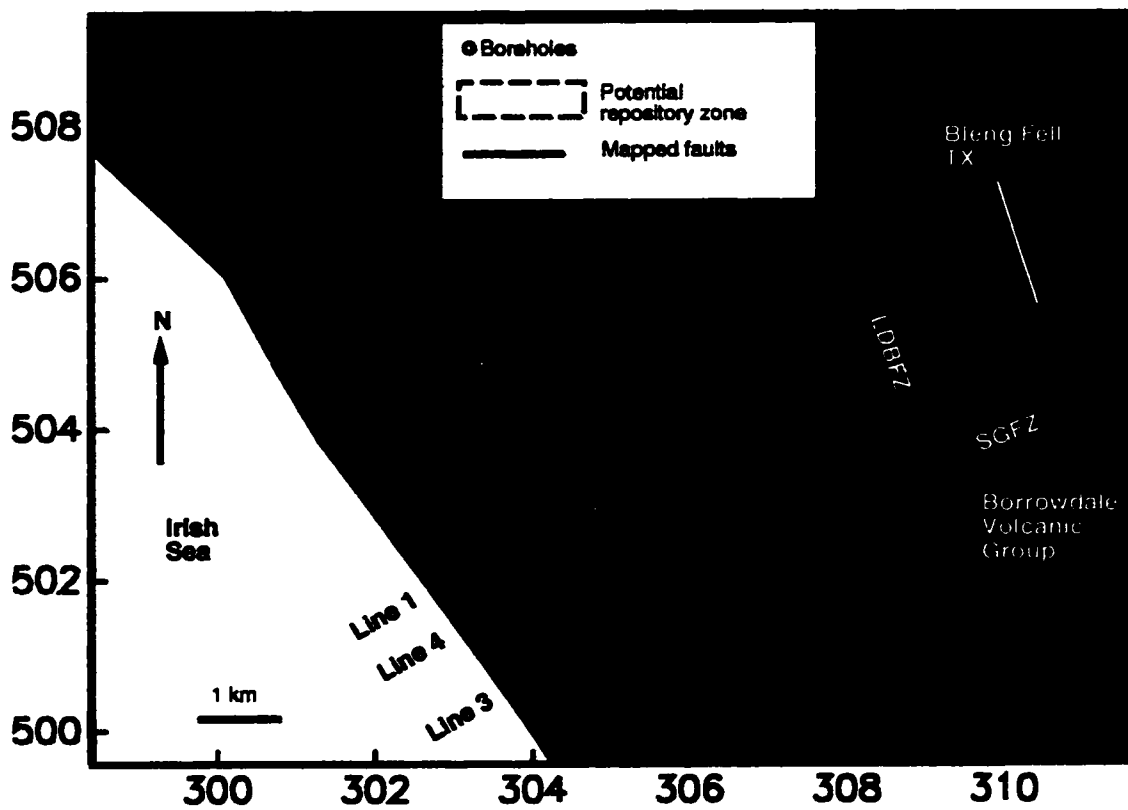
Figure 5.13: Map of the Sellafield survey area and the CSAMT layout. LDBFZ: Lake District Boundary Fault Zone. SGFZ: Seascale Gosforth Fault Zone. FHFZ: Fleming Hall Fault Zone.
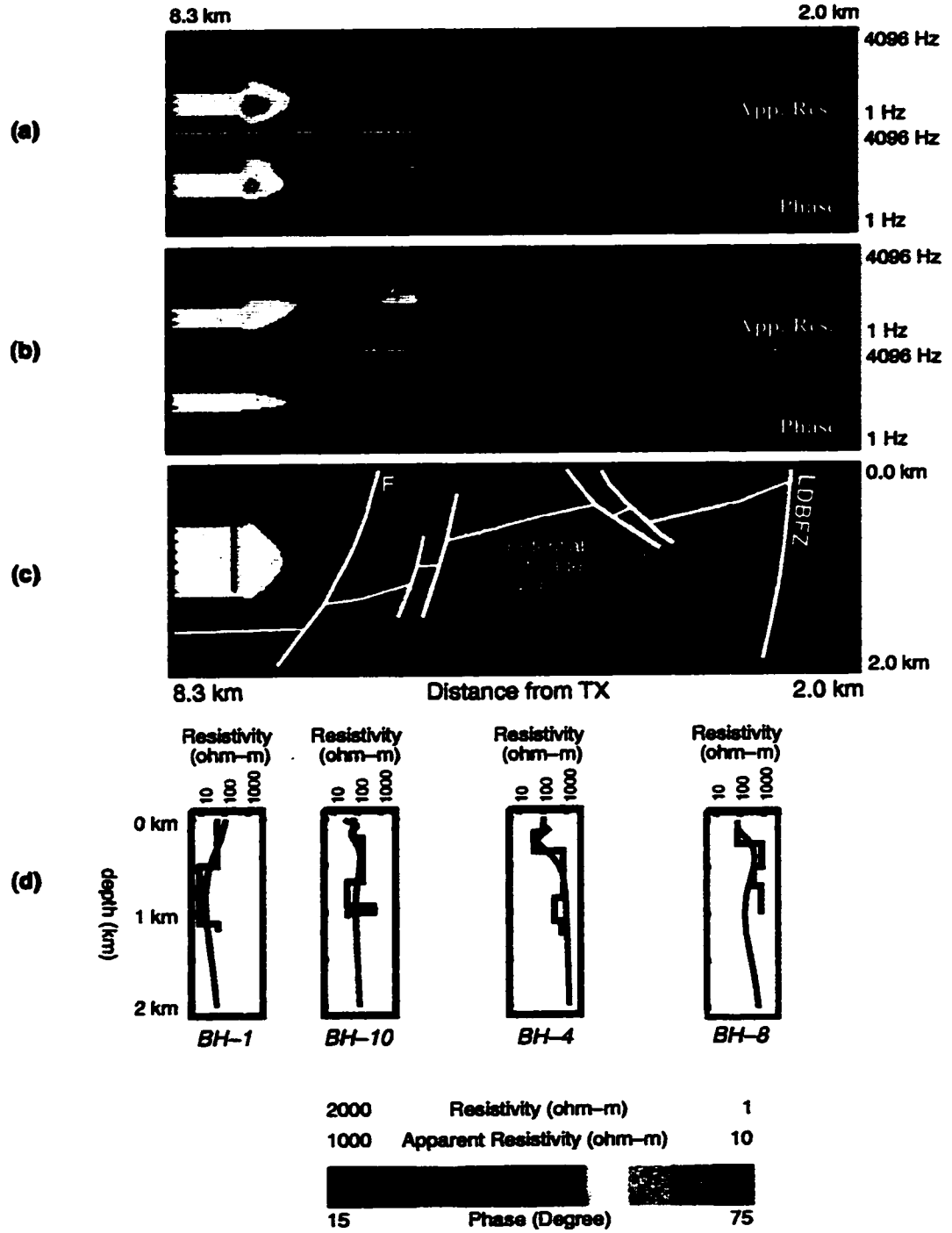
Figure 5.14: Sellafield survey: (a) Measured TE data. (b) CSAMT response of the inverted model (c). (c) The inverted resistivity model. (d) Comparison with well log data.
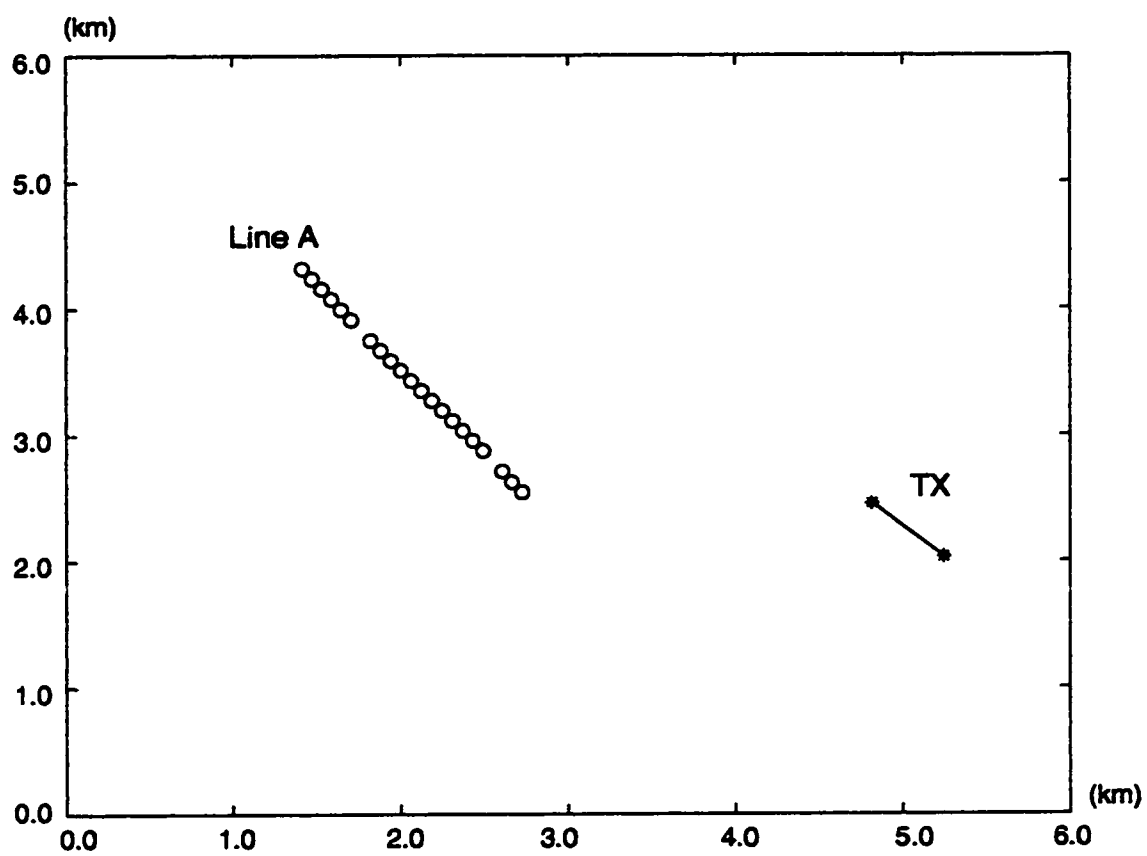
Figure 5.15: Salt dome survey: CSAMT survey layout of Line A.
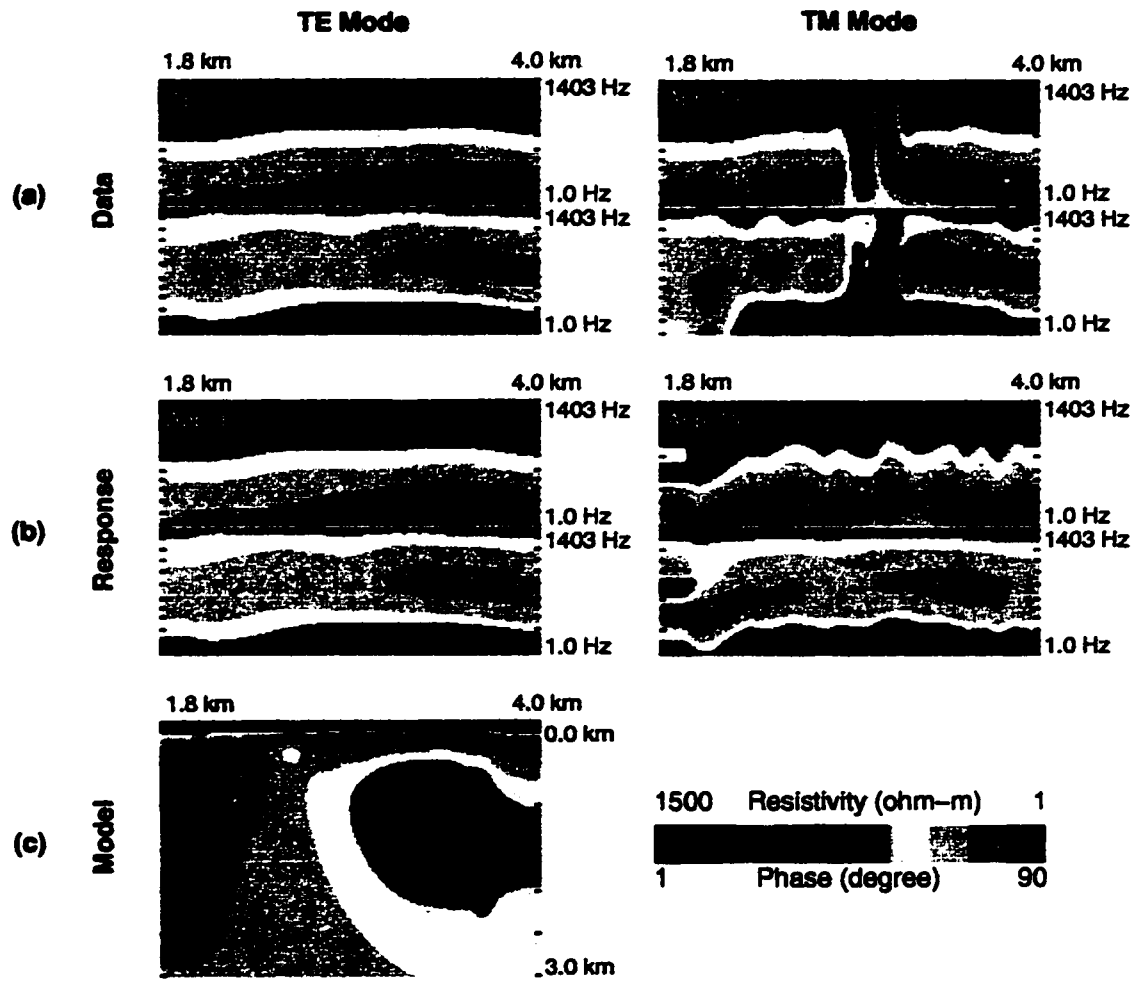
Figure 5.16: Salt dome survey: (a) Measured TE and TM data. (b) Computed TE and TM responses of the resulting model (c). (c) The inverted resistivity model.
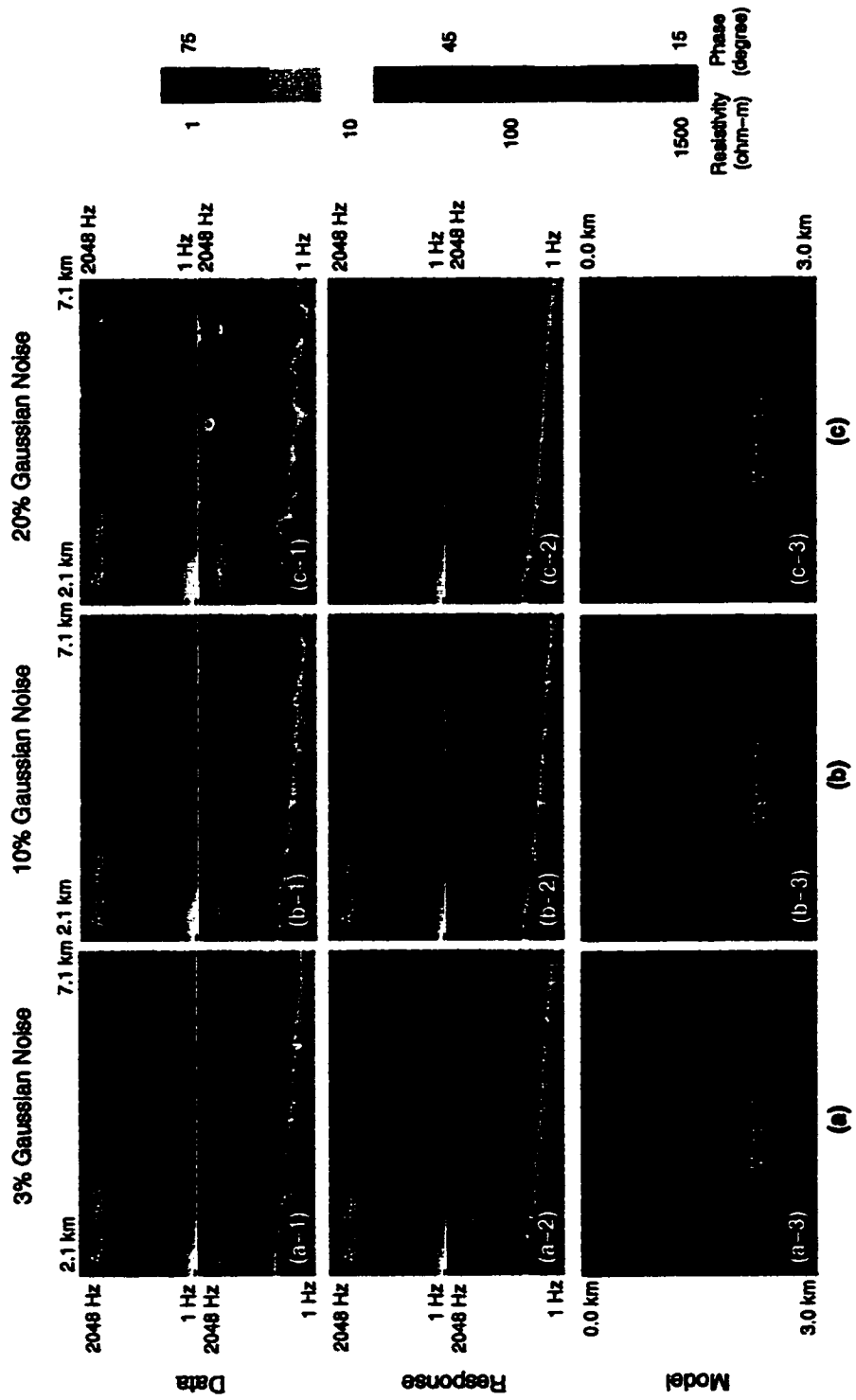
Figure 5.17: Inversion comparison for HMDy TE data on the non-main profile (x=0.0 km). Upper panels are data with different Gaussian noise. Middle panels are computed responses for inversion models. Lower panels are resistivity model inverted from data. (a) Data with 3% Gaussian noise and its inversion results. (b) Data with 10% Gaussian noise and its inversion results. (c) Data with 20% Gaussian noise and its inversion results.

Chapter 6

CONCLUSIONS AND SUGGESTIONS

This final chapter of the dissertation summarizes work done and offers some suggestions for future work.

6.1 Conclusions

I have developed an algorithm to invert CSAMT data from a horizontal electric dipole, a horizontal magnetic dipole and a finite-length horizontal electric dipole exciting a 2-D Earth. The algorithm combines a 2.5-D finite-element forward modeling method (Unsworth *et al.*, 1993) and the rapid relaxation inversion of Smith and Booker (1991). The algorithm uses an approximate method to compute sensitivity, which is closely related to the method used in RRI.

Calculating sensitivities is the most time-consuming step in the whole inverse process. The CSAMT forward modeling is computationally slow because of its 3-D source field and the singularity at the position occupied by transmitter. In order to rapidly compute sensitivities, I have adopted the philosophy of approximating them. I have derived approximate CSAMT sensitivities (CSAMT-RRI) by following the perturbation method used by Smith and Booker (1991) for the MT problem. The approximate sensitivities are valid for data collected on a non-main profile as well as the main profile. The Fréchet kernel functions for CSAMT have the same form of those for MT except the EM fields in the kernels are computed from the 2.5-D CSAMT forward modeling. I have compared the CSAMT-RRI sensitivities with the exact sensitivities by the perturbation method. Based on three models – a 100 Ωm half-

space, a three-layered earth and two dipping prisms with a conductive overburden, I find that (1) the corresponding curves for $\partial\rho_a/\partial\sigma_i$ and $\partial\phi/\partial\sigma_i$ from CSAMT-RRI and the perturbation method are broadly similar in shape and (2) a constant ratio exists between CSAMT-RRI and true sensitivities for all sites at transmitter-receiver offsets greater than one skin depth for each model. The CSAMT-RRI sensitivities are finally justified by the successful inversions of synthetic and field data.

I have also established a relationship between RRI inversion and standard inversion through the sensitivity matrix. RRI does not explicitly have a 2-D sensitivity matrix, but from the RRI inversion scheme, an implicit 2-D RRI sensitivity matrix can be constructed: the sensitivities of data to the cells directly below the observation site are computed from the formulas derived by Smith and Booker (1991) and the sensitivities of data to the rest of cells are approximated to be zero. The approximation of zero sensitivities from side cells decouples a 2-D inversion for all sites into a series of pseudo 1-D inversions at each site. I have shown that RRI sensitivities do consider the horizontal derivatives, which are approximated by the fields from the last iteration, and clarified the contributions from the horizontal derivative term in the governing equation and the cells horizontally adjacent to the site. Yamane *et al.* (1996) derived sensitivities with a Fréchet kernel including a horizontal derivative. I have compared their simplified GRRI sensitivities with RRI and true sensitivities and found that their horizontal derivative should not be included in the Fréchet kernel function. The deviation of GRRI sensitivities from RRI and true sensitivities are very large at some sites for the two quarter-space model, but the recovered models from GRRI and RRI inversions for the two quarter-space model and the same two dipping prism model are very similar. Combined with the results from CSAMT-RRI sensitivities, this implies that the requirement for the accuracy of the sensitivity matrix is probably less strict for an iterative inversion than what one usually anticipates.

In order to invert data from a horizontal magnetic dipole and a finite-length horizontal electric dipole, I have extended the 2.5-D finite-element forward modeling

method for a horizontal magnetic dipole and a finite-length horizontal electric dipole. The 2.5-D forward modeling method is flexible for various sources. The nature of the source is introduced by the primary field, which is defined as EM fields in wavenumber domain for a simple conductivity structure. I followed the work of Harrington (1961) and Ward and Hohmann (1988) to derive EM fields in wavenumber domain for 1-D layered earth for HED, HMD and FLHED sources. Numerical results have been computed for some models. The results show that source effects from HED and HMD are different in appearance for apparent resistivity and phase.

Finally, I have tested the algorithm on synthetic and field data and obtained promising results.

6.2 Suggestions

Although I have developed a working, practical 2-D CSAMT inversion, there are several things that should be addressed to improved its performance and reliability:

(1) Conduct a comparison of the CSAMT-RRI inverse algorithm with the standard exact 2-D Féchet derivative method to test how much the approximate sensitivity affects inversion results. The synthetic data tests for the two prism model show that the conductive body closer to the transmitter is normally not resolved as well as the other one. The possible explanations for this could be (a) the use of the approximate sensitivity, and (b) physical restraints in the near field. The comparison will answer this question.

(2) Make the sensitivity matrix more accurate by including additional sensitivities. The inversion uses only the sensitivities of cells directly below the site. Skin depth arguments indicate that cells which are within one skin depth range of an observation site should have significant sensitivities to the data at that site, while the rest of cells have near zero sensitivities. So the standard sensitivity matrix is very nearly a sparse matrix. An inversion would be more efficient if one could take advantage

of the sparse property. Such inversion could be implemented by inverting several sites (say N_s) simultaneously. Thus an inversion can be divided in a series of N_s-site inversions. N_s is less than the number of total sites, N_t. If $N_s = N_t$, it becomes the standard inversion. This implementation localizes important contributions to data. Such implementation could be called localized 2-D inversion. Such a philosophy could be readily extended to 3-D inversion, where it would possibly have more gains in saving computation resources.

(3) Incorporate topography into the inversion. In many practical applications, topography may have an important contribution to the response and should not be ignored. This work should not be difficult to implement.

(4) Reorganize the code to make the implementation consistent between the 2.5-D forward modeling and the inversion. The 2.5-D forward modeling was incorporated into RRI without considering a lot of subtle inconsistencies between them ranging from implementation philosophy to coding level. In implementation philosophy, for example, the 2.5-D forward modeling uses the finite-element method while RRI expects the fields were calculated by a finite-difference method. In coding, for instance, the 2.5-D forward modeling numbers model parameters row by row, but RRI numbers them column by column. These inconsistencies effect both computer resources and inversion performance.

(5) Allow the code to accommodate data with sources at different locations. Currently the code can invert data from sources (at most, two transmitters) at the same location. In practice, because of transmitter power limitation, especially for HMD, the transmitter is often relocated when receivers cannot receive a sufficiently strong signal.

REFERENCES

Adhidjaja, J.I., and Hohmann, G.W., 1989, A finite-difference algorithm for the transient electroamgnetic response of a three-dimensional body: *Geophys. J. Int.*, 98, 233-242.

Archie, G.E., 1942, The electrical resistivity log as an aid in determining some reservoir characteristics, Am. Inst. Min. Metallurg. Petr. Eng. Tech. Paper1422.

Backus, G., 1970a, Inference from inadequate and inaccurate data, I. *Proc. Nat. Acad. Sci.*, 65, 1-7.

Backus, G., 1970b, Inference from inadequate and inaccurate data, II. *Proc. Nat. Acad. Sci.*, 65, 281-287.

Backus, G., 1970c, Inference from inadequate and inaccurate data, III. *Proc. Nat. Acad. Sci.*, 67, 282-289. Backus, G., and Gilbert, F., 1968, The resolving power of gross earth data, *Geophys. J. R. astr. Soc.*, 16, 169-205.

Banos, A., 1966, Dipole radiation in the presence of a conducting half-space: New York, Pergamon Press.

Bartel, L. C. and Jacobson, R. D., 1987, Results of a controlled-source audio frequency magnetotelluric survey at the Puhimau thermal area, Kilauea Volcano, Hawaii, *Geophysics*, **52**, 665-677.

Best, M.E., Duncan, P., Jacobs, F.J., and Scheen, W.L., 1985, Numerical modeling of the electromagnetic response of three-dimensional conductors in a layered earth: *Geophysics*, 50, 665-676.

Branin, F.H., Jr., 1973, Network sensitivity and noise analysis simplied, *IEEE Transactions on Circuit Theory*, CT-20, 285-288.

Brayton, R.K., and Spence, R., 1980, Sensitivity and Optimization, Elsevier Science Publishing Co.

Cagniard, L., 1953, Basic theory of the magneto-telluric method of geophysical prospecting: *Geophysics*, 18, 605-635.

Cantwell, T., and Madden, T.R., 1960, Preliminary report on crustal magnetotelluric measurements, *Journal of Geophysical Research*, 65, No. 12, 4202-4205.

Cater, R.D., Kemp, L.F., Jr., Pierce, A.C., and Williams, D.L., 1974, Performance matching with restraints, *Society of Petroleum Engineering Journal*, 14, 187-196.

Chave, A.D., 1984, The Frechet derivatives of electromagnetic induction, *Journal of Geophysical Research*, 89, 3373-3380.

Chave, A.D., Thomson, D.J., and Ander, M.E., 1987, On the robust estimation of power spectra, coherences, and transfer functions, *Journal of Geophysical Research*, 92, 633-648.

Chen, Y.M., 1985, Generalized pulse-spectrum technique. *Geophysics*, 50, 1664-1675.

Coggon, J.H., 1971, Electromagnetic and electrical modeling by the finite element method: *Geophysics*, 36, 132-155.

Constable, S.C., Parker, R.L., and Constable, C.G., 1987, Occam's inversion: a practical algorithm for generating smooth models from EM sounding data, *Geophysics*, 52, 289-300.

deGroot-Hedlin, C., and Constable, S.C., 1990, Occam's inversion to generate smooth, two-dimensional models from magnetotelluric data, *Geophysics*, 55, 1613-1624.

d'Erceville, I., and Kunetz, G., 1962, The effect of a fault on the earth's natural electromagnetic field, *Geophysics*, XXVII, 651-665.

Egbert, G., and Booker, J.R., 1986, Robust estimation of geomagnetic transfer functions, *Geophys. J. R. astr. Soc.*, 87, 173-194.

Everett, M.E., 1990, Mid-ocean ridge electromagnetics: Ph.D. thesis, University of Toronto.

Farquharson, C.G., and Oldenburg, D.W., 1995, Approximate sensitivities for the multi-dimensional electromagnetic inverse problem, *International symposium on three-dimensional electromagnetics*, Schlumberger-Doll Research, CT, 335-341.

Franklin, J.L., 1970, Well-posed stochastic extensions of ill-posed linear problems, *J. Math. Anal. Appl.*, 31, 682-716.

Gamble, T.D., Goubau, W.M., and Clarke, J., 1979a, Magnetotellurics with a remote magnetic reference, *Geophysics*, 44, 53-68.

Gamble, T.D., Goubau, W.M., and Clarke, J., 1979b, Error analysis for remote reference magnetotellurics, *GEophysics*, 44, 959-968.

Goldman, M.M., and Stoyer, C.H., 1983, Finite-difference calculations of the transient field of an axially symmetric earth for vertical magnetic dipole excitation: *Geophysics*, 48, 953-963.

Goldstein, M.A., and Strangway, D.W., 1975, Audio-frequency magnetotellurics with a grounded electric dipole source, *Geophysics*, 40, 669-683.

Griffel, D.H., 1981, Applied Functional Analysis, Ellis Horwood Limited.

Groom, R.W., and Bailey, R.C., 1989, Decomposition of magnetotelluric impedance tensor in the presence of local three-dimensional galvanic distortion, *J. Geophys. Res.*, 94, 1913-1925.

Groom, R.W., and Bailey, R.C., 1991, Analytical investigations of the effects of near-surface three-dimensional galvanic scatterers on MT tensor decomposition, *Geophysics*, 56, 496-518.

Hohmann, G.W., 1971, Electromagnetic scattering by conductors in the earth near a line source of current: *Geophysics*, 36, 101-131.

Hohmann, G.W., 1975, Three-dimensional induced polarization and electromagnetic modeling: *Geophysics*, 40, 309-324.

Hohmann, G.W., and Raiche, A.P., 1988, Inversion of controlled source electromagnetic data, In: *Electromagnetic Methods in Applied Geophysics, Vol. 1, Theory*, M. Nabighian (ed.), Society of Exploration Geophysics.

Ishimaru, Akira, 1991, Electromagnetic wave propagation, radiation, and scattering, Englewood Cliffs, N.J., Prentice Hall.

Jones, A.G., 1988, Static shift of magnetotelluric data and its removal in a sedimentary basin environment, *Geophysics*, 53, 967-978.

Jones, F.W., and Price, A.J., 1971, Geomagnetic effects of sloping and shelving dis-

continuities of earth conductivity: *Geophysics*, 36, 58-66.

Jordan, T.H., and Franklin, J.N., 1971, Optimal solutions to a linear inverse problem in geophysics, *Proc. Nat. Acad. Sci.*, 68, 291-293.

Jupp, D.L.P., and Vozoff, K., 1977, Two-dimensional magnetotelluric inversion, *Geophysical Journal of the Royal Astronomical Society*, 50, 333-352.

Keller, G.V., 1987, Rock and mineral properties, in *Electromagnetic Methods in Applied Geophysics - Theory*, Vol.1, 13-51, ed. Nabighian, M.N., Soc. Expl. Geophys., Tulsa.

Kong, J.A., 1972, Electromagnetic fields due to dipole antennas over stratified anisotropic media, *Geophysics*: 37, No.6, 985-996.

Kuo, J.T., and Cho, V.H., 1980, Transient time-domain electromagnetics: *Geophysics*, 45, 271-291.

Lanczos, C., 1960, Linear Differential Operators, D. Van Nostrand.

Lee, K.H., 1978, Electromagnetic scattering by a two-dimensional inhomogeneity due to an oscillating magnetic dipole source: Ph.D. thesis, Univ. of California, Berkeley.

Lee, K.H., and Morrison, H.F., 1985, A numerical solution for the electromagnetic scattering by a two-dimensional inhomogeneity: *Geophysics*, 50, 1163-1165.

Lee, K.H., Pridmore, D.F. and Morrison, H.F., 1981, A hybrid three-dimensional electromagnetic modeling scheme: *Geophysics*, 46, 796-805.

Lines, L.R., and Jones, F.W., 1973, The perturbation of alternating geomagnetic fields by three-dimensional island structure: *Geophys. J. Roy. Astr. Soc.*, 32, 133-154.

Lu, X., Unsworth, M.J., and Booker, J.R., An analysis of RRI Sensitivity. (to be submitted to *Journal of Applied Geophysics*)

Lu, X., Unsworth, M.J. and Booker, J.R., Rapid relaxation inversion of CSAMT data. (submitted to *Journal of Geophysics International*, in press)

Lu, X., Unsworth, M.J. and Booker, J.R., 1997, Rapid Inversion of CSAMT data,

Proceedings of High-Resolution Geophysics, Tucsoni. (in CD).

Lu, X., Unsworth, M.J. and Booker, J.R., 1997, Two-dimensional inversion of tensor CSAMT data, Expanded Abstracts, 67th Ann. Internat. Mtg., Soc. Expl. Geophys. Vol.1, 362-365.

MacInnes, S.C., 1987, Lateral effects in controlled source audiomagnetotellurics: Ph.D. dissertation, Univ. of Arizona, Tucson.

Mackie, R.L., and Madden, T.R., 1993, Three-dimensional magnetotelluric inversion using conjugate gradients, *Geophys. J. Int.*, 115, 215-229.

Mackie, R.L., Madden, T.R., and Wannamaker, P.E., 1993, Three-dimensional magnetotelluric modeling using difference equations - Theory and comparisons to integral equation solutions, *Geophysics*, 58, 215-226.

Madden, T.R., and Mackie, R.L., 1989, Three-dimensional magnetotelluric modeling and inversion, *Proc. Inst. Electron. Electric. Eng.*, 77, 318-333.

Madden, T.R., and Nelson, P., A defense of Cagniard's magnetotelluric method, in *Magnetotelluric Methods*, ed. Vozoff, K., Soc. Expl. Geophys., Tulsa.

McGillivray, P.R., and Oldenburg, D.W., 1990, Methods for calculating Frechet derivatives and sensitivities for the non-linear inverse problem: A comparative study, *Geophysical Prospecting*, 38, 499-524.

Moghaddam, M., Yannakakis, E.J., Chew, W.C., and Randall, R., 1991, Modeling of the subsurface interface radar: *J. Elect. Waves and Appl.*, 5, 17-39.

Neuman, S.P., 1980, Adjoint-state finite element equations for parameter estimation, In: *Proceedings of the Third International Congress on Finite Elements in Water Resources*, 2.66-2.75, University of Mississippi. Newman, G.A. and Alumbaugh, D.L., 1997, Three-dimensional massively parallel electromagnetic inversion-I. Theory, *Geophys. J. Int.*, 128, 345-354.

Newman, G.A., Hohmann, G.W., and Anderson, W.L., 1986, Transient electromagnetic response of a three dimensional body in a layered earth: *Geophysics*, 51, 1608-1627.

Oden, J.T., and Carey, G.F., 1983, An introduction to the finite-element method: Prentice-Hall, Inc.

Oldenburg, D.W., 1978, The interpretation of direct current resistivity measurements, *Geophysics*, 43, 610-625

Oldenburg, D.W., 1979, One dimensionaal inversion of natural source magnetotelluric observations, *Geophysics*, 44, 1218-1244.

Oldenburg, D.W., 1983, Funnel functions in linear and non-linear appraisal, *J. Geophys. Res.*, 88, 7387-7398.

Oristaglio, M.L., and Hohmann, G.W., 1984, Diffusion of electromagnetic fields in a two-dimensional earth: A finite-difference approach: *Geophysics*, 49, 870-894.

Oristaglio, M.L., and Worthington, M.H., 1980, Inversion of surface and borehole magnetic data for two-dimensional electrical conductivity model, *Geophysical Prospecting*, 28, 633-657.

Oristaglio, M.L. and Spies, B., 1995, Three-dimensional electromagnetics: Schlumberger-Doll Research, CT.

Palacky, G.J., 1987, Resistivity characteristics of geologic targets, in *Electromagnetic Methods in Applied Geophysics - Theory*, Vol. 1, 53-129, ed. Nabighian, M.N., Soc. Expl. Geophys., Tulsa.

Parker, R.L., 1970, The inverse problem of electromagnetic induction: existence and construction of solutions based on incomplete data, *J. Geophys. Res.*, 85, 4421-4428.

Parker, R.L., 1975, The theoryof ideal bodies for gravity interpretation, *Geophys. J. R. astr. Soc.*, 42, 315-334.

Parker, R.L., 1977, The Frechet derivative for the one-dimensional electromaagnetic induction problem, *Geophysical Journal of the Royal Astronomical Society*, 49, 543-547.

Parker, R.L., 1980, The inverse problem of electrical conductivity in the mantle, *Geophys. J. R. Astr. Soc.*, 22, 121-138

Parker, R.L., 1981, The existence of a region inaccessible to magnetotelluric sounding, *Geophys. J. R. astr. Soc.*, 68, 165-170.

Parker, R.L., and Whaler, K.A., 1981, Numerical methods for establishing solutions to the inverse problem of electromagnetic induction, *J. Geophys. Res.*, 86, 9574-9584.

Parry, J.R., and Ward, S.H., 1971, Electromagnetic scattering from cylinders of arbitrary cross-section in a conductive half-space: *Geophysics*, 36, 67-100.

Price, A.T., 1962, The theory of magnetotelluric methods when the source field is considered, *Journal of Geophysical Research*, 67, No.5, 1907-1918.

Pridmore, D.F., Hohmann, G.W., Ward, S.H., and Sill, W.R., 1981, An investigation of finite-element modeling for electrical and electromagnetic data in three dimensions: *Geophysics*, 46, 1009-1024.

Raiche, A.P., 1974, An integral equation approach to 3D modeling: *Geophys. J. Roy. Astr. Soc.*, 36, 363-376.

Roach, G.F., 1980, Green's Functions, Cambridge University Press.

Reddy, I.K., Rankin, D., and Phillips, R.J., 1977, Three-dimensional modeling in magnetotelluric and magnetic variational sounding: *Geophys. J. Roy. Astr. Soc.*, 51, 313-325.

Rodi, G.F., 1976, A technique for improving accuracy of finite element solution for MT data, *Geophysical Journal of the Royal Astronomical Society*, 49, 483-506.

Routh, P.S. and Oldenburg, D.W., 1996, Inversion of controlled-source audio-Frequency magnetotelluric data for a horizontally-layered earth, *Expanded Abstracts, 66th Ann. Internat. Mtg.*, Soc. Expl. Geophys.

Sasaki, Y., Yoshihiro, Y., and Matsuo, K., 1992, Resistivity imaging of controlled-source audiofrequency magnetotelluric data: *Geophysics*, 57, 952-955.

Silvester, P., and Haslam, C.R.S., 1972, Magnetotelluric modeling by the finite element method: *Geophys. Prosp.*, 20, 872-891.

Skyes, J.F., and Wilson, J.L., 1984, Adjoint Sensitivity theory for the finite element

method, In: *Proceedings of the Fifth International Congress on Finite Elements in Water Resources*, 3-12.

Smith, J.T., and Booker, J.R., 1988, Magnetotelluric inversion for minimum structure: *Geophysics*, 53, 1565-1576.

Smith, J.T., and Booker, J.R., 1991, Rapid inversion of two and three- dimensional magnetotelluric data: *J. Geophys. Res.*, 96, 3905-3922.

Smith, J.T., 1996, Conservative modeling of 3-D electromagnetic fields; Part 1, Properties and error analysis: *Geophysics*, 61, 1308-1318.

Sommerfield, A., 1949, Partial differential equations in physics: New York, Academic Press Inc.

Stoyer, C.H., 1977, Electromagnetic fields of dipoles in stratified media: *IEEE Trans. Antennas Propagat.*, AP-25, 547-552.

Stoyer, C.H., and Greenfield, R.J., 1976, Numerical solutions of the response of a two-dimensional earth to an oscillating magnetic dipole source: *Geophysics*, 41, 519-530.

Sugeng, F. and Raiche, A.P., 1992, Comparing 3-D controlled source time-domain response of 2-D and elongated 3-D conductors in layered conducting hosts: *IAGA 11th Workshop on EM Induction in the Earth*, Wellington, NZ

Swift, C.M., Jr., 1971, Theoretical magnetotelluric and turam response from two-dimensional inhomogeneities: *Geophysics*, 36, 38-52.

Tang, C.M., 1979, Electromagnetic fields due to antennas embedded in stratified anisotropic media: *IEEE Trans. Antennas Propagat.*, AP-27, No.5, 665-670.

Tarantola, A., 1984, Linearized inversion of seismic reflection data, *Heophysical Prospecting*, 32, 998-1015.

Tikhonov, A.N., 1950, Determination of the electrical characteristics of the deep state of the earth's crust, *Dok. Akad. Nauk, USSR*, 73, 2, 295-297

Ting, S.C., and Hohmann, G.W., 1981, Integral equation modeling of three-dimensional magnetotelluric response: *Geophysics*, 46, 182-197.

Townley, L.R., and Wilson, J.L., 1985, Computationally efficient algorithms for parameter estimation and uncertainty propagation in numerical models of groundwater flow, *Water Resources Research*, 21, 1851-1860.

Unsworth, M.J., Travis, B.J., and Chave, A.D., 1993, Electromagnetic induction by a finite dipole over a 2-D earth: *Geophysics*, 58, 184-214.

Vozoff, K., 1988, The magnetotelluric method, in *Electromagnetic Methods in Applied Geophysics*, Vol.2, ed. Nabighian, M.N., Soc. Expl. Goephys., Tulsa.

Vozoff, K., 1986, Magnetotelluric methods, *Geophys. Reprint Ser. No. 5*, Soc. Expl. Geophys., Tulsa.

Wait, J.R., 1953, Propagation of radiowaves over a stratified ground: *Geophysics*, 18, 416-422.

Wait, J.R., 1954, On the relation between telluric currents and the earth's magnetic field, *Geophysics*, 19, 281-289.

Wang, T., and Hohmann, G.W., 1993, A finite-difference time-domain solution for three-dimensional electromagnetic modeling, *Geophysics*, 58, 797-809.

Wannamaker, P.E., 1991, Advances in three-dimensional magnetotelluric modeling using integral equations: *Geophysics*, 56, 1716-1728.

Wannamaker, P., 1997, Tensor CSAMT survey over the Sulphur Springs thermal area,Valles Caldera, New Mexico, U.S.A., Part I: Implications for structure of the western caldera, *Geophysics*, **62**, 451-465.

Wannamaker, P.E., Hohmann, G.W., and San Filipo, W.A., 1984, Electromagnetic modeling of three dimensional bodies in layered earths using integral equations: *Geophysics*, 49, 60-74.

Ward, S.H., 1967, Electromagnetic theory for geophysical applications, in Mining geophysics, Vol. 2, part A: Tusla, SEG, 10-196.

Weidelt, P., 1972, The inverse problem of geomagnetic induction, *Z. Geophys.*, 38, 257-289.

Weidelt, P., 1975, Electromagnetic induction in three-dimensional structure: *J. Geo-*

phys., 41, 85-109. Weidelt, P., 1975, Inversion of two-dimensional conductivity structures, *Physics of the Earth and Planetary Interiors*, 10, 282-291.

Whittall, K.P., and Oldenburg, D.W., 1986, Inversion of magnetotelluric data using a practical inverse scattering formulation, *Geophysics*, 51, 383-395

Xiong, Z., 1992, Electromagnetic modeling of 3-D structures by the method of system iteration using integral equations: *Geophysics*, 57, 1556-1561.

Yamane, K., Takasugi, S., and Lee, K.H., 1996, A new magnetotelluric inversion scheme using generalized RRI, *Journal of Applied Geophysics*, 35, 209-213.

Yamashita, M., and Hallof, P.G., 1985, CSAMT case histories with a multi-channel CSAMT system and discussion of near-field data correction: Phoenix Geophys., Ltd.

Zhdanov, M.S., Golubev, N.G., Sichak, V.V., Varentsov, I.M., 1982, The construction of effective methods for electromagnetic modeling: *Geophys. J. Roy. Astr. Soc.*, 68, 589-607.

Zeidler, E., 1985, Nonlinear Functional Analysis and its applications III - Variational Methods and Optimization. Springer-Verlag, Inc.

Zienkowicz, O.C., 1967, The finite-element method in structural and continuum mechanics: McGraw Hill Book Co.

Zonge, K. L. and Hughes, L. J., 1991, Controlled source audio-frequency magnetotellurics, in *Electromagnetic Methods in Applied Geophysics*, Vol. 2, B, pp. 713-809, ed. Nabighian, M. N., Soc. Expl. Geophys., Tulsa.

Appendix A

ELECTROMAGNETIC FIELDS

The 2.5-D forward modeling algorithm used in CSAMT inversion requires that electric fields (so called primary fields) be computed for a specific model which usually is a simple model. To compute electromagnetic fields, we always have to start with the Maxwell's equations and generally end with solving a boundary-value problem. The boundary-value problem can be solved in terms of the vector electric and magnetic field intensity functions or in terms of vector and/or scalar potential functions from which the vector field functions may be derived.

Kong (1972) and Tang (1979) give solutions due to dipole antennas in stratified anisotropic media by decomposing a general wave field into TM and TE modes, employing the concept of propagation matrices, and expressing the reflection coefficients in terms of continuous fractions. But solving EM boundary-value problem was mostly carried out by means of potential functions. Several different sets of potential functions appear in the literature. Hertzian potential functions are the most widely used set, and are used for the half-space case by Sommerfeld (1949) and Banos (1966); for the stratified isotropic media by Wait (1951, 1953, 1970), Wolf (1946), Bhattacharya (1967), Ward (1967), Stoyer (1977), etc; for the anisotropic media by Chetaev (1963), Wait (1966a, b), Praus (1965), Sinha and Bhattacharya (1967), and Sinha (1968, 1969). Chave (1982) and Chave and Luther (1990) use two scalar potentials, which are derived from the Mie representation of the magnetic induction **B**, to get the solution for a electric dipole source over a layered earth. In their solutions, the electromagnetic fields can be separated into the poloidal magnetic (PM) mode and the toroidal magnetic (TM) mode. Ward and Hohmann (1988) adapt the approach of

Harrington (1961) and use the Schelkunoff potentials, because of their symmetry and the ease of relating them to the TE and TM modes of excitation, to derive the EM fields for the various finite sources over a layered half-space in frequency and time domain.

Most of the derivation for EM fields below is based on the work of Harrington (1961) and Ward and Hohmann (1988).

A.1 Theory

A.1.1 Schelkunoff potentials

The Maxwell's equations (2.12) and (2.13) are written as

$$\nabla \times \mathbf{H} = \tilde{y}\mathbf{E} + \mathbf{J}_e^s \tag{A.1}$$

$$\nabla \times \mathbf{E} = -\tilde{z}\mathbf{H} - \mathbf{J}_m^s \tag{A.2}$$

where time factor $e^{i\omega t}$ is used. $\tilde{y} = \sigma + i\omega\varepsilon$ is the admittivity, and $\tilde{z} = i\omega\mu$ the impedivity (Harrington, 1961). Equations (A.1) and (A.2) are linear; so total field can be considered as the sum of two parts, one $[\mathbf{E}_e, \mathbf{H}_e]$ produced by $\mathbf{J}_e^s$ and the other $[\mathbf{E}_m, \mathbf{H}_m]$ by $\mathbf{J}_m^s$.

$\mathbf{E}_e$ and $\mathbf{H}_e$ satisfy

$$\nabla \times \mathbf{H}_e = \tilde{y}\mathbf{E}_e + \mathbf{J}_e^s \tag{A.3}$$

$$\nabla \times \mathbf{E}_e = -\tilde{z}\mathbf{H}_e \tag{A.4}$$

and $\mathbf{E}_m$ and $\mathbf{H}_m$ satisfy

$$\nabla \times \mathbf{H}_m = \tilde{y}\mathbf{E}_m \tag{A.5}$$

$$\nabla \times \mathbf{E}_m = -\tilde{z}\mathbf{H}_m - \mathbf{J}_m^s \tag{A.6}$$

Taking the divergence of equations (A.4) and (A.5) yields

$$\nabla \cdot \mathbf{H}_e = 0 \tag{A.7}$$

$$\nabla \cdot \mathbf{E}_m = 0 \tag{A.8}$$

Equations (A.7) and (A.8) imply that $\mathbf{E}_m$ and $\mathbf{H}_e$ may be written as the curls of two vector functions,

$$\mathbf{H}_e = \nabla \times \mathbf{A} \tag{A.9}$$

$$\mathbf{E}_m = -\nabla \times \mathbf{F} \tag{A.10}$$

From equations (A.3), (A.4), (A.5), (A.6), (A.9), and (A.10), one can get

$$\nabla \times \nabla \times \mathbf{F} = \mathbf{J}_m^s + k^2 \mathbf{F} - \tilde{z}\nabla \phi^f \tag{A.11}$$

$$\nabla \times \nabla \times \mathbf{A} = \mathbf{J}_e^s + k^2 \mathbf{A} - \tilde{y}\nabla \phi^a \tag{A.12}$$

where $k^2 = -\tilde{y}\tilde{z} = \omega^2 \mu \varepsilon - i\omega\mu\sigma$, ϕ^f and ϕ^a are arbitrary scalars. If ϕ's are chosen according to

$$\nabla \cdot \mathbf{A} = -\tilde{y}\phi^a \qquad \nabla \cdot \mathbf{F} = -\tilde{z}\phi^f \tag{A.13}$$

Equations (A.11) and (A.12) are reduced to

$$\nabla^2 \mathbf{F} + k^2 \mathbf{F} = -\mathbf{J}_m^s \tag{A.14}$$

$$\nabla^2 \mathbf{A} + k^2 \mathbf{A} = -\mathbf{J}_e^s \tag{A.15}$$

The total electromagnetic field in terms of $\mathbf{A}$ and $\mathbf{F}$ is given by

$$\mathbf{E} = -\tilde{z}\mathbf{A} + \frac{1}{\tilde{y}}\nabla(\nabla \cdot \mathbf{A}) - \nabla \times \mathbf{F} \tag{A.16}$$

$$\mathbf{H} = -\tilde{y}\mathbf{F} + \frac{1}{\tilde{z}}\nabla(\nabla \cdot \mathbf{F}) + \nabla \times \mathbf{A} \tag{A.17}$$

Let us consider some particular choices of potentials.

$\mathbf{TM}_z$:

If $\mathbf{F} = 0$, then

$$\mathbf{E} = -\tilde{z}\mathbf{A} + \frac{1}{\tilde{y}}\nabla(\nabla \cdot \mathbf{A}) \tag{A.18}$$

$$\mathbf{H} = \nabla \times \mathbf{A} \qquad (A.19)$$

If the potential $\mathbf{A}$ is given by

$$\mathbf{A} = \psi \mathbf{z} \qquad (A.20)$$

Equations (A.18) and (A.19) can be expanded as

$$E_x = \frac{1}{\tilde{y}} \frac{\partial^2 \psi}{\partial x \, \partial z} \qquad\qquad H_x = \frac{\partial \psi}{\partial y}$$

$$E_y = \frac{1}{\tilde{y}} \frac{\partial^2 \psi}{\partial y \, \partial z} \qquad\qquad H_y = -\frac{\partial \psi}{\partial x}$$

$$E_z = \frac{1}{\tilde{y}} \left(\frac{\partial^2}{\partial z^2} + k^2 \right) \psi \qquad H_z = 0 \qquad (A.21)$$

A field with no H_z is called transverse magnetic to z ($\mathbf{TM}_z$).

$\mathbf{TE}_z$:

If $\mathbf{A} = 0$, and

$$\mathbf{F} = \psi \mathbf{z} \qquad (A.22)$$

then

$$\mathbf{E} = -\nabla \times \mathbf{F} \qquad (A.23)$$

$$\mathbf{H} = -\tilde{y}\mathbf{F} + \frac{1}{\tilde{z}} \nabla(\nabla \cdot \mathbf{F}) \qquad (A.24)$$

This can be expanded as

$$E_x = -\frac{\partial \psi}{\partial y} \qquad\qquad H_x = \frac{1}{\tilde{z}} \frac{\partial^2 \psi}{\partial x \, \partial z}$$

$$E_y = \frac{\partial \psi}{\partial x} \qquad\qquad H_y = \frac{1}{\tilde{z}} \frac{\partial^2 \psi}{\partial y \, \partial z}$$

$$E_z = 0 \qquad\qquad H_z = \frac{1}{\tilde{z}} \left(\frac{\partial^2}{\partial z^2} + k^2 \right) \psi \qquad (A.25)$$

A field with no E_z is called transverse electric to z ($\mathbf{TE}_z$).

A.1.2 Construction of solutions

We need to solve the boundary-value problems (A.14) and (A.15) for computing EM fields. The general solutions of the equations (A.14) and (A.15) can be constructed as the sum of the particular solution of the inhomogeneous differential equation and the complementary solution of the homogeneous equation. So $\mathbf{F}$ and $\mathbf{A}$ can be written as

$$\mathbf{F} = \mathbf{F}_{ps} + \mathbf{F}_{cs} \tag{A.26}$$

$$\mathbf{A} = \mathbf{A}_{ps} + \mathbf{A}_{cs} \tag{A.27}$$

As Harrington (1961) points out, the particular solution ($\mathbf{F}_{ps}$ and $\mathbf{A}_{ps}$) can be thought of as the field due to sources inside the region and the complimentary solution ($\mathbf{F}_{cs}$ and $\mathbf{A}_{cs}$) as the field due to sources outside the region. So he writes out the particular solution by using the potential integral solution.

The complementary solution is the solution of (A.14) and (A.15) in the source-free region. In source-free region, it is not necessary to think of $\mathbf{A}$ as due to $\mathbf{J}_e^s$ and $\mathbf{F}$ as due to $\mathbf{J}_m^s$. One can represent a field in terms of $\mathbf{A}$ or $\mathbf{F}$ or both, regardless of its actual source. Harrington (1961) also shows that an arbitrary field in a homogeneous source-free region can be expressed as the sum of a TM field and a TE field. For instance, we have a field with E_z and H_z components, which is neither TE nor TM. We can determine ψ^a (A type source) and ψ^f (F type source) by, respectively,

$$\frac{\partial^2 \psi^a}{\partial z^2} + k^2 \psi^a = \tilde{y} E_z \tag{A.28}$$

$$\frac{\partial^2 \psi^f}{\partial z^2} + k^2 \psi^f = \tilde{z} H_z \tag{A.29}$$

Then the complementary solution would be superposition of equations (A.21) and (A.25).

Therefore the boundary problem (A.14) and (A.15) has been solved. We will practice this approach to compute EM fields for a layered half-space in the following.

A.1.3 Finite sources over a layered half-space

Finite sources used in geophysics are usually oriented in one direction at a time, so (A.14) and (A.15) can be reduced to scalar equations. Because the conductivity of a layered half-space model only changes with the depth, the two scalar partial differential equations can be converted to ordinary differential equations of z by 2-D Fourier transform.

$$\frac{d^2\hat{F}}{dz^2} - u^2\hat{F} = -\hat{J}_m^s \tag{A.30}$$

$$\frac{d^2\hat{A}}{dz^2} - u^2\hat{A} = -\hat{J}_e^s \tag{A.31}$$

where $u^2 = k_x^2 + k_y^2 - k^2$.

Now let us find a particular solution to equations (A.30) and (A.31). Solving those two equations is equivalent to solving the following equation

$$\frac{d^2\hat{G}}{dz^2} - u^2\hat{G} = -\delta(z + h) \tag{A.32}$$

where the source is at $z = -h$. Its solution is the Green's function given by

$$\hat{G}(k_x, k_y, z) = \frac{e^{-u|z+h|}}{2u} \tag{A.33}$$

Once we have the Green's function to equation (A.32), we may give a particular solution to equations (A.30) and (A.31) by

$$\hat{F}_{ps}(k_x, k_y, z) = F_p(k_x, k_y)e^{-u|z+h|} \tag{A.34}$$

$$\hat{A}_{ps}(k_x, k_y, z) = A_p(k_x, k_y)e^{-u|z+h|} \tag{A.35}$$

where F_p and A_p depend on the particular sources $\mathbf{J}_m^s$ and $\mathbf{J}_e^s$.

The complementary solutions are the solutions to the homogeneous equations of (A.30) and (A.31), that is,

$$\frac{d^2\hat{F}}{dz^2} - u^2\hat{F} = 0 \tag{A.36}$$

$$\frac{d^2\hat{A}}{dz^2} - u^2\hat{A} = 0 \tag{A.37}$$

Equations (A.36) and (A.37) are in the same form as the plane wave equation for 1-D MT. Therefore the solutions of equations (A.36) and (A.37) can be easily written out as

$$\hat{F}_{cs}(k_x, k_y, z) = F^+(k_x, k_y)e^{-uz} + F^-(k_x, k_y)e^{uz} \tag{A.38}$$

$$\hat{A}_{cs}(k_x, k_y, z) = A^+(k_x, k_y)e^{-uz} + A^-(k_x, k_y)e^{uz} \tag{A.39}$$

where superscripts $+$ and $-$ stand for downward and upward propagating solutions, respectively.

Up to this point, we have finished deriving the general solutions for finite sources over a layered half-space. For an N-layered 1-D model, the solutions in each layer are summarized in Fig.A.1. Finally, solutions in the (x, y, z) domain can be obtained by 2-D inverse Fourier transform.

In the solutions, coefficients F_n^+, F_n^-, A_n^+, and A_n^- can be determined by the following boundary conditions.

$$
\begin{aligned}
\hat{F}_n(k_x, k_y, z) &= \hat{F}_{n+1}(k_x, k_y, z) \\
\frac{1}{\mu_n} \frac{\partial \hat{F}_n(k_x, k_y, z)}{\partial z} &= \frac{1}{\mu_{n+1}} \frac{\partial \hat{F}_{n+1}(k_x, k_y, z)}{\partial z}
\end{aligned}
\tag{A.40}
$$

$$
\begin{aligned}
\hat{A}_n(k_x, k_y, z) &= \hat{A}_{n+1}(k_x, k_y, z) \\
\frac{1}{\tilde{y}_n} \frac{\partial \hat{A}_n(k_x, k_y, z)}{\partial z} &= \frac{1}{\tilde{y}_{n+1}} \frac{\partial \hat{A}_{n+1}(k_x, k_y, z)}{\partial z}
\end{aligned}
\tag{A.41}
$$

at the boundary between layer n and layer $n + 1$. r_{TE} and r_{TM} are reflection coefficients, given by

$$r_{TE} = \frac{Y_0 - \tilde{Y}_1}{Y_0 + \tilde{Y}_1} \tag{A.42}$$

$$r_{TM} = \frac{Z_0 - \tilde{Z}_1}{Z_0 + \tilde{Z}_1} \tag{A.43}$$

where Y_0 and Z_0 are intrinsic admittance and impedance of free space, respectively, and given by

$$Y_0 = \frac{u_0}{z_0} \tag{A.44}$$

$$\left\{ \begin{matrix} \hat{F}(k_x,k_y,z) \\ \hat{A}(k_x,k_y,z) \end{matrix} \right\} = \left\{ \begin{matrix} F^-_{-1}(k_x,k_y) \\ A^-_{-1}(k_x,k_y) \end{matrix} \right\} e^{u_0 z}$$

◆ **TX at z = -h**

$$\left\{ \begin{matrix} \hat{F}(k_x,k_y,z) \\ \hat{A}(k_x,k_y,z) \end{matrix} \right\} = \left\{ \begin{matrix} F_p(k_x,k_y) \\ A_p(k_x,k_y) \end{matrix} \right\} \left[e^{-u_0(z+h)} + \left(\begin{matrix} r_{TE} \\ r_{TM} \end{matrix} \right) e^{u_0(z-h)} \right]$$

z = 0 **Surface of the Earth**

h_1
$$\left\{ \begin{matrix} \hat{F}(k_x,k_y,z) \\ \hat{A}(k_x,k_y,z) \end{matrix} \right\} = \left\{ \begin{matrix} F^+_1(k_x,k_y) \\ A^+_1(k_x,k_y) \end{matrix} \right\} e^{-u_1 z} + \left\{ \begin{matrix} F^-_1(k_x,k_y) \\ A^-_1(k_x,k_y) \end{matrix} \right\} e^{u_1 z}$$ **Layer 1**

h_2
$$\left\{ \begin{matrix} \hat{F}(k_x,k_y,z) \\ \hat{A}(k_x,k_y,z) \end{matrix} \right\} = \left\{ \begin{matrix} F^+_2(k_x,k_y) \\ A^+_2(k_x,k_y) \end{matrix} \right\} e^{-u_2 z} + \left\{ \begin{matrix} F^-_2(k_x,k_y) \\ A^-_2(k_x,k_y) \end{matrix} \right\} e^{u_2 z}$$ **Layer 2**

⋮

h_n
$$\left\{ \begin{matrix} \hat{F}(k_x,k_y,z) \\ \hat{A}(k_x,k_y,z) \end{matrix} \right\} = \left\{ \begin{matrix} F^+_n(k_x,k_y) \\ A^+_n(k_x,k_y) \end{matrix} \right\} e^{-u_n z} + \left\{ \begin{matrix} F^-_n(k_x,k_y) \\ A^-_n(k_x,k_y) \end{matrix} \right\} e^{u_n z}$$ **Layer n**

⋮

$$\left\{ \begin{matrix} \hat{F}(k_x,k_y,z) \\ \hat{A}(k_x,k_y,z) \end{matrix} \right\} = \left\{ \begin{matrix} F^+_N(k_x,k_y) \\ A^+_N(k_x,k_y) \end{matrix} \right\} e^{-u_N z}$$ **Layer N**

Figure A.1: Solutions in each layer for an N-layered earth. Finite sources are at $z = -h$.

$$Z_0 = \frac{u_0}{\tilde{y}_0} \tag{A.45}$$

$\tilde{Y}_1$ and $\tilde{Z}_1$ are surface admittance and impedance at $z = 0$ and can be computed by following formulas

$$\tilde{Y}_1 = Y_1 \frac{\tilde{Y}_2 + Y_1 \tanh(u_1 h_1)}{Y_1 + \tilde{Y}_2 \tanh(u_1 h_1)}$$

$$\vdots$$

$$\tilde{Y}_n = Y_n \frac{\tilde{Y}_{n+1} + Y_n \tanh(u_n h_n)}{Y_n + \tilde{Y}_{n+1} \tanh(u_n h_n)}$$

$$\vdots$$

$$\tilde{Y}_N = Y_N = \frac{u_N}{\tilde{z}_N} \tag{A.46}$$

$$\tilde{Z}_1 = Z_1 \frac{\tilde{Z}_2 + Z_1 \tanh(u_1 h_1)}{Z_1 + \tilde{Z}_2 \tanh(u_1 h_1)}$$

$$\vdots$$

$$\tilde{Z}_n = Z_n \frac{\tilde{Z}_{n+1} + Z_n \tanh(u_n h_n)}{Z_n + \tilde{Z}_{n+1} \tanh(u_n h_n)}$$

$$\vdots$$

$$\tilde{Z}_N = Z_N = \frac{u_N}{\tilde{y}_N} \tag{A.47}$$

A.2 Electromagnetic fields of a layered half-space

In this section we derive EM fields of a horizontal electric dipole, a horizontal magnetic dipole and a finite-length line source for a layered earth. All those finite sources are x-directed. The fields for a y-directed source can be obtained by a simple coordinate permutation from its x-directed counterpart since the conductivity of a layered earth only changes with the depth.

A.2.1 Horizontal electric dipole (HED)

For the x-directed horizontal electric dipole located at $z = -h$, only the x-component of $\mathbf{A}$ exists because of the symmetry. Thus equation (A.15) can be reduced to

$$\nabla^2 A_x + k_0^2 A_x = -Idl\delta(x)\delta(y)\delta(z+h) \tag{A.48}$$

Equation (A.48) can be transformed to a differential equation in z using the 2-D Fourier transform and becomes

$$\frac{d^2 \hat{A}_x}{dz^2} - u_0^2 \hat{A}_x = -Idl\delta(z+h) \tag{A.49}$$

Comparing this equation with (A.32) and (A.33), one can easily get the particular solution for the region between the source and the surface of the earth

$$\hat{\mathbf{A}} = \hat{A}_x \mathbf{x} = \frac{Idl}{2u_0} e^{-u_0(z+h)} \mathbf{x} \tag{A.50}$$

Using (A.18) and (A.19), one can get vertical components in the (k_x, k_y, z) domain

$$\hat{E}_z^p(k_x, k_y, z) = \frac{ik_x}{\tilde{y}_0} \frac{\partial}{\partial z} \hat{A}_x(k_x, k_y, z) = -\frac{Idl}{2\tilde{y}_0} ik_x e^{-u_0(z+h)} \tag{A.51}$$

$$\hat{H}_z^p(k_x, k_y, z) = -ik_y \hat{A}_x(k_x, k_y, z) = -\frac{Idl}{2u_0} ik_y e^{-u_0(z+h)} \tag{A.52}$$

The EM field has both TM_z and TE_z components. If the particular solution is broken into a TM_z field and a TE_z field, one can treat them separately. Substituting (A.35) into (A.21) in the (k_x, k_y, z) domain and equating $\hat{E}_z^p$ in equation (A.51), one gets

$$A_p(k_x, k_y) = -\frac{Idl}{2} \frac{ik_x}{k_x^2 + k_y^2} \tag{A.53}$$

Similarly using equations (A.25), (A.34) and (A.52), one obtains

$$F_p(k_x, k_y) = -\frac{\tilde{z}_0 Idl}{2u_0} \frac{ik_y}{k_x^2 + k_y^2} \tag{A.54}$$

Once the EM field is broken into TE and TM, the expression for $\mathbf{A}$ of (A.50) is not needed any more. Using the boundary conditions (A.40) and (A.41), the rest of coefficients in solutions of Fig.A.1 can be uniquely determined.

For a half-space, the solutions in the earth for HEDx at $z = 0$ are

$$\hat{A}_z(k_x, k_y, z) = -\frac{Idl}{2}\frac{ik_x}{k_x^2 + k_y^2}(1 + r_{TM})e^{-u_1 z} \qquad (A.55)$$

$$\hat{F}_z(k_x, k_y, z) = -\frac{\tilde{z}_0 Idl}{2u_0}\frac{ik_y}{k_x^2 + k_y^2}(1 + r_{TE})e^{-u_1 z} \qquad (A.56)$$

Then superposing equations (A.21) and (A.25) yields

$$\hat{E}_x(k_x, k_y, z) = \frac{Idl}{2}\left[-\frac{u_1}{\tilde{y}_1}(1 + r_{TM})k_x^2 - \frac{\tilde{z}_0}{u_0}(1 + r_{TE})k_y^2\right]\frac{1}{k_x^2 + k_y^2}e^{-u_1 z} \qquad (A.57)$$

$$\hat{E}_y(k_x, k_y, z) = \frac{Idl}{2}\left[-\frac{u_1}{\tilde{y}_1}(1 + r_{TM}) + \frac{\tilde{z}_0}{u_0}(1 + r_{TE})\right]\frac{k_x k_y}{k_x^2 + k_y^2}e^{-u_1 z} \qquad (A.58)$$

$$\hat{E}_z(k_x, k_y, z) = \frac{Idl}{2}\left[-\frac{ik_x}{\tilde{y}_1}(1 + r_{TM})\right]e^{-u_1 z} \qquad (A.59)$$

$$\hat{H}_x(k_x, k_y, z) = \frac{Idl}{2}\left[(1 + r_{TM}) - \frac{u_1}{u_0}(1 + r_{TE})\right]\frac{k_x k_y}{k_x^2 + k_y^2}e^{-u_1 z} \qquad (A.60)$$

$$\hat{H}_y(k_x, k_y, z) = \frac{Idl}{2}\left[-(1 + r_{TM})k_x^2 - \frac{u_1}{u_0}(1 + r_{TE})k_y^2\right]\frac{1}{k_x^2 + k_y^2}e^{-u_1 z} \qquad (A.61)$$

$$\hat{H}_z(k_x, k_y, z) = \frac{Idl}{2}\left[-\frac{ik_y}{u_0}(1 + r_{TE})\right]e^{-u_1 z} \qquad (A.62)$$

Finally, EM fields in the (x, y, z) space domain can be obtained using the 2-D inverse Fourier transform.

A.2.2 Horizontal magnetic dipole (HMD)

Similarly, the particular solution in the (k_x, k_y, z) domain for an x-directed horizontal magnetic dipole located at $z = -h$ is

$$\mathbf{F} = \hat{F}_x \mathbf{x} = \frac{\tilde{z}_0 m}{2u_0}e^{-u_0(z+h)}\mathbf{x} \qquad (A.63)$$

Then one can derive vertical components in the (k_x, k_y, z) domain from (A.18) and (A.19)

$$\hat{E}_z^p(k_x, k_y, z) = \frac{\tilde{z}_0 m}{2u_0}ik_y e^{-u_0(z+h)} \qquad (A.64)$$

$$\hat{H}_z^p(k_x, k_y, z) = -\frac{m}{2}ik_x e^{-u_0(z+h)} \tag{A.65}$$

The EM field has both TM_z and TE_z and can be broken into them separately with

$$A_p(k_x, k_y) = -\frac{k_0^2 m}{2u_0}\frac{ik_y}{k_x^2 + k_y^2} \tag{A.66}$$

and

$$F_p(k_x, k_y) = -\frac{\tilde{z}_0 m}{2}\frac{ik_x}{k_x^2 + k_y^2} \tag{A.67}$$

Once $A_p(k_x, k_y)$ and $F_p(k_x, k_y)$ are derived, the solutions in Fig.A.1 are completely determined by the boundary conditions.

For a half-space, the solutions in the earth for HMDx at $z = 0$ are

$$\hat{A}_z(k_x, k_y, z) = -\frac{k_0^2 m}{2u_0}\frac{ik_y}{k_x^2 + k_y^2}(1 + r_{TM})e^{-u_1 z} \tag{A.68}$$

$$\hat{F}_z(k_x, k_y, z) = -\frac{\tilde{z}_0 m}{2}\frac{ik_x}{k_x^2 + k_y^2}(1 + r_{TE})e^{-u_1 z} \tag{A.69}$$

Then using equations (A.21) and (A.25), one can derive EM components in the (k_x, k_y, z) domain

$$\hat{E}_x(k_x, k_y, z) = \frac{m}{2}\left[-\frac{k_0^2}{\tilde{y}_1}\frac{u_1}{u_0}(1 + r_{TM}) - \tilde{z}_0(1 + r_{TE})\right]\frac{k_x k_y}{k_x^2 + k_y^2}e^{-u_1 z} \tag{A.70}$$

$$\hat{E}_y(k_x, k_y, z) = \frac{m}{2}\left[-\frac{k_0^2}{\tilde{y}_1}\frac{u_1}{u_0}(1 + r_{TM})k_y^2 + \tilde{z}_0(1 + r_{TE})k_x^2\right]\frac{1}{k_x^2 + k_y^2}e^{-u_1 z} \tag{A.71}$$

$$\hat{E}_z(k_x, k_y, z) = \frac{m}{2}\left[-\frac{k_0^2}{\tilde{y}_1}\frac{ik_y}{u_0}(1 + r_{TM})\right]e^{-u_1 z} \tag{A.72}$$

$$\hat{H}_x(k_x, k_y, z) = \frac{m}{2}\left[\frac{k_0^2}{u_0}(1 + r_{TM})k_y^2 - u_1(1 + r_{TE})k_x^2\right]\frac{1}{k_x^2 + k_y^2}e^{-u_1 z} \tag{A.73}$$

$$\hat{H}_y(k_x, k_y, z) = \frac{m}{2}\left[-\frac{k_0^2}{u_0}(1 + r_{TM}) - u_1(1 + r_{TE})\right]\frac{k_x k_y}{k_x^2 + k_y^2}e^{-u_1 z} \tag{A.74}$$

$$\hat{H}_z(k_x, k_y, z) = \frac{m}{2}\left[-ik_x(1 + r_{TE})\right]e^{-u_1 z} \tag{A.75}$$

EM fields in the (x, y, z) space domain can be obtained using the 2-D inverse Fourier transform.

A.2.3 Finite-length line source

The finite-length line source, centered at the origin and extending from $-L/2$ to $L/2$ along the x-axis, can be represented by

$$\mathbf{J}_e^s = IL\, B(x)\, \delta(y)\, \delta(z)\, \mathbf{x} \tag{A.76}$$

where $B(x)$ is the box car function defined as

$$B(x) = \begin{cases} 1 & \text{if } |x| \leq \frac{L}{2} \\ 0 & \text{otherwise.} \end{cases} \tag{A.77}$$

Then the potential $\mathbf{A}$ equation in 2-D Fourier transform domain (k_x, k_y, z) is given by

$$\frac{d^2 \hat{A}_x}{dz^2} - u_0^2 \hat{A}_x = -IL\, \text{sinc}(\frac{k_x L}{2})\, \delta(z) \tag{A.78}$$

where the *sinc* function is defined as

$$\text{sinc}(x) = \frac{\sin(x)}{x} \tag{A.79}$$

By analogy with equations (A.49), (A.50), (A.53), and (A.54), the particular solution is

$$\hat{\mathbf{A}} = \hat{A}_x \mathbf{x} = \frac{IL}{2u_0}\text{sinc}(\frac{k_x L}{2})e^{-u_0 z}\mathbf{x} \tag{A.80}$$

and the separated TM_z and TE_z have the amplitudes

$$A_p(k_x, k_y) = -\frac{IL}{2}\text{sinc}(\frac{k_x L}{2})\frac{ik_x}{k_x^2 + k_y^2} \tag{A.81}$$

$$F_p(k_x, k_y) = -\frac{\tilde{z}_0 IL}{2u_0}\text{sinc}(\frac{k_x L}{2})\frac{ik_y}{k_x^2 + k_y^2} \tag{A.82}$$

Once $A_p(k_x, k_y)$ and $F_p(k_x, k_y)$ are derived, the rest of the derivation is straightforward. The solutions in a half-space are

$$\hat{E}_x(k_x, k_y, z) = \frac{IL}{2}\left[-\frac{u_1}{\tilde{y}_1}(1 + r_{TM})k_x^2 - \frac{\tilde{z}_0}{u_0}(1 + r_{TE})k_y^2\right]\frac{1}{k_x^2 + k_y^2}\text{sinc}(\frac{k_x L}{2})e^{-u_1 z} \tag{A.83}$$

$$\hat{E}_y(k_x, k_y, z) = \frac{IL}{2}\left[-\frac{u_1}{\tilde{y}_1}(1 + r_{TM}) + \frac{\tilde{z}_0}{u_0}(1 + r_{TE})\right]\frac{k_x k_y}{k_x^2 + k_y^2}\text{sinc}(\frac{k_x L}{2})e^{-u_1 z} \quad \text{(A.84)}$$

$$\hat{E}_z(k_x, k_y, z) = \frac{IL}{2}\left[-\frac{ik_x}{\tilde{y}_1}(1 + r_{TM})\right]\text{sinc}(\frac{k_x L}{2})e^{-u_1 z} \quad \text{(A.85)}$$

$$\hat{H}_x(k_x, k_y, z) = \frac{IL}{2}\left[(1 + r_{TM}) - \frac{u_1}{u_0}(1 + r_{TE})\right]\frac{k_x k_y}{k_x^2 + k_y^2}\text{sinc}(\frac{k_x L}{2})e^{-u_1 z} \quad \text{(A.86)}$$

$$\hat{H}_y(k_x, k_y, z) = \frac{IL}{2}\left[-(1 + r_{TM})k_x^2 - \frac{u_1}{u_0}(1 + r_{TE})k_y^2\right]\frac{1}{k_x^2 + k_y^2}\text{sinc}(\frac{k_x L}{2})e^{-u_1 z} \quad \text{(A.87)}$$

$$\hat{H}_z(k_x, k_y, z) = \frac{IL}{2}\left[-\frac{ik_y}{u_0}(1 + r_{TE})\right]\text{sinc}(\frac{k_x L}{2})e^{-u_1 z} \quad \text{(A.88)}$$

Vita

Xinyou Lu

Born: Zhejiang Province, P.R.China, July 15, 1965.

Education

09/1993-03/1999: Ph.D., Geophysics, University of Washington, Seattle.

08/1998-06/1999: MSEE, Electrical Engineering, University of Washington, Seattle.

09/1986-07/1989: M.Sc., Geophysics, China University of Geosciences, Beijing.

09/1982-07/1986: B.A., Applied Geophysics, China University of Geosciences, Wuhan.

Publications

Unsworth, M.J., Lu, X., and Booker, J.R., CSAMT exploration at Sellafield: characterization of a potential radioactive waste storage site, *Geophysics*, in review.

Lu, X., Unsworth, M., and Booker, J., 1999, Rapid relaxation inversion of CSAMT data, *Geophs. J. Int.*, in press.

Ogawa, Y., Jones, A.G., Unsworth, M.J., Booker, J.R., Lu, X., Craven, J., Roberts, B., Parmelee, J., and Farquharson, C., 1996, Deep electrical conductivity structure of the Appalachian Orogen in the southeastern U.S., *Geophysical Research Letters*, **23**, 1597-1600.

Wang, X., Tang, M. and Lu, X., 1992, Deep electric characteristics and nappe structure of Altun Mountain Slope, *Scientia Geologica Sinica*, **4**, 317-324 (in Chinese)

Wang, X., Tang, M. and Lu, X., 1992, Discovery of nappe structure in the Western Qaidam Basin – Magnetotelluric results applied to oil and gas prospecting, in *Lithospheric Tectonics and Resources*, 266-277, ed. Xu Guizhong, Ocean Publishing House, Beijing (in Chinese)

Lu, X. and Fu, L., 1991, IP nonlinear spectra of ores, *Geophysical & Geochemical Exploration*, **15**, 358-365 (in Chinese)

Abstracts & Presentations

Lu, X., Unsworth, M.J., and Booker, J.R., 1999, Inversion of CSEM Data From Finit-Length Line Source Exciting A 2D Earth, *The 22nd IUGG*, Birmingham.

Lu, X., Unsworth, M.J., and Booker, J.R., 1997, Two-dimensional inversion of tensor CSAMT data, *Expanded Abstracts, 67th Ann. Int. Mtg.*, 1, 362-365, Soc. Expl. Geophys., Tulsa.

Unsworth, M.J., Lu, X., and Watts, D., 1997, Site characterization for nuclear waste disposal using CSAMT exploration, *Expanded Abstracts, 67th Ann. Int. Mtg.*, 1, 358-361, Soc. Expl. Geophys., Tulsa.

Lu, X., Unsworth, M.J., and Booker, J.R., 1997, Rapid inversion of CSAMT data, *Proceedings of High-Resolution Geophysics Workshop*, Tucson.

Lu, X., Unsworth, M.J., and Booker, J.R., 1996, Rapid relaxation inversion of CSAMT data, *The 13th Workshop on Electromagnetic Induction in the Earth*, Onuma.